Insulator-to-metal Transition and Resistive Memory Switching in Cr-doped $SrTiO_3$: Charge-transfer Processes Involving the Cr Ions

Dissertation

zur

Erlangung der naturwissenschaftlichen Doktorwürde
(Dr. sc. nat.)

vorgelegt der

Mathematisch-naturwissenschaftlichen Fakultät

der

Universität Zürich

von

Fabio La Mattina
aus Italien

Promotionskomitee

Prof. Dr. Hugo Keller (Vorsitz)
Dr. Dr. h.c. mult. Johannes Georg Bednorz (Leitung der Dissertation)
Prof. Dr. Alexander Shengelaya
Prof. Dr. Dr. h.c. mult. Karl Alexander Müller

Zürich 2008

To Carlotta

Abstract

Nowadays, many companies aim to engineer non-volatile memory architectures with characteristics of speed and endurance comparable with those of volatile memory devices. Achieving such a technology would not only lower the power consumption, but it would allow for turning on and off a device bypassing the slow start-up and shut-down sequence for loading or storing data. In the present work, we investigated on the nature of the resistance change non-volatile memory, which has been found in perovskites oxides like (Ba,Sr)TiO_3, $SrZrO_3$, $SrTiO_3$. Exposed to an electrical field, the resistance of doped perovskites is reduced by several orders of magnitude and a conductor is obtained. We define this process as electro-conditioning (EC). In the conducting state, consecutive electrical current pulses of opposite polarity switch the resistance of the perovskites reversibly between a high-resistance and a low-resistance state. These two different states persist after removal of the applied electrical bias with a retention time of up to several years (non-volatile memory). We report on a study of single crystals of Cr-doped $SrTiO_3$ as a model system for this class of perovskite oxides. In particular we investigated the role of the Cr-dopant with respect to the physical processes involved in the insulator-to-metal transition and the resistive switching.

During a thermal reduction process of Cr-doped $SrTiO_3$ in Ar/H_2 atmosphere, a charge compensation associated with cre-

ation of oxygen vacancies (V_O) causes the valence of the Cr atoms to change from 4+ to 3+. We show that the insulating state of the crystal is preserved due to the interaction between the V_Os and the Cr^{3+} ions. Through the study of oxygen-reduced Cr-doped $SrTiO_3$, we found indications of a strong one-to-one correlation between the concentration of Cr^{3+} ions and V_Os. Thus, the Cr concentration and the thermal annealing in Ar/H_2 are methods to control the amount of V_Os in the bulk. Our findings open a pathway to study V_Os in the bulk on a microscopic scale for a deeper understanding of the conducting mechanisms of $SrTiO_x$.

Electron paramagnetic resonance (EPR) spectroscopy and electrical transport measurements during the EC process show anticorrelation between the intensity of the Cr^{3+} EPR signal and the electrical current flowing trough the sample. This is an evidence that the Cr-dopants act as a reservoir of electrons that produce the current that initiates the insulator-to-metal transition. Our electroluminescence (EL) measurements reveal that during resistive switching, light is emitted only in the transition from high to low conductivity. The EL spectrum observed is typical for Cr^{3+} in an octahedral ligand field, and indicates that the switching process involves trapping/detrapping of electrons at the Cr site. This result provides an important stimulus for the refinement of a microscopic theoretical model.

Zusammenfassung

Ziel modernster Forschung im Bereich der Datenspeicherungstechnologie ist es, bei nicht-flüchtigen ("non-volatile") Datenträgern Eigenschaften, wie etwa Prozessgeschwindigkeit und Langlebigkeit, zu erreichen, die mit herkömmlichen Komponenten vergleichbar sind. Diese neue Technologie birgt nicht nur das Potential, den Energieverbrauch zu optimieren, sondern ermöglicht auch, die Ein- und Ausschaltzeiten entsprechender Geräte zu verringern. In der vorliegenden Dissertation wurden Materialien, mit potenzieller Verwendungsmöglichkeit für nichtflüchtige Speicher, die auf materialspezifischen Widerstandsänderungen basieren, untersucht. Eine Abnahme des elektrischen Widerstandes um mehrere Grössenordnungen allein durch Anlegen elektrischer Felder wurde in dotierten Perovskit-Oxiden, wie z.B. (Ba,Sr)TiO_3, $SrZrO_3$ und $SrTiO_3$, gefunden. Dieser Prozess wird "electro-conditioning", kurz EC-Prozess genannt. Im leitenden Zustand elektrische Pulse entgegen gesezter Polarität verändern den elektrischen Widerstand reversibel zwischen einem hoch-resistiven und niedrig-resistiven Wert. Die erreichten metastabilen Widerstandswerte sind über mehrere Jahren stabil, daher die Bezeichnung "non-volatile". In der vorliegenden Arbeit wurden Cr-dotierte $SrTiO_3$ Einkristalle als Modellsystem verwendet. Insbesondere wurde die Bedeutung der Cr-Dotierung für die physikalischen Prozesse, welche für die Widerstandsänderung verantwortlich sind, untersucht.

Durch die thermische Behandlung der Proben in einer Ar/H2-Atmosphäre entstehen Sauerstoffleerstellen auf Grund von Ladungsausgleichsprozessen, wodurch die Valenz der Cr-Ionen von 4+ auf 3+ reduziert wird. Wir zeigen, dass der nichtleitende Zustand des Kristalls durch die Wechselwirkung zwischen Sauerstoffleerstellen und Cr^{3+}-Ionen erhalten bleibt. Die Untersuchungen an Cr-dotierten $SrTiO_3$-Kristallen, die in einer Argon/Wasserstoff (Mischung) Atmosphäre reduziert wurden, ergaben Hinweise auf eine direkte Korrelation zwischen der Zahl der Cr^{3+}-Ionen und der Zahl der Sauerstoffleerstellen (V_O). Über die Cr^{3+}-Dotierung und die thermische Behandlung der Probe in einer Ar/H2-Atmosphäre lässt sich die V_O-Konzentration in der Probe kontrollieren. Unsere Ergebnisse zeigen einen Weg auf, um die Rolle der Sauerstoffleerstellen auf mikroskopischer Ebene zu untersuchen und dadurch ein tieferes Verständnis des Leitungsmechanismus in $SrTiO_x$ zu erlangen.

Elektronenparamagnetische-Resonanz (EPR)-Spektroskopie und Transportmessungen
während des EC-Prozesses zeigen eine Antikorrelation zwischen der Intensität des Cr^{3+}-EPR-Signals und dem in der Probe fliessenden elektrischen Strom. Dieses Resultat ist ein Hinweis dafür, dass durch die Cr-Dotierung ein Elektronenreservoir geschaffen wird. Der Strom, der seinerseits den Leiter-Isolator-Umschaltprozess auslöst, wird aus ebendiesem Reservoir gespiesen. Unsere Elektrolumineszenz (EL)-Messungen zeigen, dass Lichtemission nur beim Übergang vom niedrig-resistiven zum hoch-resistiven Verhalten stattfindet. Das EL-Spektrum ist typisch für Cr^{3+}in einem oktaedrischen Ligandenfeld, und weist darauf hin, dass Cr eine wichtige Rolle für das Einfangen und Freisetzen von Elektronen während des Widerstandsänderungsprozesses spielt. Die Ergebnisse stimulieren eine Verfeinerung bestehender theoretischer Modelle.

List of Acronyms

ARPES	Angle Resolved Photoelectron Spectroscopy
CFT	Crystal Field Theory
DL	Delayed Luminescence
EC	Electro-Conditioning
EPR	Electron Paramagnetic Resonance
FET	Field Effect Transistor
CB	Conduction Band
FWHM	Full Width at Half Maximum
HR	High Resistance
IV	Current-Voltage
LR	Low Resistance
MIM	Metal-Insulator-Metal
MOM	Metal-Oxide-Metal
PC	Personal Computer
PL	Photo Luminescence
SO	Spin-Orbit
SPCM	Single Photon Counting Module
TM	Transition Metal elements
TTL	Transistor-Transistor Logic
XPS	X–ray Photoelectron Spectroscopy
XRPD	X–Ray Powder Diffraction
XANES	X–ray Absorption Near Edge Structure
XAS	X–ray Absorption Spectra
VB	Valence Band
V_O	Oxygen Vacancy

Contents

Chapter 1

Introduction

Volatile memory architectures, currently used as Random Access Memory (RAM) in common personal computers (PC) are high-speed but highly power-consuming while in use. This kind of memories lose their contents as soon as the computer or hardware devices are powered off, and need to transfer the data to low-speed, non-volatile memory storage prior to powering down. Non-volatile memories are devices that do not lose the data when the system or device is turned off and are commonly used for long-term persistent storage. Typically, a non-volatile memory either costs more or performs worse in term of speed than a volatile random access memory. Nowadays, many companies aim to engineer non-volatile memory architectures with characteristics of speed and endurance comparable with the volatile memory. Achieving such a technology would not only save energy, but it would allow to turn on and off a computer bypassing the slow start-up and shutdown sequence. Among the different concepts to realize new solid-state non-volatile memory devices based on resistively switching materials, novel oxides are being investigated with much effort, in order to engineer storage devices with high areal density and low power consumption. One approach is to use the classical phenomenon of ferroelectricity occurring in numerous perovskite oxides in a Field Effect Transistor (FET) structure [1, 2]. Here, switching the orientation of the ferroelectric polarization within the gate insulator allows to reversibly modulate the resistance in an adjacent channel, which is formed by a conducting oxide. Simpler memory cells can be realized with two terminal Metal-Oxide-Metal (MOM) structures in which an electrical stimulation in form of voltage or current pulses will establish two or more defined resistive states of the memory device. Since most of the oxides under investigation are insulators in the initial state, an electro-conditioning (EC) forming step [3–5] (e.g. a current limited nondestructive breakdown) has to be performed to drive the material into a conducting state, which is a prerequisite for the memory operation. Although the mechanism for establishing the "low" (LR) and "high" (HR) resistance states is well understood for the phase-change memories [6] (PCM) based on chalcogenide compounds, a clear picture describing the soft nondestructive electrical breakdown and the memory switching in binary and ternary oxides such as the perovskites has not yet emerged. Current-induced bistable resistance effects or voltage-controlled negative resistance phenomena in compounds such as Nb_2O_5 [7], TiO_2 [8], Ta_2O_5 [9] and NiO [10–13] , and selected perovskites recently investigated [14], exhibit strong similarities in the current-voltage (IV) characteristic from the macroscopic down to the nanometer scale [15, 16]. This suggests that a common scheme may be applicable. While most research is done on thin-film oxide layers, a few reports on memories are based on bulk single crystals. The Cr doped single crystals used for this work exhibit the same memory behavior as thin films and other oxides under investigation. Thus, $SrTiO_3$ is used as a model memory system to study the role of lattice defects controlled by dopants in the EC procedure and the memory operation. Upon exposure to an electrical field, the resistance of the doped perovskite is reduced by several orders of magnitude and a conductor is obtained, which is a prerequisite for the memory switching. Because of the high initial resistance, the EC procedure has to start at a high electric field of the order of 10^4 V/cm to initiate a current flow in the nA range. As continuous carrier injection leads to an increasing current with time, the voltage is decreased in steps to reduce the power level and prevent irreversible damage of the crystal (see Fig. 1.1). This

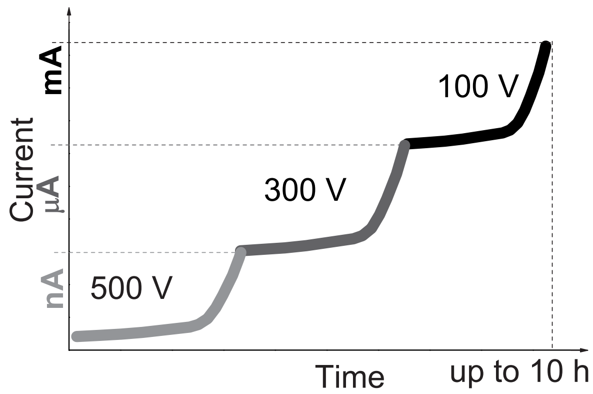

Figure 1.1: *Current-voltage behavior of a Cr-doped $SrTiO_3$ single crystal during the electro-conditioning procedure. The voltage is adjusted to minimize the power load to prevent irreversible damage. The increase of the conductivity shows a drastic change after long time exposure to high voltage.*

process can be accelerated by photo-excitation in the visible. The final conducting state, in which stable resistive switching is established, is typically reached within a few seconds for thin films up to a few hours in single crystals. Consecutive electrical current pulses of opposite polarity switch the resistance of the perovskite reversibly between a HR and a LR state. Figure 1.2 shows a typical hysteretic IV characteristic of a $SrTiO_3$ single crystal with a Cr content of 0.2 mol % as obtained after the EC process. By reaching a threshold voltage in the positive branch of the IV characteristic, the resistance switches from LR to HR. Viceversa in the negative branch the resistance switches from HR to LR. These two states have an ohmic behavior for low current voltage values and persist even if the power is turned off. It is still not clear how the EC process leads to such a memory behavior in the IV characteristics. Since the conducting state is not an intrinsic property of

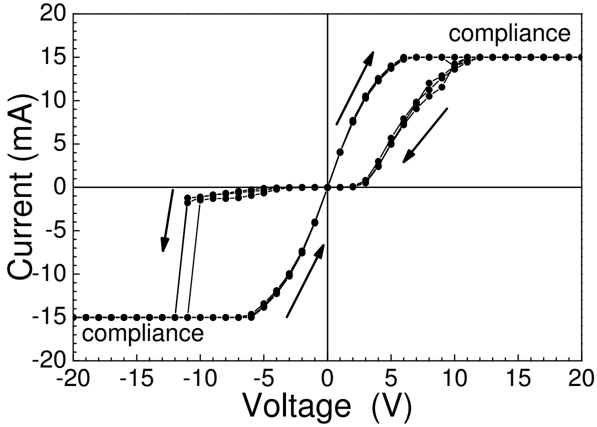

Figure 1.2: *Current-voltage characteristics of a single crystal Cr-doped $SrTiO_3$ ([Cr] = 0.2 mol%) memory cell. The compliance is set at 15 mA.*

Cr-doped $SrTiO_3$, understanding the EC process is crucial to build a model for the resistive switching. Figure 1.3 illustrates some of the models for the resistive switching of $SrTiO_3$ currently under discussion. A conductive filamentary path has been shown experimentally [4, 17] to result as a consequence of the EC procedure. Extended defects such as dislocations and changes in the V_O concentration are held responsible for the conducting state achieved by the EC, while local reduction/oxidation processes have been proposed as an explanation for the resistance switching mechanism (Fig.1.3.a) [4]. A phenomenological approach involving a non-percolating domain structure [18] tries to describe the conducting state in terms of tunneling of carriers between these regions (Fig. 1.3.b). In such a model the resistive switching is explained by charging or discharging these domain structures. High resolution imaging of X-ray absorption at the energy of the pre-edge of Cr showed that the EC process creates a conducting path (Fig.1.3.a) enriched of V_Os [4] in planar structures. On the other hand, further models propose modified interface properties. Changes

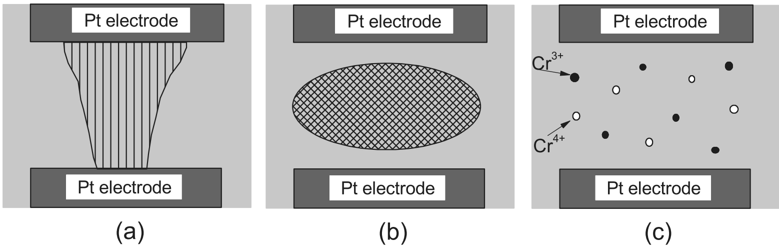

Figure 1.3: *(a) Percolating conducting region in Cr-doped $SrTiO_3$ as obtained after the electro-conditioning (EC) process. High resolution imaging by means of X-ray absorption near the K-edge (XANES) of Cr^{3+} on planar structure reveals an increasing of Cr^{3+}-V_O complexes in such a region [4]. (b) non percolating metallic region embedded in insulating $SrTiO_3$. Resistive switching could be explained by using tunneling of electrons through this region (producing charge and discharge) [17]. (c) Distribution of Cr^{3+}/Cr^{4+} ions in the bulk acting as traps and/or donor (triggered by the electric field) for the electron carrier.*

of the electronic state of the Cr dopant have been detected by X-ray absorption near edge structure (XANES) on crystals during electrical stressing, where it is possible to detect the transformation of Cr^{3+} to Cr^{4+} in a volume close to the metal electrode (anode). It is still not clear which role the Cr ion and its different valence states are playing in the resistive switching (Fig. 1.3.b) [3, 19]. By using electron paramagnetic resonance (EPR) it is possible to microscopically characterize different charge states of Cr in the bulk of $SrTiO_3$. In this work we performed EPR experiments on samples with different Cr doping concentrations in defined valence states controlled by thermal annealing processes. After an EPR characterization of the virgin materials, we investigated the effect of the EC process and the resistive switching, on the Cr valence state and the symmetry of its site. The EPR cavity and the sample holder were modified for in-situ measurements of IV, laser irradiation, and luminescence. The designed new set-up allows to study the changes in the electronic state of Cr during the EC process which leads to the insulator-to-metal transition and the different memory states.

Chapter 2

Sample preparation

In this chapter the methods used for the synthesis of $SrTiO_3$ powders and Cr-doped $SrTiO_3$ single crystals will be illustrated. In particular, it will be shown that in the sample preparation the concentration of transition metals (TM), which can display effects similar to Cr atoms, was accurately controlled.

2.1 Synthesis of $SrTiO_3$ powder

$SrTiO_3$ powder was obtained by heating a 1:1 mixture of $SrCO_3$ and TiO_2 powders. Heating the mixture at 1350 ^{o}C leads to the decomposition of $SrCO_3$ [20]:

$$\mathrm{SrCO_3} \quad \stackrel{T}{\rightarrow} \quad \mathrm{SrO} + \quad \mathrm{CO_2}(\uparrow) \tag{2.1}$$

Subsequently, the reaction of SrO with TiO_2 producess the $SrTiO_3$ powders via the solid state reaction:

$$\mathrm{SrO} + \quad \mathrm{TiO_2} \quad \stackrel{T}{\rightarrow} \quad \mathrm{SrTiO_3} \tag{2.2}$$

The reaction of these two powders during the thermal annealing is strongly affected by the grain dimensions and their mutual dispersion. X-ray powder diffraction (XRPD) spectroscopy was used to check the quality of the $SrTiO_3$ formed.

Figure 2.1 shows the XRPD pattern of the $SrTiO_3$ powder obtained after the first thermal annealing step. The comparison of this pattern with other standards [21], allows to distinguish $SrTiO_3$ from other products. The presence of residual TiO_2 (marked by the vertical blue lines) indicates that the reaction is not complete due to inhomogeneity in the distribution of the reactants.

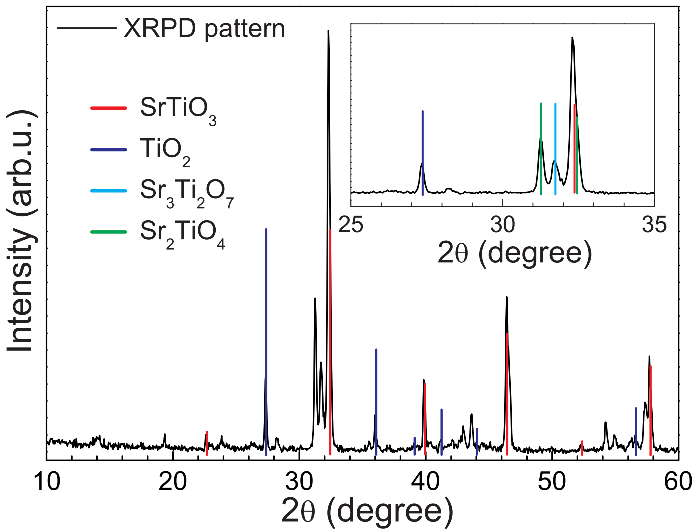

Figure 2.1: *X-ray powder diffraction (XRPD) pattern of a $SrTiO_3$ powder obtained after the first thermal treatment step (black line). The pattern is compared with those of selected standards [21].*

Therefore other SrO rich phases appear to compensate the non-reacted fraction of TiO_2. The inset in Fig. 2.1 shows an enlargement of the spectrum where the lines assigned to $Sr_3Ti_2O_7$ and $Sr_2Ti_2O_4$ are clearly visible. In order to eliminate these impurity phases, the powders were mixed again and the thermal annealing was repeated for a complete reaction of the TiO_2.

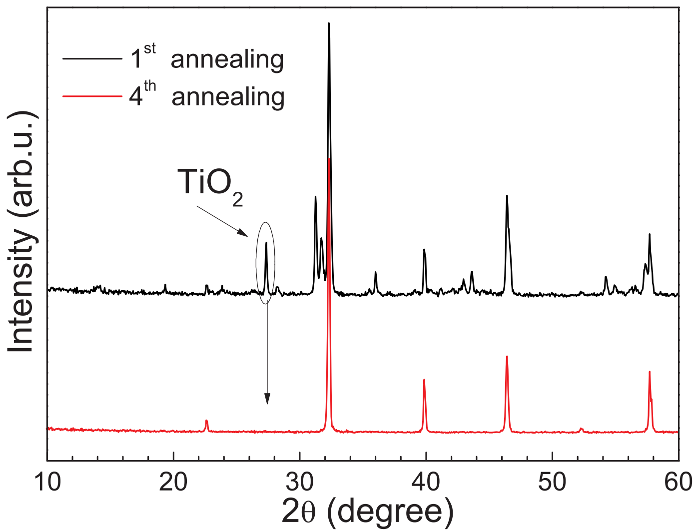

Figure 2.2: *Comparison between XRPD patterns of $SrTiO_3$ powders obtained from the same mixture: (black line) diffraction pattern obtained after one annealing step; (red line) diffraction pattern obtained after four annealing steps.*

Figure 2.2 shows the comparison between XRPD spectra after one and four annealing steps. Here, the peaks corresponding to TiO_2 disappear together with those of the SrO rich phases. For the investigations performed in this work, it was crucial to control the concentrations of TM's that could influence the electrical properties of $SrTiO_3$, similarly to the Cr atoms. Table 2.1 shows the impurity contained in the two reactants used for the preparation of $SrTiO_3$ powder. The powders used are TM-free on the level of 99.996% and 99.999% for TiO_2 and $SrCO_3$, respectively.

Impurities in TiO_2	mol%		Impurities in $SrCO_3$	mol%
Mg	$<$ **0.0002**		Mg	$<$**0.0001**
Fe_2O_3	$<$ **0.002**		Fe	**0.0002**
Cr	**0.0001**			
Cu	$<$ **0.0001**			
Mn	$<$ **0.0005**			
Ni	**0.0005**			
V	0.0006			
Al_2O_3	$<$ 0.003			
SiO_2	$<$ 0.002			
Sb_2O_3	$<$ 0.003		Ba	0.0004
SnO_2	$<$ 0.002		Ca	$<$0.0001
Pb	$<$ 0.00005		Na	0.0001

Table 2.1: *Impurity content in TiO_2 and $SrCO_3$. They result to be free of TM elements of about 99.996% and 99.999%, respectively.*

2.2 Cr-doping and sintering

Cr_2O_3 was admixed to $SrTiO_3$ to obtain Cr doping levels up to 0.2 mol%. $SrCrO_4$ was used to compensate the missing fraction of Sr in the stoichiometric mixture for Cr doping between 0.4 mol% and 2 mol%:

$$(1-x)\ \mathrm{SrTiO_3} \quad + \quad \frac{x}{2}\ \mathrm{Cr_2O_3} \qquad\qquad x \leq 0.002 \quad (2.3)$$

$$(1-x)\ \mathrm{SrTiO_3} \quad + \quad x\ \mathrm{SrCrO_4} \qquad\qquad 0.004 \leq x \leq 0.02 \quad (2.4)$$

The mixtures of $SrTiO_3$ and the dopant were then pressed at ~35 Kbar to obtain 100×5×5 mm^3 shaped rods which are then heated at 1100 ^{o}C for 6 h. At this temperature the sintering process leads to the formation of a mechanically stable ceramic to be used for the crystal growth.

2.3 Crystal growth

2.3.1 Zone melting

In the floating zone process [22] a molten zone is moved through a ceramic polycrystalline material. At the beginning of the process, the molten volume touches the top of a seed crystal and part of the liquid crystallizes keeping the seed orientation. Subsequently, the molten zone is forced to move through the ingot, resulting in a melting at the liquid-ceramic interface and a crystallization at the liquid-seed interface. If properly seeded, a single crystal will result.

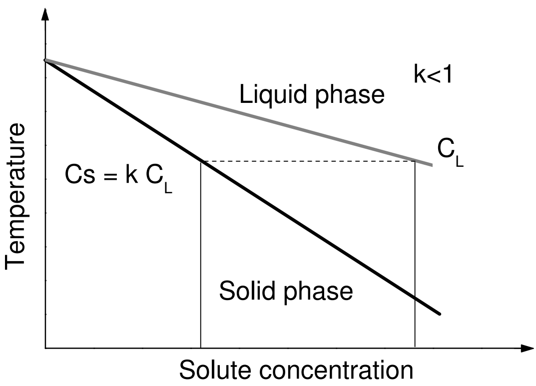

Figure 2.3: *Phase diagram of the solvent at different solute concentrations. The interceptions of the dashed horizontal line with the solid lines represent the equilibrium of a liquid phase with solute concentration C_L and a solid phase with C_S.*

The thermodynamics of these processes is essentially described by the equilibrium distribution coefficient k, defined as the ratio of the dopant concentration in the freezing solid C_{S} to that in the main body of the liquid C_{L}. Figure 2.3 shows a typical diagram of the solute concentration in the two different phases, where the solute lowers the melting temperature of the solvent. If freezing occurs slowly (ideally quasi-static), the solute concentration in the liquid is uniform, and the concentration in the freezing solid is k times the one in the liquid phase. In the real case, the advancing crystallization front of the liquid-solid interface rejects the solute more rapidly than it can diffuse into the main body of liquid. Hence, an enriched layer builds up ahead of the interface. The concentration in this layer rather than the one in the main body of liquid, determines the concentration that freezes out in the solid. In such a case, an effective distribution coefficient k_{eff} gives the ratio $C_{\mathrm{S}}/C_{\mathrm{L}}$. This coefficient is usually lower than 1 because impurity atoms "prefer" to stay in the melt [22].

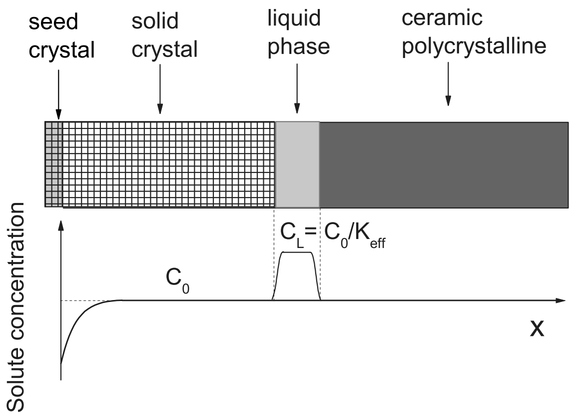

Figure 2.4: *Concentration of the solute after passage of one molten zone through a charge of uniform mean concentration C_0.*

In other words, the solubility of impurity atoms in the melt is larger than in the solid. If the liquid phase has a solute concentration C_L, the initial part of the crystal that forms contains a concentration C_S of solute, which is given by the intersection of the temperature horizontal line (dashed) with the solid phase line (see Fig. 2.3). Figure 2.4 shows the profile of the solute concentration in the single crystal phase, which forms after the passage of a melting zone in a ceramic ingot with a content C_0 of solute. During the progression of the molten zone trough the ingot, the solute concentration in the liquid (C_L) increases until a steady state with $C_L = \frac{C_0}{k_{eff}}$ is reached. This condition is satisfied when the melting rate of the ceramic feed and the crystallization rate are identical, and the molten volume is constant. The profile of solute along the principal axis (x) can be described as follows [22]:

$$C_S(x) = C_O \left(1 - (1 - k_{\text{eff}})e^{-\frac{k_{\text{eff}}x}{L}}\right) \tag{2.5}$$

Due to the distribution of C_S along the axis of the crystal (Eq. (2.5)), the first and the last parts of the crystal (∼5 mm of each side) are usually removed. The zone melting technique requires an apparatus that can locally control the temperature to achieve the melting point in a defined region. Any changes of parameters which modify the steady state while moving the molten zone will affect the quality and homogeneity of the final single crystal. At constant growth rate and for maintaining a constant diameter, the volume of the molten region, the melting rate of the ceramic feed, the crystallization rate, and the temperature are critical parameters, which must be controlled.

2.3.2 Floating zone apparatus

In floating zone crystal growth a liquid zone is moved through a suspended ingot in presence of an inert gas or controlled atmosphere. In this way, there is no incorporation of impurities that the melt picks up for instance by dissolving the crucible material. To heat a confined zone, an optical furnace based on two elliptical mirrors (Fig. 2.5) with a common focal point was used.

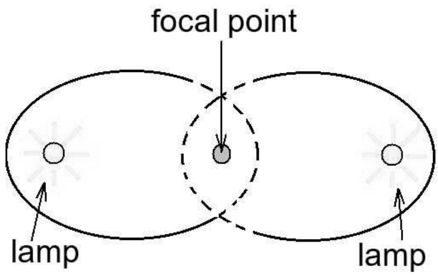

Figure 2.5: *Optical furnace. Two elliptic mirrors with a common focal point. Two lamps (commercial halogen, 1000 W) are attached at the other focal points.*

In the center of the furnace the temperature can be adjusted to reach the melting point ($\sim 2050\ ^oC$) of $SrTiO_3$. Figure 2.6a shows the furnace in operation. Two holes in the mirrors allow a projection (front and back) of the image of the molten zone and the crystal. In order to control the atmosphere during the crystal growth, a quartz tube of 10 cm diameter is placed in the center between the two elliptical mirrors as shown in Fig. 2.6b. Hence it is possible to have a controlled atmosphere. For the growth of $SrTiO_3$ a N_2/O_2 mixture (synthetic air) was used. The heated region consist of the superposition of the images of the two light sources, placed in the two individual focal points. The ceramic is fixed to a glass hook by platinum wires, while the seed crystal is inserted into a platinum tube.

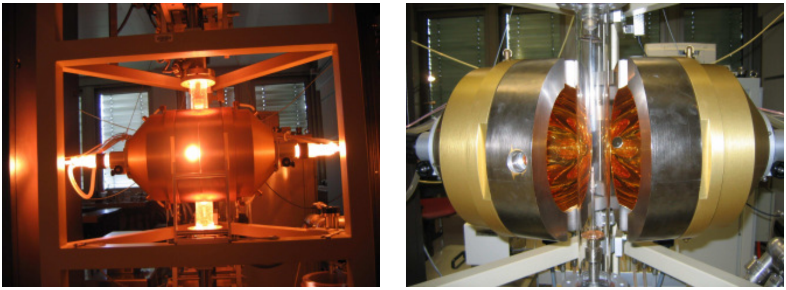

(a) (b)

Figure 2.6: *Floating zone apparatus: (a) during the crystal growth, two holes in the optical mirrors allow to project the image of the molten zone on screens on the front and back; (b) a quartz tube is inserted in the central axis to flux syntectic air.*

Figure 2.7a shows the ceramic approaching the seed crystal. During this procedure the temperature and the position of the ceramic are carefully adjusted in order to melt the starting volume. The resulting liquid zone is then forced to touch the seed by moving the ceramic, and during the rest of the growth the seed and the ceramic are pulled down at constant speed. In order to keep the volume of the molten zone constant, the melting rate of the ceramic and the crystallization rate must be equal. This condition guarantees to reach the steady state of $C_S(x)$ described in the previous paragraph. Since the densities of the single crystal and the ceramic are different, the speeds to pull down these two parts have to be adjusted, typically between 15 and 20 mm/h, by controlling the evolution of the volume of the molten zone.

Moreover the seed is rotated to continuously mix the liquid zone. This rotation helps to have a more uniform distribution of the solute in the liquid phase. The growing-time of the crystals prepared in this work was about 4 h.

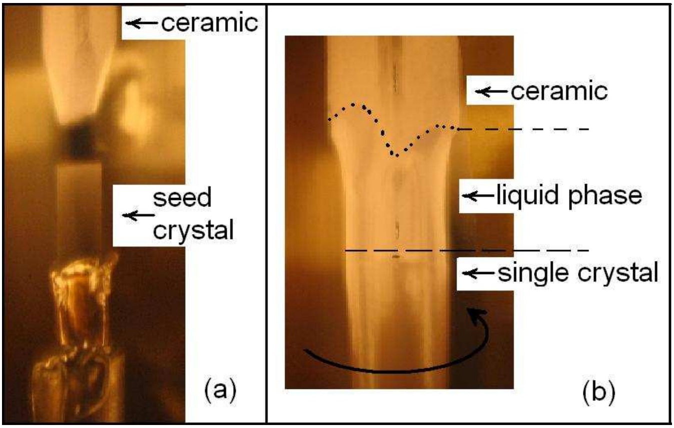

Figure 2.7: *Images of the crystal during the crystal growth. Projections of the light from the two holes in the optical mirrors (Fig. 2.6a): (a) the ceramic is approaching the seed crystal and the melting point of the $SrTiO_3$ is not reached; (b) the molten part of the ceramic touched the seed and freeze by crystallizing with the same orientation as the seed.*

Figure 2.8 shows two crystals which have been grown with this method. They have a cylindrical shape with ~5 mm diameter and a length of ~5 cm. The seed crystals are still attached to the cylinders of the Cr-doped $SrTiO_3$ single crystals. The color of these as-grown crystals is dominated by the presence of the Cr dopant which acts as color center and also depend on the Cr valence states.

Figure 2.8: *$SrTiO_3$ single crystals: (dark gray) [Cr] = 0.2 mol%; (orange) [Cr] = 0.01 mol% .*

2.4 The sample preparation

X-Ray Laue diffraction was performed on the as-grown crystals to find the {100} faces. Figure 2.9 shows a typical diffraction pattern of a (100) face. The orientation was performed by using a goniometer with a division scale of 0.1 degree. Due to the dimension of the spot in the diffraction pattern the precision in finding the final direction is affected by an error of <0.5 degree.

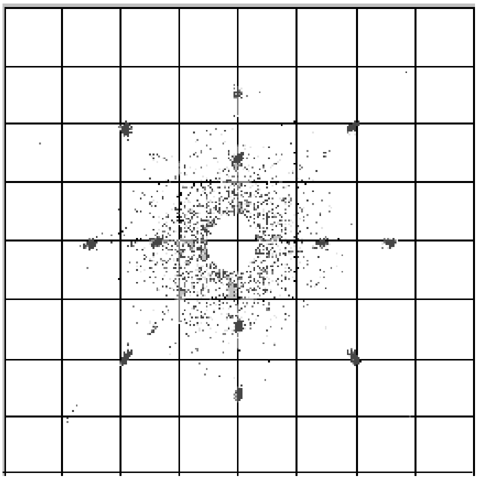

Figure 2.9: *X-ray Laue diffraction pattern of a (100) face of $SrTiO_3$.*

The oriented crystals were cut in disks of 1 mm thickness and 5 mm diameter. For the investigation presented in this thesis, a series of crystals were grown with Cr doping from 0.001 mol% up to 2 mol%. We performed two types of thermal annealing under flowing of Ar/H_2 (5%), or O_2 for each doping. In the case of Ar/H_2 the Cr dopants are forced to be in the 3+ valence state because of a charge compensation with V_Os introduced by the annealing, whereas in the case of O_2, the Cr ions are in the 4+ valence state. We define as virgin samples the pristine samples after the reduced anneling. Figures 2.10a and b show the temperature ramps used during the thermal treatments.

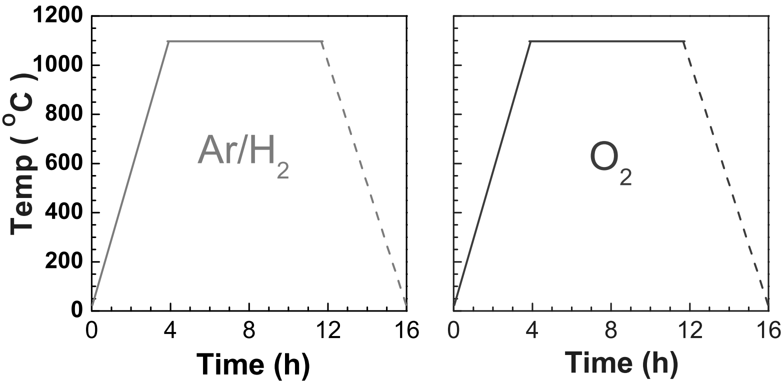

Figure 2.10: *Scheme of the two annealing procedures: (a) thermal annealing in* Ar/H_2*; b thermal annealing in* O_2*. The samples used for the electro-conditioning and the resistive switching were annealed in* Ar/H_2*.*

Temperature ramps of $\sim 5^oC/min$ were chosen to avoid thermal shock which could damage the crystal. In the rest of this manuscript we have to distinguish three type of samples: the as-grown samples (pristine), the reduced samples (virgin), and the conducting samples obtained from the virgin samples after the EC process.

Chapter 3

Electron Paramagnetic Resonance

The technique of electron paramagnetic resonance (EPR) allows to study the energy levels of an electronic magnetic dipole of an atom in a magnetic field. The electronic magnetic dipole originates both from the magnetic moment associated with the spin momentum S and the orbital angular momentum L of the electrons of the atom. A short introduction to the basic principles of EPR is given in this chapter. In particular, the effect of an octahedral crystal field on the Cr^{3+} *EPR signal is described. The reader is referred to textbooks for a more detailed description [23–26].*

3.1 The Zeeman energy splitting

The potential energy of a magnetic dipole moment $\overrightarrow{\mu}$ in presence of a magnetic field $\overrightarrow{B}$ along the z axis is given by:

$$E = -\overrightarrow{\mu} \cdot \overrightarrow{B} \tag{3.1}$$

with

$$\overrightarrow{\mu} = g\ \beta\ \overrightarrow{J} \tag{3.2}$$

where β is the Borhr magneton, g is the Landé factor, and $\overrightarrow{J}$ is the total angular momentum.

Because of the $2J + 1$ projections (m) of the angular momentum along the $\overrightarrow{B}$ field, Eqs. 3.1 and 3.2 lead to the Zeeman energy levels [24–26] given by:

$$E_m = -g \ \beta \ m \ B \tag{3.3}$$

By means of EPR technique we study the transition between the the Zeeman energy states of Eq. (3.3).

3.1.1 Crystal field theory

In 1929 Hans Bethe developed the crystal field theory (CFT) [23] by applying group theory to quantum mechanics. From this perspective, the energy of a TM ion in a crystal matrix is calculated by neglecting the covalent bonding with the neighbor atoms. The interaction of the ion with the crystal field is treated with a simple approach, just as the attraction between the positively charged metal cation and the negative charge of the electrons of the ligands. According to this theory, the Hamiltonian of a TM ion in a crystals is given by:

$$\mathcal{H} = \mathcal{H}_{\text{ion}} + \mathcal{H}_{\text{SO}} + \mathcal{H}_{\text{cryst}} \tag{3.4}$$

where $\mathcal{H}_{\text{ion}}$ is the sum of the Coulomb interaction and the kinetic energy of the isolated ion, $\mathcal{H}_{\text{SO}}$ represents the spin-orbit (SO) interaction of the ion, and $\mathcal{H}_{\text{cryst}}$ is the electrostatic interaction term of the ion with the crystal field.

3.2 The case of Cr^{3+}

3.2.1 Cr^{3+} in an octahedral crystal field

Let's consider, as an example, the effect of an the octahedral crystal field with cubic symmetry on the ground state of Cr^{3+}. According to Hund's rules, the Cr^{3+} 3d^3 electrons on the last occupied shell lead to the $^4F_{\frac{3}{2}}$ multiplet ($^{2S+1}L_J$) describing the ground state (see Fig. 3.1).

m_L

	-2	-1	0	+1	+2
(3d^3)			$\uparrow$	$\uparrow$	$\uparrow$

$$S = \frac{3}{2}\ , \quad L = 3\ , \quad J = |\, L - S \,| = \frac{3}{2} \qquad \Longrightarrow \qquad {}^4F_{\frac{3}{2}}$$

Figure 3.1: *Construction of the $^4F_{\frac{3}{2}}$ multiplet corresponding to the ground state of 3d^3 electronic configuration. In the table each position (m_L) corresponds to a projection of the orbital angular momentum L. The arrows indicate the spin moment S (up or down) of the electrons that are distributed according to Hund's rules, and J is the total angular momentum.*

Within the CFT theory, an energy splitting of $^4F_{\frac{3}{2}}$ multiplet states (crystal field splitting) occurs. Such a splitting arises because of the orientation of the d orbitals. In particular, the energy increases when the orbital is located in a region of high electron density, and decreases in the other case. Figure 3.2 shows the effect of an octahedral crystal field with cubic symmetry on the energy levels of the $^4F_{\frac{3}{2}}$ multiplet. For example, such a crystal field can be due to an octahedral arrangement of oxygen atoms like in $SrTiO_3$. Here, the Cr^{3+} is located at the center of the octahedron. Since the lobes of the xy, the xz, and the yz orbitals (t_{2g}) point midway to the oxygen anion positions (Fig. 3.2), they give rise to the same electrostatic interaction. Such an interaction energy is weaker than

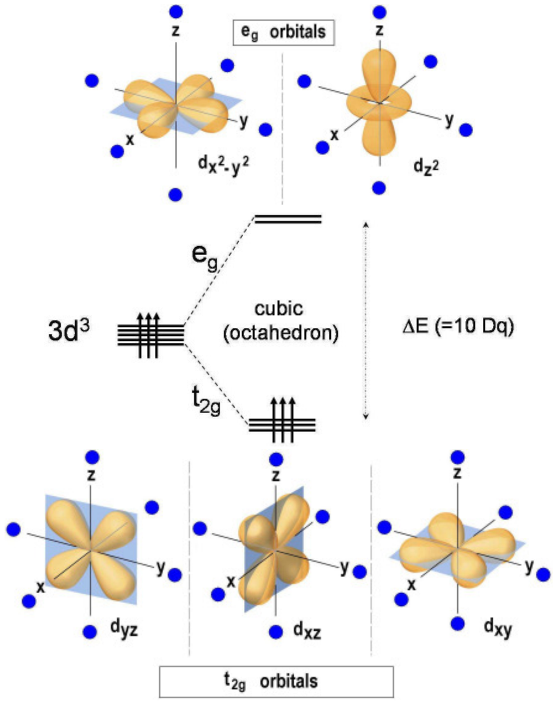

Figure 3.2: *Splitting of the energy levels of the* Cr^{3+} $^4F_{\frac{3}{2}}$ *multiplet in an octahedral field with cubic simmetry.*

in the case of the x^2-y^2 and the 3 z^2-r^2 orbitals (e_g), for which the lobes point directly to the oxygen locations. Therefore, the d orbital degeneracy is removed, giving rise to a ground state with an orbital angular momentum $L = 0$ (quenching of the orbital angular momentum), and a spin moment S $= \frac{3}{2}$.

3.2.2 The spin-orbit correction: effective spin hamiltonian

The spin-orbit (SO) term of Eq. (3.4) can be written as:

$$\mathcal{H}_{\mathrm{SO}} = \lambda \overrightarrow{L} \cdot \overrightarrow{S} \tag{3.5}$$

where λ is the strength of the SO interaction, $\overrightarrow{L}$ is the orbital angular momentum, and $\overrightarrow{S}$ is the spin momentum. The introduction of the SO interaction in the Hamiltonian (Eq. (3.4)) produces and additional energy correction term of the ground state. As a general method, we can construct an effective spin Hamiltonian which simplifies the description of such an interaction [24, 26].

$$\mathcal{H}_{\mathrm{eff}} = \beta \overrightarrow{B} \cdot \widetilde{g} \cdot \overrightarrow{S} + \overrightarrow{S} \cdot D \cdot \overrightarrow{S} \tag{3.6}$$

In this equation the effect of the SO term is taken into account by an effective tensor $\widetilde{g}$ instead of the g factor, and the tensor D:

$$\widetilde{g} = g_{\mathrm{e}} I + 2 \lambda \Lambda \tag{3.7}$$

$$D = \lambda^2 \Lambda \tag{3.8}$$

where g_e is the g factor of the free electron $\sim$2.00232, I is the unit tensor, λ is the spin-orbit interaction energy of the ion, and the tensor Λ is a function of the orbital angular momentum of certain excited state, which are coupled to the ground state through the SO interaction. When the angular momentum of a system is purely due to a spin moment, the tensor g should be isotropic with the value g_e. Any anisotropy and deviation from this value result from the tensor Λ which contains the orbital angular momentum from the coupled excited states. According to the CFT, for Cr^{3+} in an octahedral crystal field of cubic symmetry $\widetilde{g}$ is isotropic but its value deviates from g_e as [25]:

$$g = g_e - 8 \frac{\lambda}{\Delta E} \tag{3.9}$$

Here $\Delta E = 10\ Dq$ is the amplitude of the crystal field energy splitting described in Fig. 3.2. However, in order to obtain the right g factor it is necessary to include the covalent bonding with the oxygen atoms. This can be done by studying the overlap of the electronic wave function of the Cr^{3+} and the oxygen atoms [27, 28].

3.2.3 The nuclear spin interaction

In case of ion with a nuclear spin, an additional term must be considered in the spin Hamiltonian:

$$\mathcal{H}_{\text{nucl}} = A\ \overrightarrow{I} \cdot \overrightarrow{S} \tag{3.10}$$

Here A is the interaction energy between the nuclear spin I and the electron spin S, analogue to λ for the SO term. This terms leads to an additional energy splitting which can be described by:

$$\Delta E(m_S\ m_I) = A\ m_S\ m_I \tag{3.11}$$

where m_S and m_I are the electron spin and nuclear spin projection moments, respectively.

Cr has four isotopes with different nuclear spin: ^{50}Cr, ^{52}Cr, ^{54}Cr with I=0, and ^{53}Cr of 9.5% abundance with $I=\frac{3}{2}$. The Cr^{3+} EPR signal originates from the superposition of their contributions (see Chap.5).

Chapter 4

The EPR spectrometer

In this chapter a short description of the EPR spectrometer used in this work will be given. Moreover, a set-up, which combines the EPR detection with in-situ current-voltage (IV), laser irradiation, and luminescence measurements will be presented.

4.1 The spectrometer

The spectrometer used in this work is a Bruker EMX^{TM} system, which operates at microwave frequencies between 9 and 10 GHz (X band).

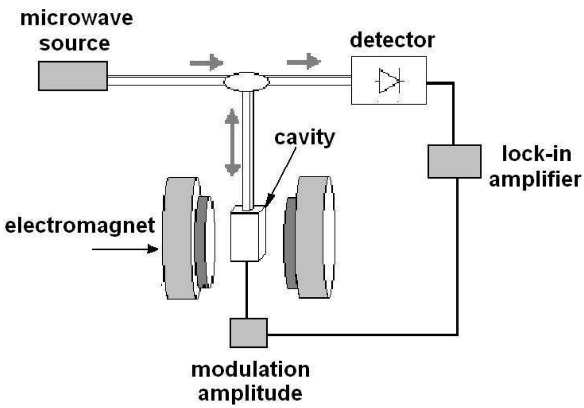

Figure 4.1: *Block diagram of the EPR spectrometer.*

The block diagram presented in Fig. 4.1 shows the main elements of the EPR apparatus. The apparatus works at a fixed frequency of the electromagnetic radiation, by varying the applied magnetic field H_0 through the resonance condition. The operating frequency ν_0 is tuned to the TE_{102} normal mode of the rectangular resonant cavity [29]. When H_0 sweeps through the resonance condition, the spectrometer detects the absorbtion by measuring the microwave power reflected from the cavity, which depends mainly on the energy absorbed from the cavity and the paramagnetic sample inside. This measurement is improved by using a phase sensitive detection (lock-in amplifier).

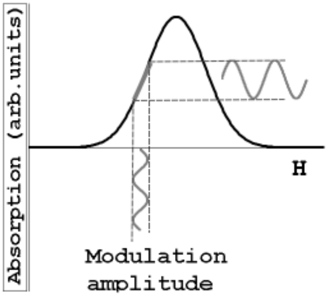

Figure 4.2: *Effect of the modulation amplitude on the EPR absorption. The modulation of the absorption power is detected by means of lock-in technique.*

While H_0 sweeps, a low frequency (100 kHz) oscillating field $H(t)$ is superimposed (modulation amplitude) as shown in Fig. 4.2. As a consequence, the paramagnetic resonance response is modulated at this frequency. The lock-in amplifier extracts the modulated component in phase with the modulation amplitude, from the reflected power. Therefore the EPR signal detected is proportional to the first derivative of the paramagnetic resonance absorbtion.

4.2 The resonant cavity

The resonant cavity used works as a band-pass filter with a quality factor Q of $\sim$ 6000, defined by:

$$Q = \frac{\nu_0}{\Delta\nu} \tag{4.1}$$

where $\Delta\nu$ is the full width at half maximum (FWHM) of the spectral range tuned with the cavity. Q represents the capability to fix a selected frequency, and the EPR signal intensity is proportional to Q [29]. Inside the cavity, the standing electromagnetic wave (at $\nu = 9.4$ GHz, i.e. $\lambda = 3$ cm) has its electric and magnetic field components exactly out of phase, i.e. where the magnetic field is maximal, the electric field is minimal and vice versa. The spatial distribution of the amplitudes of the magnetic and electric fields for the TE_{102} mode that we used is shown in Fig. 4.3.

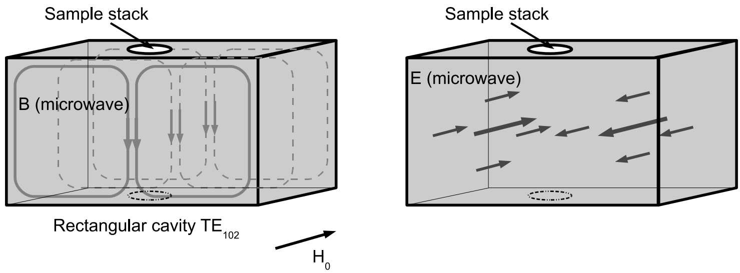

Figure 4.3: *Representation of the TE_{102} normal mode of the resonant cavity: (red lines) microwave magnetic field distribution; (blue arrows) microwave electric field distribution.*

The sample is inserted in the geometrical center of the cavity, where the microwave magnetic field is maximal. The cavity is oriented in such a way that the microwave magnetic field at the sample position is orthogonal to the applied field H_0 generated by the electromagnetic coils (Fig. 4.1). H_0 induces the Zeeman splitting, and the microwave field of the cavity is responsible for the transition between these states. The interaction with the microwave radiation involves the angular momentum operator J_x [24, 26]. This leads to the selection rule condition $\Delta m = \pm\ 1$ [24,25], where m represent the projections of J_z (see par. 3.1). Due to the intensity distribution of the standing wave of the microwave field inside the cavity, the position of the sample affects the EPR signal intensity. Moreover, prior to the measurement session, the tuning of the microwave source with the resonant cavity modifies the power trasmitted into the cavity at each session. These two circumstances lead to a reproducibility of the EPR measurements with an error of 10%. In order to study the effect of the EC process and the resistive switching on the Cr^{3+} signal, a set-up to allow EPR and in-situ IV experiments was designed. The sample, together with a reference marker, are fixed inside the cavity, and the EC process is performed without further touching the sample. This simple procedure decreases the error of the EPR intensity measurement to $\leq 1\%$.

4.3 Pt electrodes

In order to apply a voltage on the sample, it is necessary to deposit two metallic electrodes on the opposite surface of the crystal. The presence of electrodes on the surface of the crystal, and electrical wires inside the EPR cavity turned out to be a problem, since any metal inside the cavity can disturb the normal mode of the cavity, or even destroy it.

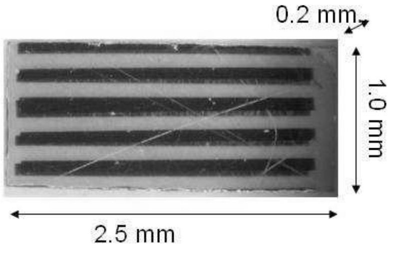

Figure 4.4: *Pt electrodes on the (100) large faces of a polished crystals of Cr-doped $SrTiO_3$. The electrodes were deposited by E-beam evaporation (50 to 100 nm thickness).*

In order to overcome this problem, capacitor-like structures of dimensions $2.5 \times 1 \times 0.2$ mm^3 were prepared by depositing special designed Pt electrodes (50 to 100 nm thickness) on the (100) large faces of the polished crystals via E-beam evaporation (Fig. 4.4). The electrodes consist of 0.1×2 mm^2 stripes with a gap of 0.15 mm, interconnected by drops of silver paint to form a meandering structure. These structures are an approximation of a continuous metallic layer, which were found to be transparent to the microwave radiation without disturbing the normal mode of the cavity. The wires were twisted and inserted along the axis of the sample holder which is placed in the center of the cavity (see Fig. 4.5).

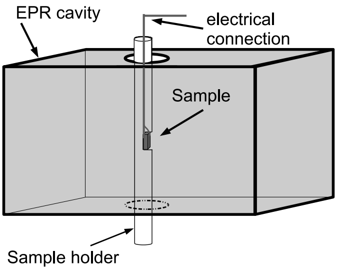

Figure 4.5: *Resonant cavity with the sample inserted (red). The blue line represent the electrical wires mounted along the axis of the sample holder. This position guarantees a minimal interference of the wires with the electric component of the microwave field.*

The Q factor of the cavity that we used is $\simeq$6000 and reduces to $\simeq$5000 after loading the sample. In the case of a sample with Pt electrodes (Fig. 4.4) connected to electrical wires (Fig. 4.5) Q is $\sim$ 4000. This means that for our experiments the sensitivity decreases by a factor $\frac{1}{5}$.

4.4 The in-situ experiments

A radiative charge transfer process involving the Cr^{3+} was studied in this work by combining luminescence with EPR measurements during the EC process. For this reason, the resonant cavity described in the previous paragraphs was modified. In particular, a special hole (Figs. 4.6 and 4.7) with a diameter

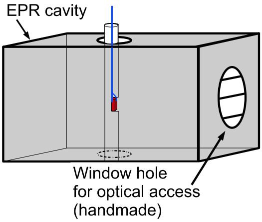

Figure 4.6: *Resonant cavity with a modified wall for the optical access.*

of 1.5 cm was made in the wall of the resonant cavity. This hole is aligned with two optical lenses. It was designed to give sufficient access to illuminate the sample with a laser, and collect the light emitted by the sample. The hole does not change

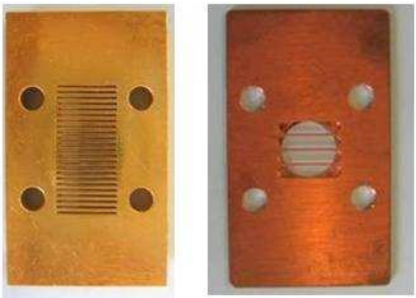

(a) (b)

Figure 4.7: *Walls of resonant cavity used for optical access: (a) commercial wall; (b) handmade wall with a circular hole of 1.5 cm diameter.*

the Q factor of the EPR cavity. The sample position coincides with the center of the cavity and the focal point of the first lense. The experimental set-up used for these experiments is

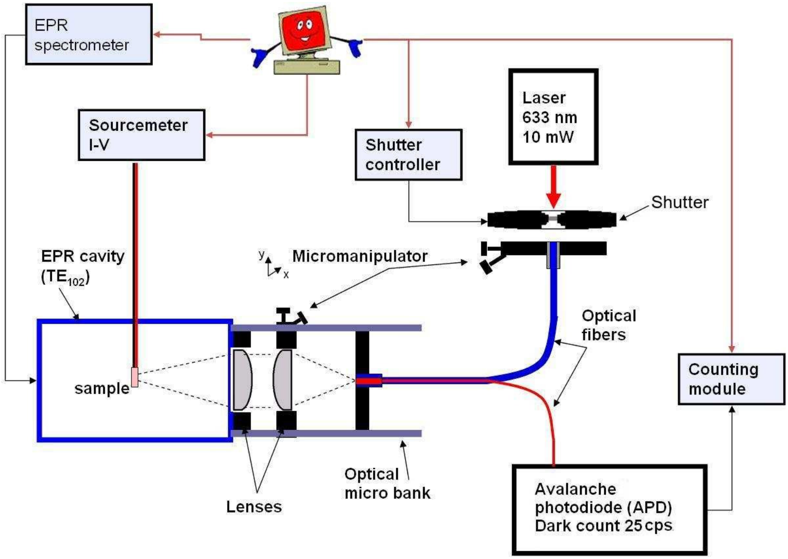

Figure 4.8: *Schematic diagram of the apparatus that combines EPR, IV, laser irradiation, and luminescence measuraments.*

schematically shown in Fig. 4.8. A special double fiber is used both for the laser irradiation and the collection of the light emitted by the sample. In particular, to measure the luminescence the core of the fiber is coupled to a single photo counting module (SPCM) of Laser Components GmbH. The SPCM produces a TTL pulse for each incoming photon and has a dark count of 25 photons/sec. This counting module is connected to an Canberra Lin-Log Ratemeter 14481-La, which was used to measure the incoming photon-rate. The photoluminescence experiments were performed using an optical multichannel analyzer covering a spectral range from 300 to 1000 nm and a photon-counting Si avalanche photodiode for the wavelength-integrated signal in the range from 400 to 1060 nm. The full system is synchronized via a PC.

Chapter 5

Oxygen vacancy proximity effect to the Cr^{3+} site

Changes in the oxygen vacancy (V_O) content, were shown to be responsible for the electron conduction in pure $SrTiO_3$ [30,31]. A new promising concept for electronic engineering has focussed on the possibility of confining V_Os in regions of nanometer dimensions [16,32,33]. Moreover, it has been proposed that the spatial distribution [34,35] of V_Os is responsible fot both the enhancement and/or the decrease of carrier density. In this chapter it will be shown how V_Os are spatially distributed with respect to Cr atoms in reduced Cr-doped $SrTiO_3$ single crystals, and how such a correlation affects the transport properties of the material.

5.1 Symmetry of the Cr^{3+} site in oxygen-reduced $SrTiO_3$

As shown in Fig. 5.1, Cr dopants in $SrTiO_3$ are substituting Ti atoms. At this octahedral site Cr has a 4+ valence state as Ti. In such an electronic configuration Cr^{4+} has spin $S = 1$, and it is EPR silent at the X-band due to the strong crystal field splitting [36,37] which does not permit to see the allowed EPR transitions. A direct detection of Cr^{4+} requires measurements at higher frequencies (Q-band) [36, 37]. Because Cr^{4+} acts as an electron trap, in the presence of electron donors (impurities or V_Os) it changes to the trivalent state. Figure 5.2

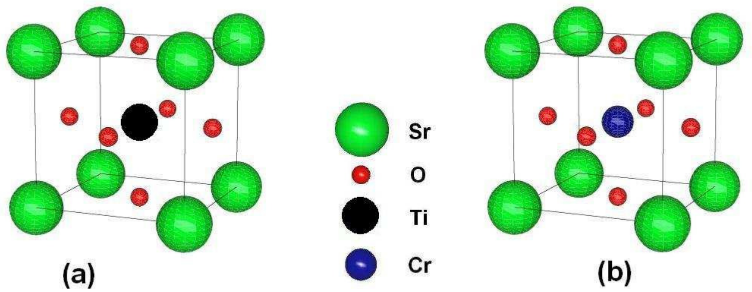

Figure 5.1: *(a) Crystal structure of* $SrTiO_3$*. (b) Structure of the Cr site in Cr-doped* $SrTiO_3$*.*

shows a comparison between the EPR signals of Cr^{3+} in a Cr/Nb-codoped sample (blue line) and Cr-doped oxygen reduced sample (black line). These two cases are an example of two different kind of electron doping. Through an EPR analysis of these crystals we determine how the charge-compensation between the electron donors and the Cr ions can affect the symmetry of the Cr sites. The EPR signal of Cr^{3+} consists of one central line ($g \approx 1.978$) resulting from the 3+ ionic state of the ^{50}Cr,^{52}Cr,^{54}Cr isotopes and one hyperfine quartet resulting from the nuclear spin coupling ($I_n = \frac{3}{2}$) of the isotope

^{53}Cr (natural abundance 9.5%) [38]. The hyperfine constant of the nuclear spin coupling $A \approx 16 \cdot 10^{-4}$ cm^{-1} determines the splitting of this quartet, as indicated in the spectra. The comparison between the spectra in Fig. 5.2 reveals a different lineshape for the two cases. In the Cr/Nb co-doped sample

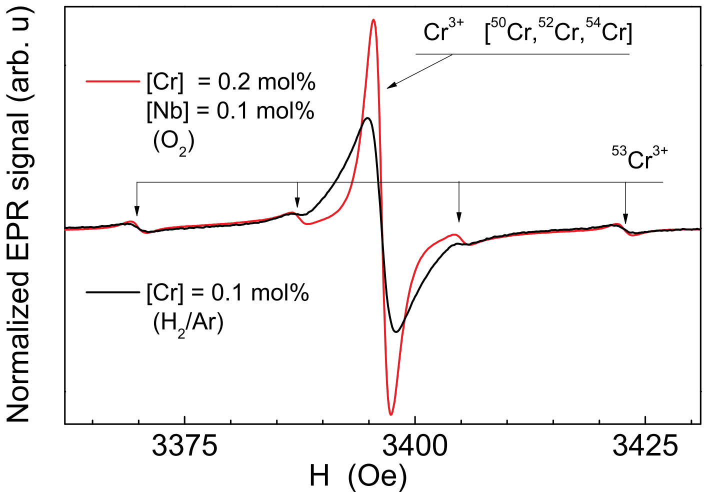

Figure 5.2: *Comparison of Cr^{3+} EPR signals in $SrTiO_3$. The spectra exhibit different site symmetries: (red line) isotropic signal detected in the as grown Cr/Nb-doped sample ([Cr]=0.2 mol%, [Nb]=0.1 mol %); (black line) signal detected in the oxygen reduced Cr-doped sample ([Cr]=0.1 mol %).*

([Cr] =0.2 mol %, [Nb] =0.1 mol %) the nominal content of the electron donor Nb determines the Cr^{3+}/Cr^{4+} fraction. On the other hand, the reduced sample was chosen with a Cr content of 0.1 mol % in order to have the same Cr^{3+} spin centers as the Cr/Nb-codoped sample. The reduced sample has a broad EPR component overlapping the central line.

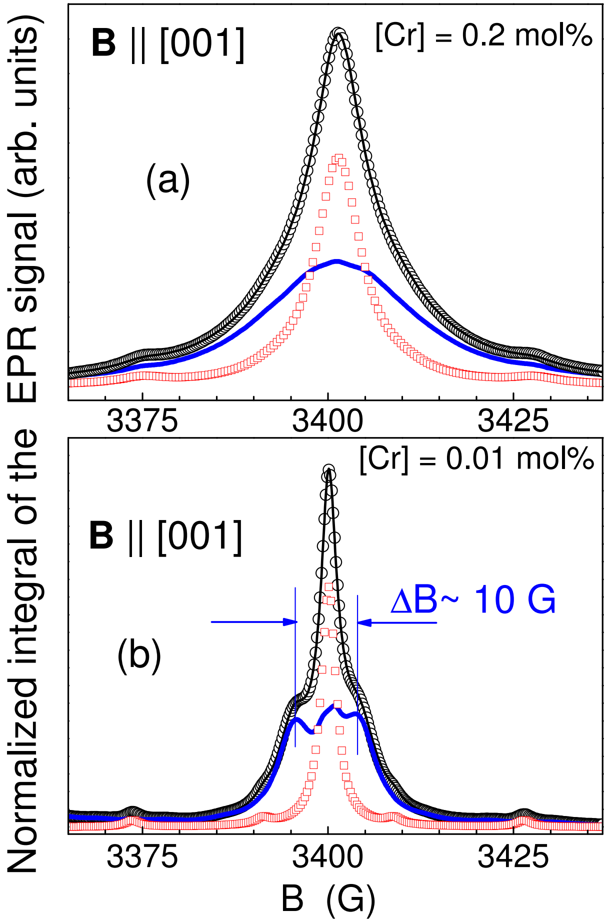

Figure 5.3: *Integral of the EPR signal of reduced Cr-doped $SrTiO_3$: (a) [Cr]=0.2 mol%; (b) [Cr]=0.01 mol%. The spectra were fitted with a Lorentzian line, including the four hyperfine lines ($^{53}Cr^{3+}$) and three broad lines for the anisotropic component. The result of the fitting is reported: (black open circles) measured spectra; (red line) the isotropic narrow lines; (blue line) the anisotropic component obtained as difference between the measured data and the fitted red component; (black line) fitted spectra.*

This broadening cannot be explained in terms of magnetic dipolar interaction, because in such a sample the Cr content (therefore the total number of spin centers) is lower than in the Cr/Nb sample. The angular dependence of these EPR spectra was studied with respect to the orientation of the crystal axes and the applied magnetic field. This investigation reveals that the Cr^{3+} signal is isotropic in the Cr/Nb case, whereas the broad line in the reduced sample shows an angular dependence. Furthermore, the same angular dependence was observed for the central line and the hyperfine lines of the reduced sample. Because these satellite lines are a signature of the $^{53}Cr^{3+}$ ion (nuclear hyperfine spin coupling), we concluded that the anisotropic component overlapping the EPR central line has to be assigned to a Cr^{3+} spin center in a non-cubic site.

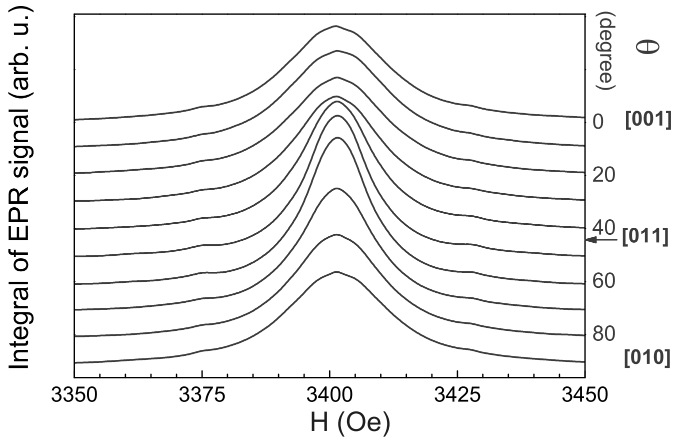

Figure 5.4: *Angular dependence of the anisotropic component of the EPR signal for the Cr-doped (0.2 mol %) reduced sample. Sample rotation is around a [100] crystal axis.*

A deconvolution of the Cr^{3+} EPR spectra was performed to characterize the symmetry of this site in the reduced crystals. As shown in Fig. 5.3, a narrow (red line) and a broad (blue line) component can be clearly separated, for all the Cr-doping levels. Here the deconvolution was performed for two different representative Cr concentrations of 0.2 and 0.01 mol% (Fig. 5.3). It was observed that the narrow component is isotropic with respect to the magnetic field orientation, whereas the broad component is responsible for the anisotropic character of these spectra. In Fig. 5.4 the anisotropic component of the EPR spectra is reported as a function of orientation of the applied magnetic field with respect to the [100] crystal axis. A sample with 0.2 mol % Cr doping was chosen to simplify the fitting procedure. At much lower Cr content the fitting is made unreliable by the presence of an additional anisotropic line due to Fe^{3+}, which is present at the impurity level of 40 molar ppm [39]. A sample of dimension of $0.5 \times 0.5 \times 0.5$ mm^3 was used in order to avoid contributions due to shape anisotropy. At $\theta = 0$ degree H is aligned along the [001] direction, and after a rotation by $\frac{\pi}{2}$ around [100] is aligned along the [010] direction. Because of the cubic structure of $SrTiO_3$ the initial and final directions are indistinguishable as shown by the spectra in Fig. 5.4. The relative weights of the isotropic and the anisotropic contributions were found to be $\simeq$40% and $\simeq$60%, respectively. This is constant for all the Cr concentrations analyzed (0.001 to 2 mol %). This indicates that the charge compensation mechanism causes a distortion at the Cr sites, and involves the full amount of Cr. The spectra reported in Fig. 5.3b indicate the presence of at least three components. The angular dependence of the signal shown in Fig. 5.4 can be understood by invoking an angular-dependent shift of these spectral components within a range of 5 Oe with respect to the central isotropic line. In order to study this angular dependence we use an effective spin Hamiltonian in the limit of weak-crystal field [24–26]. We used an axial crystal-field term (represented by the D parameter) in the spin Hamiltonian:

$$\mathcal{H} = \beta \overrightarrow{B} \cdot \widetilde{g} \cdot \overrightarrow{S} + h\ D(S_z^2 - \frac{1}{3} S \cdot (S+1)) \tag{5.1}$$

Here β is the Bohr magneton, $\overrightarrow{B}$ is the magnetic field, the $\widetilde{g}$ tensor is assumed to be isotropic ($g \approx 1.978$), $\overrightarrow{S}$ is the spin vector (S_x ,S_y ,S_z), h is the Planck constant, D is the crystal field operator describing the axial symmetry (here measured in GHz), and S is equal to $\frac{3}{2}$. The weak crystal field condition is obtained by the limiting condition of $D \ll\simeq\ 9.4\ GHz$ (the microwave energy used). Under this condition it is possible to solve the effective Hamiltonian with a perturbation approach and to obtain the following resonant magnetic fields for the three allowed transitions [40, 41]:

$$(-\frac{3}{2} \leftrightarrow -\frac{1}{2}): \quad B_{res} = B_0 + \Delta B_0\ (3\ cos(\theta)^2 - 1) \tag{5.2}$$

$$(-\frac{1}{2} \leftrightarrow +\frac{1}{2}): \quad B_{res} = B_0 \tag{5.3}$$

$$(+\frac{1}{2} \leftrightarrow +\frac{3}{2}): \quad B_{res} = B_0 - \Delta B_0\ (3\ cos(\theta)^2 - 1) \tag{5.4}$$

where

$$\Delta B_0 = \frac{h\ D}{g\ \beta}. \tag{5.5}$$

Equation (5.3) shows that an axial symmetry may have an isotropic line corresponding to the transition $-\frac{1}{2} \leftrightarrow +\frac{1}{2}$, and two anisotropic lines symmetrically distributed around the central line described by Eqs. (5.2) and (5.4). Moreover, the relative amplitude of the three spectral contributions are given by the square of the matrix element of the creation operator, S^+, between the projection states. The relative intensities of the transitions described above are 3:4:3, yielding a fraction of $\frac{4}{4+6}$ for the isotropic line and $\frac{6}{4+6}$ for the anisotropic line, in excellent agreement with our experimental observation of $\simeq$ 40% and 60%. By performing a fitting of the spectra obtained at different angles between the <001> crystal axes and H, we found a crystal field parameter D=8.3(8) MHz which is independent from the Cr concentration. This value corresponds to $\Delta B_{0(avg)}$=3.0(3) G.

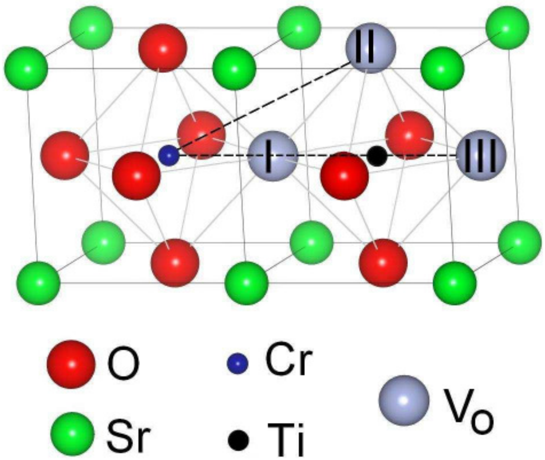

Figure 5.5: *Portion of the SrTiO$_3$ crystal structure showing the Cr ion and the possible V_O positions investigated: position I is excluded because it is inconsistent with the small value of the crystal-field parameter observed (D $\simeq$ 8 MHz); position II is inconsistent with the axial symmetry along the [100] direction; position III is consistent with the symmetry of the crystal field and the D value we measured.*

The reader is referred to the chapter 8 of this thesis for a detailed description of the fitting procedure. Strong axial crystal fields (D) of $\simeq$ 40 and $\simeq$80 GHz have been characterized for Fe^{3+}-V_O in $SrTiO_3$ and Cr^{3+}-V_O in WO_3 [42, 43]. Due to the strong valence bond character of the oxygen octahedra, a similar crystal field splitting (D value) should be observed in $SrTiO_3$ in case of an oxygen vacancy directly attached to the

Cr site (position I in Fig. 5.5). Because in our samples, the parameter D was observed to be $\simeq$ 8 MHz, this discrepancy suggests a positioning of V_O at next-neighbor sites along the <100> direction (position III in Fig. 5.5). The possibility of a V_O in the second coordination sphere (position II in Fig. 5.5) is excluded because this geometry leads to a symmetry that is inconsistent with our result (axial along [100]). As observed in the Cr/Nb-codoped sample, the Cr^{3+} ions are centered at sites of cubic symmetry, whereas in all reduced samples the Cr^{3+} ion exhibit an axial symmetry. This can be explained by the localization of a V_O at the 3th coordination sphere of each of the Cr^{3+} ions.

5.2 The charge compensation mechanism between the Cr^{3+} and the oxygen vacancy centers

In pure $SrTiO_3$ the formation of V_Os during a reduction process leads to filling of the Ti(3d) conduction band (CB) states and an insulator-to-metal transition at sufficiently high electron doping [30, 31]. We found that our thermal reduction process, described in chapter 2 (Ar/H_2 at 1150° for 6h), does not alter the insulating state of the crystal independently of the Cr doping.

Optical absorption (OA) spectra taken at room temperature enable a comparison between conducting and insulating $SrTiO_3$ [14, 30] (Fig. 5.6). The undoped oxidized sample is insulating and transparent in the near-infrared and visible range with an absorption edge at 3.2 eV, corresponding to the an indirect band gap transition of $SrTiO_3$ [44–47]. The highly reduced sample, annealed in vacuum, exhibits absorption below the band gap, which can be assigned to the presence of V_os and conducting electrons [30, 48]. However, the nominal pure $SrTiO_3$ crystals annealed in Ar/H_2 or O_2 (ambient pressure,

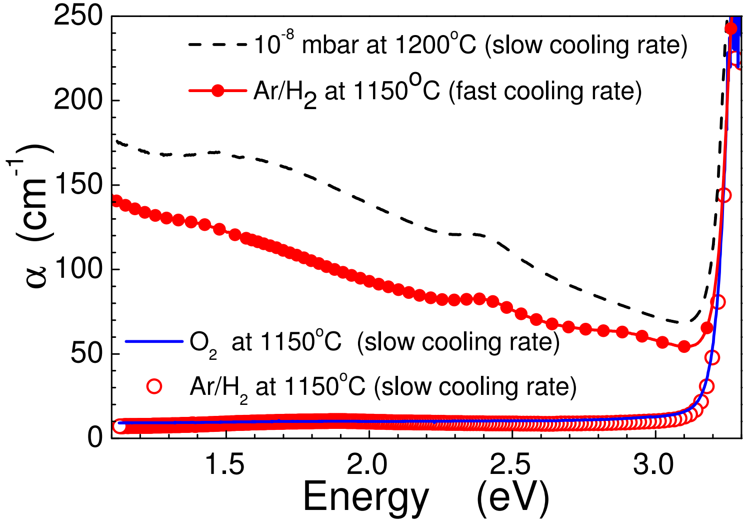

Figure 5.6: *Optical absorption spectra of nominally pure $SrTiO_3$ annealed in different atmospheres.*

at 1150°C for 6 h), show identical OA spectra. These two particular thermal treatments were performed with a relatively slow cooling rate ($\simeq$-200°C/h) from 1150°C to room temperature. The comparison of the spectra in Fig. 5.6 suggest that the Ar/H_2 annealing is not able to significantly change the conducting properties of pure $SrTiO_3$. However, if the sample is quenched (in $\leq$ 60 sec) from 1150°C to room temperature, the crystal became conducting and exhibits a similar OA spectrum as the pure $SrTiO_3$ annealed in high vacuum, as shown in Fig. 5.6. This means that at 1150°C a significant amount of V_o is introduced because of the reducing atmosphere of Ar/H_2, but the cooling process can produce different effects: the slow cooling rate ($\simeq$-200°C/h) assists the re-oxidation of the crystal due to presence of a residual partial pressure of O_2; the fast cooling (quenching) freezes V_o in the crystal. A different behavior was observed in the case of Cr-doped crystals. The

Ar/H_2 annealing causes the valence change of Cr from the 4+ to the 3+ state. Since Cr^{4+} ions are deep traps for CB electrons, at high temperature they capture electrons introduced by the V_o, and when the temperature is reduced slowly, the crystal is forced to keep an amount of V_o to compensate the charge trapped at the Cr^{3+} ions.

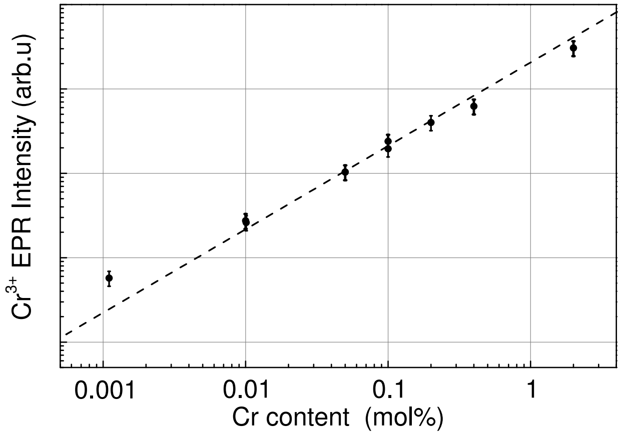

Figure 5.7: *Intensity of the EPR Cr^{3+} signal versus Cr content in reduced $SrTiO_3$. The linear behavior indicates that the Cr amount converted to the 3+ state is independent of the Cr concentration. The absence of any saturation process at high doping suggests that the full amount of Cr is always converted to the 3+ valence state.*

In the doping range investigated, i.e., up to 2 mol%, all Cr atoms convert to the 3+ valence state, as demonstrated by the linear dependence of the EPR intensities of Cr^{3+} versus the Cr concentration shown in Fig. 5.7. At a content $\leq$0.01 mol%, the average distance between the Cr centers is $\geq$ 10 unit cells.

Therefore, at this distance, an interaction between the Cr sites is expected to be negligible. As at all concentrations the Cr^{3+} centers exhibit the same axial symmetry, there must be a V_o perturbing each of the Cr sites. The absence of a saturation in the linear behavior suggests that the compensation arises from the effect of the thermal annealing on the Cr dopants and not from other impurities. Moreover, the linear behavior indicates that the charge compensation mechanism is the same at every doping level.

5.2.1 Cr^{3+} and oxygen vacancy complex

The study of the symmetry of the Cr^{3+} site allows to understand what is the origin of the charge compensation mechanism that changes the valence of the Cr ions to 3+. The electron captured by the Cr ion could arise from the V_O center nearby. In this case there should be an unpaired electron at the V_O center, or a Ti^{4+} should be converted to Ti^{3+}. In both cases the magnetic dipolar interaction of these centers with the Cr^{3+} ion could give rise to an axial symmetry. According to Fig. 5.5, this electron should have an average distance from the Cr^{3+} ion on the order of $R_D = 3 \times R_0$, where R_0 is the distance between the Cr ion and the oxygen atom at the first coordination sphere. The magnitude of the field produced by this unpaired electron at the Cr^{3+} site is given by the expression [26]

$$B \simeq \frac{g\ \beta}{R_D^3} \simeq 93\ \text{G}, \tag{5.6}$$

This value is one order of magnitude larger than our experimental value observed as the splitting $\Delta B_0 \sim 3$ G. This discrepancy is consistent with the fact that we did not observe any other paramagnetic center except that of the Cr^{3+}. We have to conclude that, if an unpaired electron is present at the V_o site (or in form of Ti^{3+}) there must be a strong phonon coupling which masks this paramagnetic center via a strong spin-phonon relaxation. Another possible explanation is that there are two kinds of V_o centers introduced by the Ar/H_2 annealing: double charged vacancies (V_o^{++}) which could be randomly distributed and compensate the charges of the electrons trapped by the Cr ions, and neutral V_os which are located at the 3rd coordination sphere of the Cr^{3+} ions. In the case of the neutral V_o center, the two electrons from the missing bond of the nearest Ti ions are localized at the two adjacent Ti^{3+} with antiparallel spins [49] as shown in Fig. 5.8. This particular spin configuration is EPR silent [50]. Both kinds of oxygen vacancies are consistent with the model of strongly localized two-electron and two-hole excitation proposed by Anderson [51].

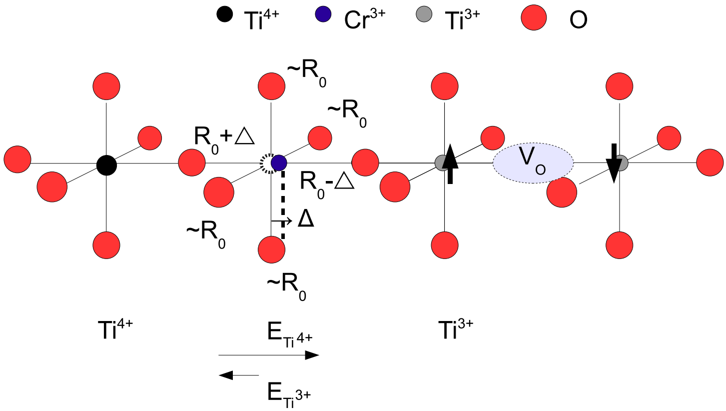

Figure 5.8: *Model of the Cr^{3+}-O-Ti^{3+}-V_o-Ti^{3+} complex in reduced Cr-doped $SrTiO_3$ with the Cr^{3+} ion displaced by the distance Δ from the original 4+ position. The electric field generated by the two adjacent Ti^{3+} and Ti^{4+}, maybe responsible of the displacement Δ.*

The proximity of the the Ti^{3+}-V_o-Ti^{3+} complex may be responsible of the breaking of the symmetry of the crystal field experienced by the Cr ion. As shown in Fig. 5.8, the Ti^{4+} repels the Cr^{3+} more than the nearest Ti^{3+}. The result of this Coulomb interaction produces a net attractive force on the Cr^{3+} toward the Ti^{3+}-V_o-Ti^{3+} complex. As a consequence, the Cr ion may result displaced from the center of the octahedron. Because of the strong covalent bond of the oxygen octahedron, we assume the displacement of the Cr ions as predominant reason of the axial symmetry. We now estimate the displacement of the Cr ion using the experimental value of the axial parameter D. For spin centers $S < 2$, Newman and Urban [52] have shown that D can be expressed as a simple sum over the contribution of the separate coordinated ligands (denoted n):

$$D = \bar{b}_2(R_0)\left(\frac{3}{2}\right)\sum_{1}^{6}\left(\frac{R_0}{R_n}\right)^{t_2}\left(\cos^2\Theta_n - \frac{1}{3}\right) . \qquad (5.7)$$

Here R_0 is distance between the Cr ion and the oxygen in an unperturbed octahedral site (Fig. 5.8), R_n is the distance between the Cr ion and the nth oxygen ligand in the distorted site, Θ_n is the angle between the line joining the paramagnetic ion with the nth ligand and main EPR axis, and $\bar{b}_2(R_0)$ and t_2 are coefficients that depend on R_0 and the nature of the ligand. These two coefficients have been evaluated by Müller and Berlinger [53] for Cr^{3+} on a metal 4+ site in $SrTiO_3$. In particular they replace the term $\bar{b}_2(R_0) \times (\frac{R_0}{R})^{t_2}$ in Eq. (5.7) with the function $\bar{b}_2(R)$, which can be approximated to a Lennard-Jones-type function described as [53]:

$$\bar{b}_2(R) = -A\left(\frac{R_0}{R}\right)^{n} + B\left(\frac{R_0}{R}\right)^{m} , \qquad (5.8)$$

where $R_0 = 1.95$ Å, $A = -9.7(1.3)\ \mathrm{cm}^{-1}$, $B = -7.4(1.2)\ \mathrm{cm}^{-1}$, and the two exponents m =10 and n =13.

From Eqs. (5.7) and (5.8) and the experimental D value, we calculated the displacement Δ (Fig. 5.8) of the Cr^{3+} as

$$D = \bar{b}_2(R_0 + \Delta) + \bar{b}_2(R_0 - \Delta) - 2\bar{b}_2(R_0) \ . \qquad (5.9)$$

We obtain $\Delta = 0.06(2)$ Å, which corresponds to a displacement of only 3%. This result is in excellent agreement with a previous study of the EPR signal of Cr^{3+} in $SrTiO_3$ under a static uniaxial stress reported by Müller and Berlinger [53]. They found a value of $\Delta B_0 \simeq 2.8$ G, extrapolated at zero stress, which compares with our results of $\simeq 3$ G. They suggest that this axial symmetry may be explained in terms of a displacement of the Cr ion out of the center of the octahedral site along one of the <100> directions. Here we demonstrate that the axial symmetry is not an intrinsic property of the Cr^{3+}, but is a consequence of the nature of the charge compensation which generates the Cr^{3+} sites caused by the V_os. In the Cr/Nb-codoped crystal, with only Nb as a donor the Cr^{3+} remains in the center of a cubic site, whereas in the case of V_o compensation it shifts from the center. Other complexes of TM ions and V_os where the oxygen vacancy is located in the first coordination sphere have been found in $SrTiO_3$, for example Fe^{3+}-V_o [54], Mn^{2+}-V_o [42], and Ni^{3+}-V_o [50]. However, the Cr^{3+}-V_o complex has never been observed with the V_o at the first coordination sphere. This fact may be explained in terms of the interaction between the Cr ion and the V_o. Once the Cr^{4+} traps an electron and becomes Cr^{3+}, the Coulomb interaction with the Ti^{3+} minimizes the energy to form the structure presented in Fig. 5.8. This particular complex could be the reason why all the reduced Cr-doped $SrTiO_3$ crystals we studied were insulating.

Chapter 6

Charge transfer processes

In this chapter evidence for a charge-transfer process between the Cr^{3+} and the conduction band is presented. This processes is involved during the EC process and the resistive switching. The combination of EPR measurements, and current-voltage measurements show that the Cr ions act as reversible trap/detrap centers for the conducting electrons.

6.1 The R-line of Cr^{3+}

In the previous chapter, it was shown that the annealing in Ar/H_2 at 1150° forces the full amount of Cr-dopants to change the valence state from 4+ to 3+. It is known that photo-excitation above 1.8 eV can promote an electron from the Cr^{3+} ion to the conduction band (CB) [55]. Vice versa a CB electron, when trapped by Cr^{4+}, will form an excited Cr^{3+} state ($^2E_{2g}$), which subsequently relaxes to the ground state ($^4A_{2g}$) via the radiative transition (luminescence) $^2E_{2g} \rightarrow {}^4A_{2g}$. This emission is known as the R-line of Cr^{3+} in a octahedral crystal field [56–58].

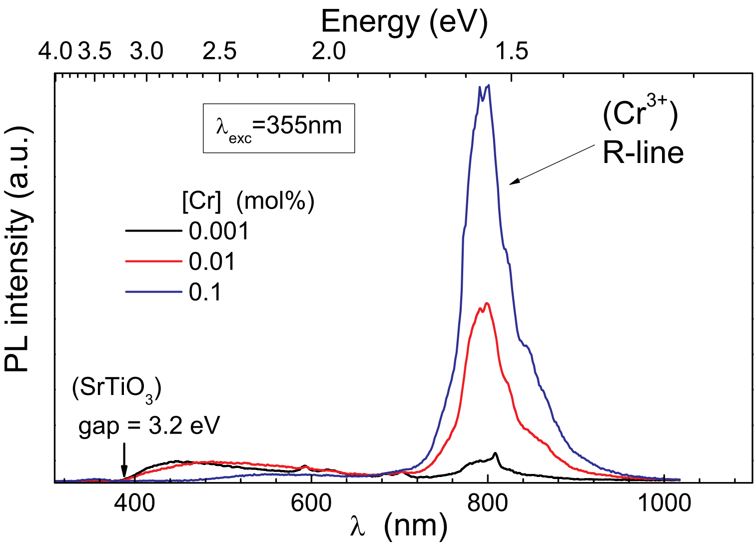

Figure 6.1: *Photoluminescence spectra of Cr^{3+}-doped $SrTiO_3$. The luminescence was excited at λ = 355 nm. The spectral line centered at 790 nm is known as R-line of Cr^{3+} in an octahedral crystal field.*

Figure 6.1 shows the R-line spectra obtained under a laser excitation of 355 nm for different Cr-doping levels. The broad linewidth of such a spectrum is assigned to a strong phonon-coupling involved in the radiative emission (vibronic transition) [56]. The time scale of the recombination process changes from seconds to hours depending on the Cr concentration. The slow recombination kinetics results from the capture of electrons at different traps below the CB, and by their thermally activated liberation [55].

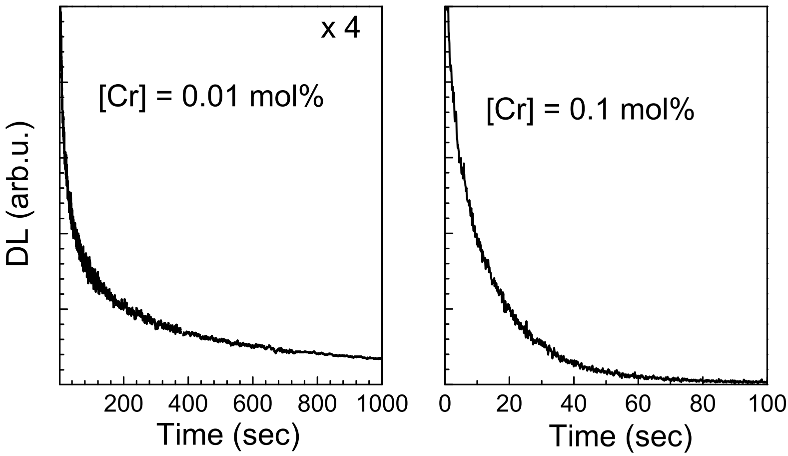

Figure 6.2: *Delayed luminescence (DL) of the Cr^{3+} in Cr-doped $SrTiO_3$ single crystals as a function of time. The intensity was recorded by means of a single photocounting module (SPCM) after switching off the laser.*

Figure 6.2 shows the time-resolved delayed luminescence (DL) measured after switching off the laser. In the higher doping case (0.1 mol%) the recombination is faster because of the higher amount of Cr (trap centers). These processes will be further described in the next sections, where the luminescence will be shown with a simultaneous current measurement and the measurement of the Cr^{3+} EPR intensity (time-resolved).

6.2 The reference marker

It is common to use a reference marker to enhance the precision to assign the spectroscopic peak positions of EPR lines. The operating frequency is fixed by the resonant cavity and is measured with a relative error of 10^{-6}. The main error in finding the peak position arises from the H field which induces the Zeeman energy splitting. This field is affected by an absolute error of typically $\pm$ 0.1 Oe, which arises from the accuracy of the set current in the magnet coils (see Par. 4.1). However, the increments (ΔH) during the sweep of the magnetic field, are much more precise than the absolute value of H. It is possible to determine the resonant field with an error $<$ 0.01 Oe by measuring the relative distance of a resonance peak with respect to a reference marker. In this work, a 2,2-Diphenyl-

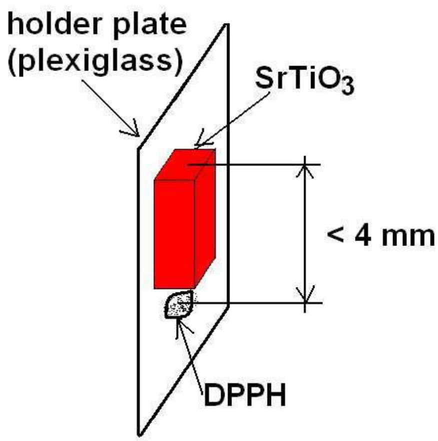

Figure 6.3: *Schematic diagram of the sample installation. The DPPH reference marker sample was mounted 1 mm below the $SrTiO_3$ crystal. To protect the DPPH from the laser irradiation, it was covered by teflon tape.*

1-Picrylhydrazyl (DPPH) sample was used both as standard for the intensity and as a reference resonance marker. Figure 6.3 schematically shows how the $SrTiO_3$ sample and the DPPH sample (reference) were mounted. The signal of the DPPH is not affected by the voltage which is applied to the $SrTiO_3$ sample.

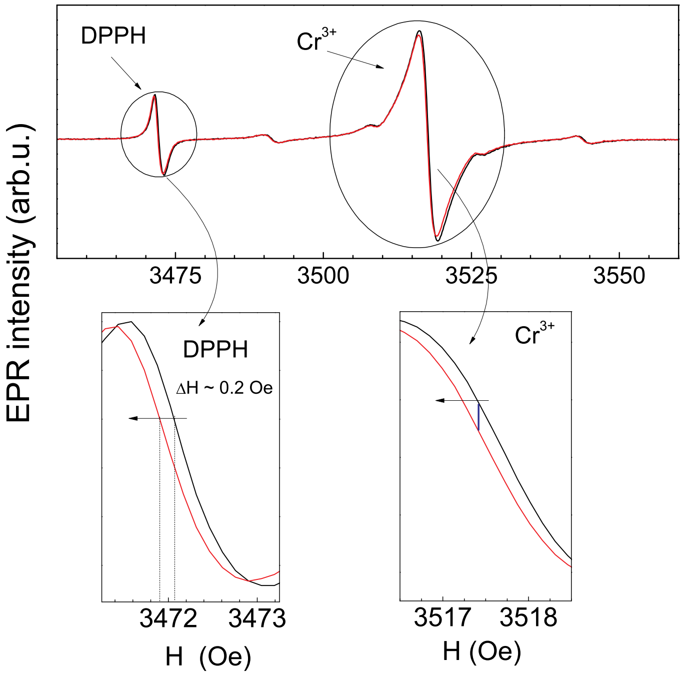

Figure 6.4: *EPR spectra of Cr^{3+} of Cr-doped $SrTiO_3$ single crystal ([Cr] = 0.1 mol%): (black line) spectrum detected in the dark; (red line) spectrum detected under laser illumination ($\lambda \simeq 633$ nm). The comparison between the spectra of the DPPH indicates a shift of the spectra caused by the error (accuracy) of the field H.*

Furthermore, it is protected from the laser irradiation since it is fixed 1 mm away from the focal point of the laser (laser beam $\simeq$ 1 mm diam.).In addition, it is covered by several layers of teflon. Figure 6.4 shows the comparison between the spectrum of the virgin sample (measured after storing it in the dark for 24 h), and a spectrum of the same sample under laser irradiation. The small change of the EPR intensities of the DPPH signal indicates a change of the cavity tuning which affects the intensity of all the measurements. However, by scaling the EPR signals to the intensity of the DPPH signal, it is possible to correct such a change. Moreover, the absolute error of H manifests itself in a shift of the full spectra, and this artefact can be corrected by using the DPPH signals to shift the spectra.

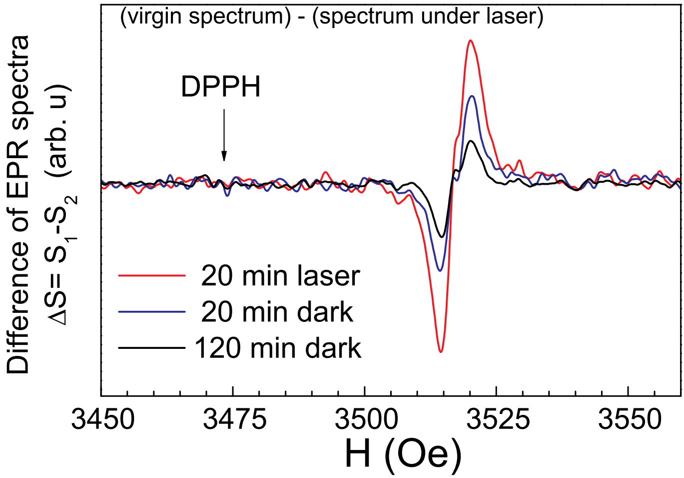

Figure 6.5: *Difference between EPR spectra of the Cr^{3+} signal in a Cr-doped $SrTiO_3$ single crystal ([Cr] = 0.1 mol%). The spectra were shifted and scaled to the DPPH signal. Under laser irradiation a decrease of $\simeq$ 3% of the Cr^{3+} signal is detected.*

The spectra, recorded under laser illumination and after switching off the laser, were subtracted from the spectrum of the crystal as shown in Fig. 6.5. Under laser irradiation the Cr^{3+} signal decreases of $\simeq$ 3%, while after turning off the irradiation, the signal slowly recovers back, according to the recombination process described at the beginning of this chapter [55]. Only after storing the sample in the dark for 24h the signal recovers completely to the initial intensity.

6.3 Time-resolved EPR signal

By fixing the magnetic field H corresponding to the maximum peak of the Cr^{3+} signal (central line) it is possible to monitor changes of the EPR signal as a function of time. Figure 6.6 shows the effect of the laser irradiation (633 nm /$\simeq$1.96 eV) on the EPR signal.

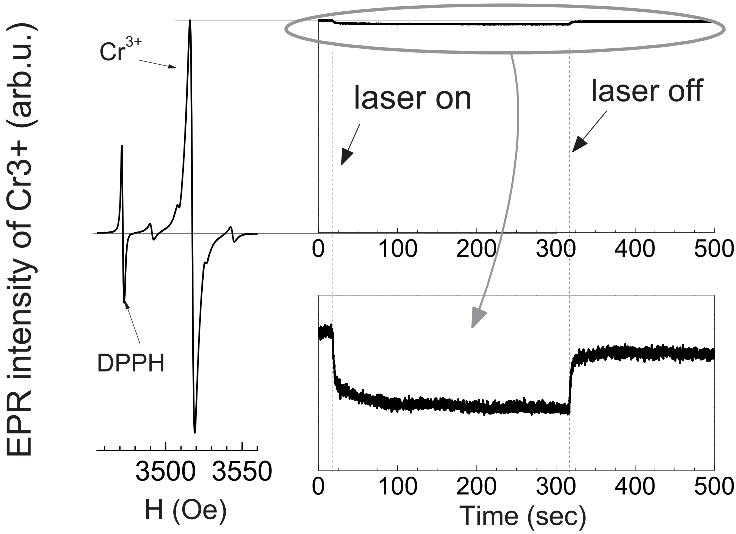

Figure 6.6: *Effect of the laser irradiation (λ 633nm) on the EPR signal of Cr^{3+} in Cr-doped $SrTiO_3$ ([Cr] = 0.1 mol %).*

As discussed in the previous sections the laser irradiation with a photon energy above 1.8 eV promotes electrons from Cr^{3+} to the CB. This process can be directly observed in the time dependence of the photo-current and the EPR signal of Cr^{3+} under laser irradiation. This is shown in Fig. 6.7 for a virgin crystal with 0.1 mol% of Cr at fixed bias voltage of 50 V. The photo-current under laser illumination is accompanied by a decrease of the Cr^{3+} signal. After stopping the irradiation, the CB electrons recombine at the Cr centers, as evidenced by the recovery of the EPR signal. Simultaneously, the current drops rapidly to the initial value. This anticorrelation is a direct proof of selective transfer of electrons between the Cr ions and the CB.

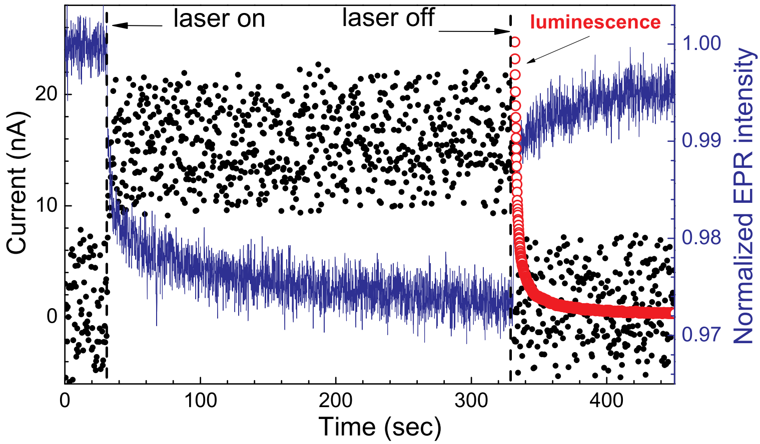

Figure 6.7: *Photocurrent (black bullets) and EPR intensity of Cr^{3+} in Cr-doped $SrTiO_3$ (blue line) as a function of time for a bias voltage of 50 V and laser irradiation (λ = 633 nm). When the laser is turned off, the delayed luminescence arising from the R-line of Cr^{3+} is recorded (red open circles).*

Further evidence of this recombination process is provided by the delayed luminescence (DL) which accompanies the recovery of the EPR signal (Fig. 6.7). This emission arises when a CB electron is trapped by Cr^{4+}, forming Cr^{3+} in an excited state ($^2E_{2g}$), which subsequently relaxes radiatively via the $^2E_{2g} \rightarrow {}^4A_{2g}$ transition (R-line see Fig. 6.8) [3, 55, 56]. A part of the electrons recombines fast, and the rest needs a longer time to diffuse until they recombine at Cr sites. Accordingly, the recovery of the EPR signal exhibits two components: a fast one correlated with the current drop, and a slow one also visible in the DL measurements. The EPR signal allows to estimate that roughly half of the electrons recombine promptly, whereas the remainder recombines with a very long decay time.

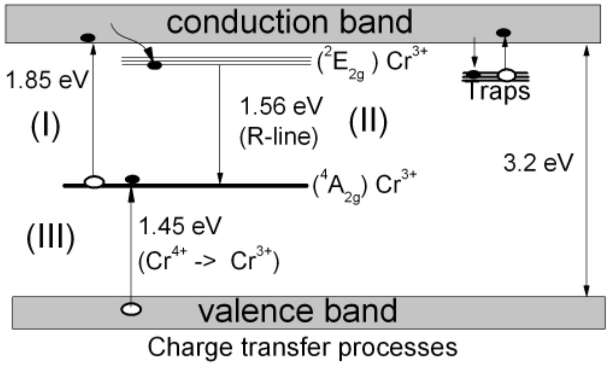

Figure 6.8: *Diagram of transition energies and charge transfer processes involving Cr^{3+} ions in Cr-doped $SrTiO_3$. Adapted from Basun et al. [55].*

The slow recombination kinetics was proposed by Basun et *al.* [55] to originate from the capture of electrons at trap centers (below the CB) which are not related to the Cr. The trapped electrons are released by thermally activated process and/or by IR irradiation (<1 eV) [55]. Figure 6.8 shows an additional charge-transfer process (III) from the valence band (VB) to Cr^{4+}, resulting in the increase of the Cr^{3+} concentration and creation of holes in the VB. Since in the virgin sample all Cr ions are in the 3+ state at the beginning of the irradiation, process III is negligible. However, the creation of Cr^{4+} via processes I will be balanced via process II and III as shown by the asymptotic approach to a steady state in the EPR signal (see Fig. 6.7). The rate of recombination of process II is controlled by the diffusion of electrons from the traps. The time to reach 90% of both, EPR signal decay and recovery, is comparable and of the order of 80 sec.

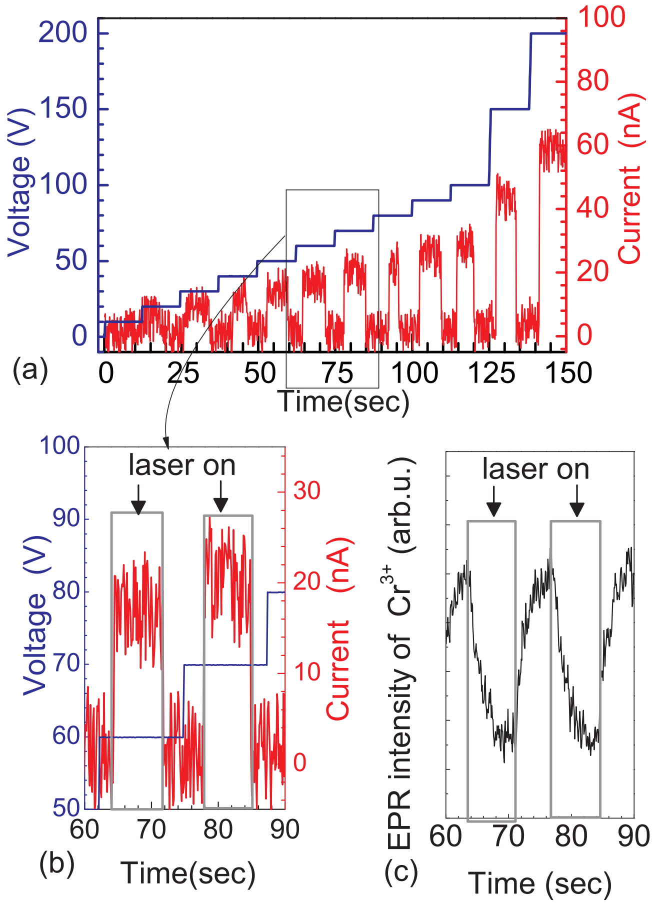

Figure 6.9: *Current and Cr^{3+} EPR intensity measurements in Cr-doped $SrTiO_3$. (a) Current measurement time-resolved at different applied voltage during an On and Off laser irradiation sequence: (b) a current is detectable only when laser is turned On; (c) the EPR intensity of Cr^{3+} is detected simultaneously with the current measurement. The EPR intensity is independent from the applied voltage.*

Figure 6.9 shows the results of an experiment that further clarifies how Cr^{3+} influences the transport property in the virgin $SrTiO_3$ crystals. This EPR experiment consists of a simultaneous measurement of the electrical current when the bias voltage is progressively increasing. During the increase of the bias voltage, each value of the bias was kept constant for a time long enough to observe the effect of laser irradiation (on and off sequences). An electrical current is detectable only when the laser is turned on (Fig. 6.9b). Independently of the applied voltage (electric field $\leq 10^4$ V/cm), the decrease of the intensity of the Cr^{3+} EPR signal is only a function of the laser illumination (Fig. 6.9c).

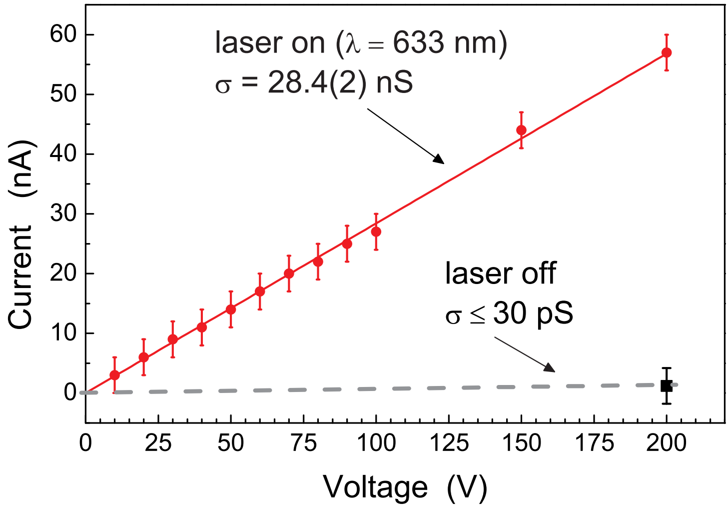

Figure 6.10: *Current voltage characteristics of a reduced Cr-doped $SrTiO_3$ crystal ([Cr]=0.1 mol%).*

This correlation indicates that the photocurrent produced by the red laser is mainly dominated by the extraction of electrons from Cr^{3+} ions. This is clearly summarized in Fig. 6.10, where the current values, measured at different bias voltage, are recorded under laser irradiation and in the dark, as a function of the voltage. Two conducting states are distinguishable in the dark and under illumination. Thus, we can conclude that the Cr^{3+} ions act as a reservoir of electrons, which can be promoted to the conduction band (CB) by photo-excitation. If the applied electric field remains below 10^4 V/cm the charge-transfer process observed is fully reversible, and when the laser is turned off, the electrons recombine as shown in Fig. 6.9c by the recovery of the EPR signal.

6.4 The electro-conditioning procedure

At high initial resistance ($\simeq$30 GΩ), process I of Fig. 6.8 provides the carriers necessary to initiate the EC. For prolonged application of a bias voltage ($\geq 10^4$ V/cm) under continuous photo-excitation the current will increase, and the voltage is adjusted to minimize the power load and prevent damage. Once the final conducting state is reached, the intensity of the Cr^{3+} signal drops irreversibly to a lower level. Figure 6.11 shows the integral of the Cr^{3+} EPR spectra of samples in the insulating and the conducting state for a doping level of 0.1 mol% and 0.2 mol%, in which the EC process leads to a final resistance of 0.25 kΩ and 3 kΩ, respectively. It can be seen that the total amount of Cr^{3+} is lowered by $\simeq$20 %.

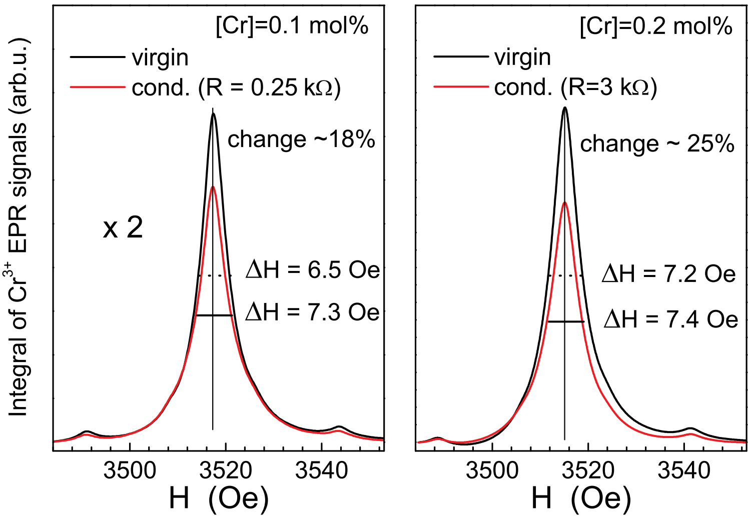

Figure 6.11: *Integral of the Cr^{3+} EPR signal in Cr-doped $SrTiO_3$ vs. magnetic field H. Comparison between the virgin (black line) and conducting crystals (red line).*

This can be regarded as a measure of the crystal volume in which an irreversible modification occurred. The comparison between the virgin and conducting samples shows an increase of the full width at half maximum (FWHM) of $\Delta H \simeq 1$ Oe in the sample with 0.1 mol% of Cr. For the sample with higher doping level (Fig. 6.11b), the FWHM remains apparently unchanged, because the linewidth is already broadened owing to the higher Cr content. The lineshape of the latter, however, is clearly asymmetric after the EC, indicating a small distortion of the Cr environment. Such a distortion starts to be visible in the spectra obtained as a difference with respect to the spectrum of the virgin sample at the beginning of the EC process. Figure 6.12 shows these differences for different applied electric fields under laser irradiation.

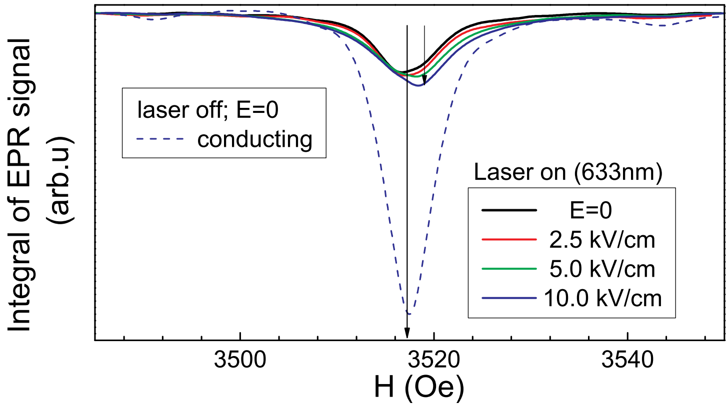

Figure 6.12: *EPR spectra of Cr^{3+} in Cr-doped $SrTiO_3$. The spectra are obtained by subtracting the spectrum measured (in the same sample) in the dark at $E = 0$ before the EC process.*

The spectrum obtained for E=0 has a symmetric lineshape, whereas the other spectra of the differences show a systematical distortion, which grows with the increasing applied voltage. This fact suggests that the applied voltage induce a distortion of the Cr^{3+} site, which remains permanent in the final conducting state (dashed line). In addition, there is evidence of electronic structural changes, as indicated by the different response to the laser illumination (without bias voltage) in the virgin state and the conducting state. Figure 6.13 shows that in this case the Cr^{3+} signal increases under laser exposure, whereas in the virgin state it decreases ([Cr]=0.1 mol%, same crystal as in Fig. 6.7). Process III (Fig. 6.8) explains this increase as a conversion of Cr^{4+} to Cr^{3+}. Therefore, the $\simeq$20% reduction of the Cr^{3+} signal in the conducting state is a proof of the creation of Cr^{4+} centers during the EC process.

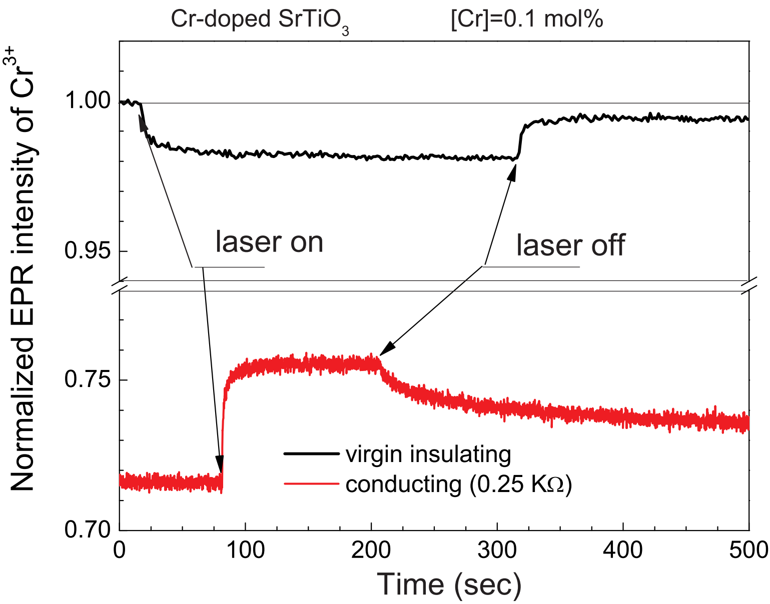

Figure 6.13: *Time-resolved EPR intensity of Cr^{3+} in Cr-doped $SrTiO_3$ under laser exposure and without bias voltage for a sample in the virgin (black line) or conducting (red line) state.*

Apparently, the presence of mixed valencies of the Cr ions is necessary to create the conducting state. In oxidized samples, all Cr ions are in the 4+ valence state and no electron donors are present. Moreover, the Cr^{4+} ions act as electron traps, which explain why these samples cannot be brought into the conducing state through EC.

6.5 Electroluminescence during resistive switching

Upon the EC procedure the resistance typically decreases from the GΩ to the kΩ range, where IV loops begin to exhibit hysteretic behavior. In this state it is possible to see a current induced luminescence, namely electroluminescence (EL), by recording the spectra during multiple hysteresis loops.

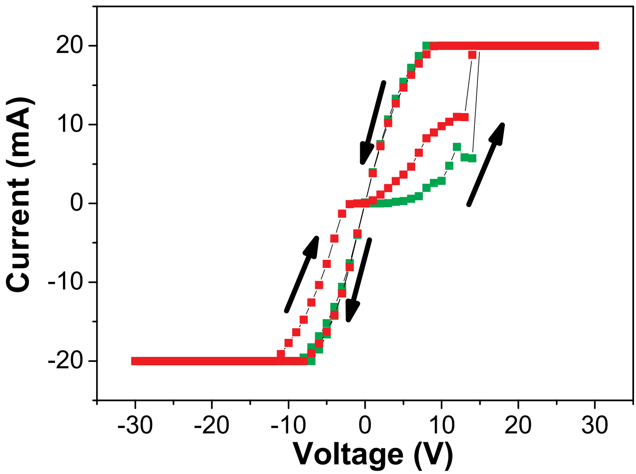

Figure 6.14: *Two current-voltage (IV) loops in Cr-doped conducting $SrTiO_3$ ([Cr]=0.2 mol%). The two loops are represented with two different color: red and green. The IV loops show the transition from a LR to a HR state at negative polarity.*

Figure 6.14 shows two IV loops with transition from the LR to the HR state at negative polarity. The EL spectra shown in Fig. 6.15 were recorded separately for each "write" (positive branch) and "erase" (negative branch) half loop of the IV.

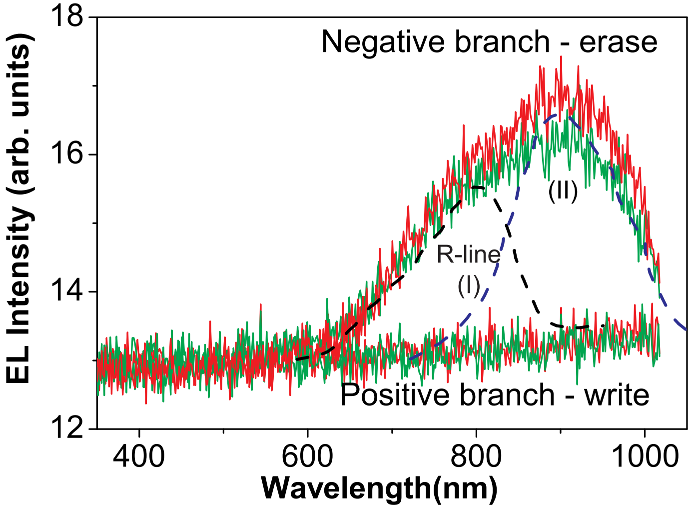

Figure 6.15: *Electron-luminescence (EL) spectra in Cr-doped conducting $SrTiO_3$ ([Cr]=0.2 mol%). The spectra were recorded during two different IV loops (red an green as in Fig. 6.14) for each "write" (positive branch) and "erase" (negative branch) half loop of the IV measurement the. The occurrence of the luminescence only at the erasing branch clearly indicates that this luminescence is correlated with a recombination process that decreases the number of conducting electrons.*

The spectra are broadened, suggesting a superposition of two emission lines (I an II in Fig. 6.15). A component (I) is still the R-line (at 790 nm), already observed in the DL of the virgin sample and in the EC process, when the conductivity was four orders of magnitude lower. This implies that in the conducting state the charge-transfer processes via the Cr band-gap states play a significant role in the electronic transport. Another component (II) at lower energy is visible in the spectrum (at $\simeq$900 nm). A band in this energy range has actually been observed by optical excitation in numerous compounds with

Cr dopants at octahedral lattice sites [59–64] and is assigned to the $^4T_2 \rightarrow {}^4A_{2g}$ transition.

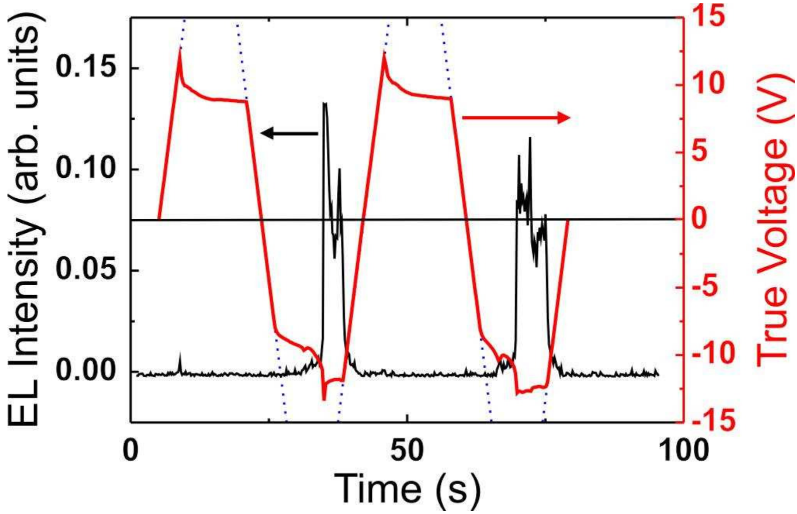

Figure 6.16: *Simultaneous time-resolved luminescence (black line) and IV loops on a single crystal of SrTiO3:Cr 0.2mol%. The abrupt changes of the true applied voltage curve (red line) observed in the negative branch of the hysteresis curve indicate that the onset of EL coincides with an abrupt decrease in the conductance. The true voltage deviates from the nomina voltage (dashed line) at the compliance level of the current (see Fig. 6.14a).*

The occurrence of the luminescence only in the erasing branch of the IV clearly indicates that this luminescence is correlated with a recombination process which decreases the amount of conducting electrons. Simultaneous time resolved luminescence (black) and voltage loops on a single crystal of $SrTiO_3$:Cr 0.2 mol % are shown in Fig. 6.16. The abrupt changes in the real applied voltage vs. time (red) during the negative branch of the hysteresis are indicating a resistance change coincident with the start of strong EL. We report an essential process describing the decrease of conductivity during the resistive switching, which involves the Cr site as a center which is reversibly trapping/detrapping the conducting electrons. Our luminescence measurements performed on SrTiO3:Cr crystals at different stages of conductivity reveal that there is light emission associated with 3d intrashell transitions of Cr^{3+} in an octahedral lattice site during both the EC process and the resistive switching. With increasing conductivity of $SrTiO_3$ the emission maximum shifts from the R-line to the $^4T_2 \rightarrow {}^4A_{2g}$ transition (see Fig. 6.15). We interpret this as being due to a geometrical change of the oxygen octahedron, through either a distortion and/or a modified oxygen vacancy distribution. The EL in the final state, which occurs only when the memory cell is switched from the LR to the HR state, can provide an important stimulus for the refinement of theoretical models taking controlled and defined trapping centers into account.

Chapter 7

Concluding remarks

Many models have been proposed for the resistance switching in perovskite oxides [2–5, 18]. However, at present, unresolved basic issues are: current-induced or field-induced insulator-to-metal transition, the role of the ferroelectricity, the electron correlation, the role of defects, the role of controlled impurities like Cr ions and oxygen vacancies (V_O). In this scenario we found some basic phenomena, which can provide an important stimulus for the refinement of theoretical models by taking controlled and defined trapping centers into account.

EPR characterization of the Cr^{3+} center

Our EPR study of Cr-doped $SrTiO_3$ single crystals reveals an axial symmetry of the Cr site, when the valence state is forced to be 3+ via a charge compensation through the formation of oxygen vacancies. We found evidence of the presence of two kinds of V_O centers introduced by the Ar/H2 annealing: double charged vacancies (V_O^{++}s) which could be randomly distributed and compensate the charges of the electrons trapped by the Cr ions, and neutral V_Os which are located at the 3rd coordination sphere of the Cr^{3+} ions. The proximity of the the Ti^{3+}-V_O-Ti^{3+} complex may be responsible of the breaking of the symmetry of the crystal field experienced by the Cr ion.

Other complexes of TM ions and V_os where the oxygen vacancy is located in the first coordination sphere have been found in $SrTiO_3$, for example Fe^{3+}-V_o [54], Mn^{2+}-V_o [42], and Ni^{3+}-V_o [50]. However, the Cr^{3+}-V_O complex has never been observed with the V_o at the first coordination sphere. This fact may be explained in terms of the interaction between the Cr ion and the V_o. Once the Cr^{4+} traps an electron and becomes Cr^{3+}, the Coulomb interaction with the Ti^{3+} minimizes the energy to form the Cr^{3+}-O-Ti^{3+}-V_o-Ti^{3+} complex. Thus we identify a linear complex which is unique in its structure, and which, furthermore, might account for the stabilization of the insulating state in reduced Cr-doped $SrTiO_3$ crystals.

EPR time-resolved: charge-transfer during the EC process

Through EPR studies we observed the excitation of electrons from the Cr^{3+} ions to the CB via a decrease of the Cr^{3+} signal and a simultaneous increase of the electrical current at fixed bias voltage. We concluded that the Cr^{3+} ions present in the virgin insulating samples are responsible for the photocurrent, which initiates the EC process. The decrease of the Cr^{3+} EPR signal by ∼20% in the conducting state indicates creation of Cr^{4+} ions, which act as trap centers for the carriers. Apparently the presence of mixed valences of the Cr ions is necessary to create the conducting state.

A small distortion of the EPR line of Cr^{3+} was observed. We ascribe the change of the lineshape to a small distortion of the oxygen octahedron surrounding the Cr^{3+}. This result is not in agreement with the creation of Cr^{3+}-V_O complexes induced by the EC process, which have been observed from high resolution imaging of X-ray absorbtion at the pre-edge energy of the K-edge of Cr [4]. However, because EPR is a bulk sensitive technique, we cannot exclude the formation of such complexes at the electrode interface .

Luminescence: charge-transfer during the resistive-switching

Electrically stimulated light emission was observed during the decreasing of conductivity in the resistive-switching loop. This luminescence can be taken as proof of dynamic processes involving trapping and subsequent radiative decay of electrons at the Cr dopant sites. With increasing conductivity, achieved during the EC process, the emission maximum shifts from the R-line to the $^4T_2 \rightarrow {}^4A_{2g}$ transition. The latter is associated with a change in orbital occupancy, and its energy shift can be related to a structural change of the oxygen octahedron, either through distortion and/or a modified oxygen-vacancy distribution.

Bibliography

[1] Y. Watanabe, *Epitaxial all-perovskite ferroelectric field effect transistor with a memory retention*, Appl. Phys. Lett. **66**, 1770 (1995).

[2] C. H. Ahn, J. M. Triscone, and J. Mannhart, *Electric field effect in correlated oxide systems*, Nature **424**, 1015 (2003).

[3] S. F. Alvarado, F. La Mattina, and J. G. Bednorz, *Electroluminescence in SrTiO3:Cr single-crystal nonvolatile memory cells*, Appl. Phys. A **89**, 85 (2007).

[4] M. Janousch, G. I. Meijer, U. Staub, B. Delley, S. F. Karg, and B. P. Andreasson, *Role of Oxygen Vacancies in Cr-Doped SrTiO3 for Resistance-Change Memory*, Advanced Materials **19**, 2232 (2007).

[5] Y. Watanabe, *Review of Resistance Switching of Ferroelectrics and Oxides in Quest for Unconventional Electronic Mechanisms*, Ferroelectrics **349**, 190 (2007).

[6] H. F. Hamann, M. O'Boyle, Y. C. Martin, M. Rooks, and H. K. Wickramasinghe, *Ultra-high-density phase-change storage and memory*, Nature Materials **5**, 383 (2006).

[7] W. R. Hiatt and T. W. Hickmott, *Bistable Switching in Niobium Oxide Diodes*, Appl. Phys. Lett. **6**, 106 (1965).

[8] G. Argall, *Switching Phenomenon in Titanium Oxide Thin Films*, Solid-State Electron. **11**, 535 (1968).

[9] K. L. Chopra, *Avalanche-Induced Negative Resistance in Thin Oxide Films*, J. Appl. Phys. **36**, 184 (1965).

[10] J. C. Bruyere and B. K. Chakraverty, *Switching and Negative Resistance in Thin Films of Nickel Oxide*, Appl. Phys. Lett. **16**, 40 (1970).

[11] Y. You, B. S. So, J. H. Hwang, W. Cho, S. S. Lee, T. M. Chung, C. G. Kim, and K. S. An, *Impedance spectroscopy characterization of resistance switching NiO thin films prepared through atomic layer deposition*, Advanced Materials **89**, 22210 (2006).

[12] M. J. Lee, S. Seo, D. C. Kim, S. E. Ahn, D. H. Seo, I. K. Yoo, I. G. Baek, D. S. Kim, I. S. Byun, S. H. Kim, I. R. Hwang, J. S. Kim, S. H. Jeon, and B. Park, *A Low-Temperature-Grown Oxide Diode as a New Switch Element for High-Density, Nonvolatile Memories*, Advanced Materials **19**, 73 (2007).

[13] R. Jung, M. Lee, S. Seo, D. C. Kim, G. Park, K. Kim, S. Ahn, Y. Park, I. Yoo, J. Kim, and B. H. Park, *Decrease in switching voltage fluctuation of Pt/NiO_x /Pt structure by process control*, Appl. Phys. Lett. **91**, 022112 (2007).

[14] A. Beck, J. G. Bednorz, C. Gerber, C. Rossel, and D. Widmer, *Reproducible switching effect in thin oxide films for memory applications*, Appl. Phys. Lett. **77**, 139 (2000).

[15] Y. Watanabe, D. Sawamura, and M. Okano, *Recurrent local resistance breakdown of epitaxial BaTiO3 heterostructures*, Appl. Phys. Lett. **72**, 2415 (1998).

[16] K. Szot, W. Speier, G. Bihlmeyer, and R. Waser, *Role of Oxygen Vacancies in Cr-Doped SrTiO3 for Resistance-Change Memory*, Nature Mater. **5**, 312 (2006).

[17] C. Rossel, G. I. Meijer, D. Bremaud, and D. Widmer, *Electrical current distribution across a metal-insulator-metal structure during bistable switching*, J. Appl. Phys. **90**, 2892 (2001).

[18] M. J. Rozenberg, I. H. Inoue, and M. J. Sánchez, *Nonvolatile Memory with Multilevel Switching: A Basic Model*, Phys. Rev. Lett. **91**, 178302 (2004).

[19] F. La Mattina, J. G. Bednorz, S. F. Alvarado, A. Shengelaya, and H. Keller, *Detection of charge transfer processes in Cr-doped $SrTiO_3$ single crystals*, Appl. Phys. Lett. **93**, 022102 (2008).

[20] R. C. Weast, *Handbook of Chemistry and Physics*, 57^{th} edition CRC PRESS, 1976.

[21] *Powder Diffraction File (Inorganic Phases)*, International Centre for Diffraction Data (JCPDS).

[22] W. G. Pfan, *Zone Melting*, John Wiley & Sons Inc., 1966.

[23] H. J. Zeiger and G. W. Pratt, *Magnetic interaction in solids*, Clarendon Press · Oxford, 1973.

[24] A. Abragam and B. Bleaney, *Electron paramagnetic resonance of transition ions*, Oxford Univeristy Press, 1970.

[25] G. E. Pake, *Paramagnetic Resonance – An introduction monography.*, Benjamin W.A., 1962.

[26] J. E. Wertz, *Electron Spin Resonance. Elementary Theory and Practical Applications.*, Chapman and Hall, 1986.

[27] R. Lacroix and G. Emch, *Covalence et resonance paramagnetique*, Helv. Phys. Acta **35**, 592 (1962).

[28] R. Lacroix, U. Höchli, and K. A. Müller, *Strong Field g-value Calculation for d^7 Ions in Octahedral Surraundings*, Helv. Phys. Acta **137**, 627 (1964).

[29] C. P. Poole, *Electron Spin Resonance: A Comprensive Treatise on Experimental Techniques/Second Edition*, Curier Dover Publications., 1996.

[30] W. S. Baer, *Free-Carrier Absorption in Reduced $SrTiO_3$*, Phys. Rev. **144**, 734 (1966).

[31] G. Binnig, A. Baratoff, H. E. Hoenig, and J. G. Bednorz, *Two-Band Superconductivity in Nb-Doped $SrTiO_3$*, Phys. Rev. Lett. **45**, 1352 (1980).

[32] L. Pellegrino, I. Pallecchi, D. Marre, E. Bellingeri, and A. S. Siri, *Fabrication of submicron-scale $SrTiO_{3-\delta}$ devices by an atomic force microscope*, Appl. Phys. Lett. **81**, 3849 (2002).

[33] D. A. Müller, N. Nakagawa, A. Ohtomo, J. L. Grazul, and H. Y. Hwang, *Atomic-scale imaging of nanoengineered oxygen vacancy profiles in $SrTiO_3$*, Nature **430**, 657 (2004).

[34] D. D. Cuong, B. Lee, K. M. Choi, H.-S. Ahn, S. Han, and J. Lee, *Oxygen Vacancy Clustering and Electron Localization in Oxygen-Deficient $SrTiO_3$: LDA + U Study*, Phys. Rev. Lett. **98**, 115503 (2007).

[35] F. Cordero, *Hopping and clustering of oxygen vacancies in $SrTiO_3$ by anelastic relaxation*, Phys. Rev. B **76**, 172106 (2007).

[36] R. H. Hoskins and B. H. Soffer, *9.6 GHz and 34GHz electron paramagnetic resonance studies of chromium-doped forsterite*, Phys. Rev. **133**, A490 (1964).

[37] D. E. Budil, D. G. Park, J. M. Burlitch, R. F. Geray, R. Dieckmann, and J. Freed, *9.6 GHz and 34 GHz EPR studies of Chromium-Doped Forsterite*, J. Chem. Phys. **101**, 3538 (1994).

[38] K. A. Müller, *Resonance paramagnetique du Cr^{3+} dans des monocristaux de $SrTiO_3$*, Arch. Sci. (Geneve) **12**, 122 (1958).

[39] W. I. Dobrov, R. F. Vieth, and M. E. Browne, *Electron Paramagnetic Resonance in $SrTiO_3$*, Phys. Rev. **115**, 79 (1959).

[40] B. Bleaney, *Hyperfine structure in paramagnetic resonance*, Physica **17**, 175 (1951).

[41] B. Bleaney and D. J. E. Ingram, *The Paramagnetic Resonance Spectra of Two Salts of Manganese*, Proc. Roy. Soc. A **205**, 336 (1951).

[42] E. S. Kirkpatrick, K. A. Müller, and R. S. Rubins, *Strong Axial Electron Paramagnetic Resonance Spectrum of Fe^{3+} in $SrTiO_3$ Due to Nearest-Neighbor Charge Compensation*, Phys. Rev. **135**, A86 (1964).

[43] T. Hirose and M. Kawaminami, *EPR Study of Strong Axial Cr^{3+}-Vo Centers in WO_3*, Journal of the Phys. Soc. of Japan **50**, 843 (1981).

[44] M. Capizzi and A. Frova, *Optical Gap of Strontium Titanate (Deviation from Urbach Tail Behavior)*, Phys. Rev. Lett. **25**, 1298 (1970).

[45] S. I. Shablaev, A. M. Danishevskii, V. K. Subashiev, and A. A. Babashkin, *Investigation of the energy band structure of $SrTiO_3$ by the two-photon spectroscopy method*, Sov. Phys. Solidi State **21**, 662 (1979).

[46] S. I. Shablaev, A. M. Danishevskii, and V. K. Subashiev, *The band structure of the oxygen-octahedral ferroelectrics $BaTiO_3$, $SrTiO_3$, $KTaO_3$, determined from data of two-photon spectroscopy*, Sov. Phys. JETP **59**, 1256 (1984).

[47] K. van Benthem, C. Elsässer, and R. H. French, *Bulk electronic structure of SrTiO3 : Experiment and theory*, J. Appl. Phys. **90**, 6156 (2001).

[48] C. Lee, *The Quantised Hall Effect*, Phys. Rev. Lett. **11**, 2299 (1975).

[49] D. Ricci, G. Bano, G. Pacchioni, and F. Illas, *Electronic structure of a neutral oxygen vacancy in* $SrTiO_3$, Phys. Rev. B **68**, 224105 (2003).

[50] K. A. Müller, W. Berlinger, and R. S. Rubins, *Observation of two Charged States of a Nickel-Oxygen Vacancy Pair in* $SrTiO_3$ *by Paramagnetic Resonance*, Phys. Rev. **10**, 361 (1969).

[51] P. W. Anderson, *Model for the Electronic Structure of Amorphous Semiconductors*, Phys. Rev. Lett. **34**, 953 (1975).

[52] D. J. Newman and W. Urban, *Interpretation of S-state ion E.P.R. spectra*, Adv. Phys. **24**, 793 (1975).

[53] K. A. Müller and W. Berlinger, *Superposition model for sixfold-coordinated* Cr^{3+} *in oxide crystals (EPR study)*, J. Phys. C **16**, 6861 (1983).

[54] K. A. Blazey, J. A. Cabrera, and K. A. Müller, *Oxygen vacancy-transition Metal-io impurity association in* $SrTiO_3$, Solid State Comm. **45**, 903 (1983).

[55] S. A. Basun, U. Bianchi, V. E. Bursian, A. A. Kaplyanskii, W. Kleemann, L. S. Sochava, and V. S. Vikhnin, *Study of Photoinduced charge transfer in* $SrTiO_3$*: luminescence, photoconductivity and photo-EPR*, Ferroelectrics **183**, 255 (1996).

[56] T. Feng, *Anomalous Photoelectronic Processes in* $SrTiO_3$, Phys. Rev. B **25**, 627 (1982).

[57] A. M. Glass, *Optical Spectra of Cr^{3+} Impurity Ions in Ferroelectric $LiNbO_3$ and $LiTaO_3$*, J. Chem. Phys. **50**, 1501 (1969).

[58] S. A. Basun, U. Bianchi, V. E. Bursian, A. A. Kaplyanskii, W. Kleemann, L. S. Sochava, and V. S. Vikhnin, *Charge transfer process and dynamic equilibrium of electronic state occupancies in optically excited $SrTiO_3$: Cr crystals*, J. Lumin **66**, 526 (1996).

[59] M. Grinberg, P. I. Macfarlane, B. Henderson, and K. Holliday, *Inhomogeneous broadening of optical transitions dominated by low-symmetry crystal-field components in Cr^{3+}-doped gallogermanates*, Phys. Rev. B **52**, 3917 (1995).

[60] G. A. Torchia, O. Martinez Matos, P. Vaveliuk, and J. O. Tocho, *Electron-lattice coupling in congruent Co-doped $LiNbO_3$:Cr^{3+}:ZnO crystal*, J. Phys.: Condens. Matter **13**, 6577 (2001).

[61] G. A. Torchia, O. Martinez Matos, P. Vaveliuk, and J. O. Tocho, *Influence of the electron-lattice coupling for Cr^{3+} ions in Nb^{5+} site into congruent co-doped $LiNbO_3$: Cr^{3+}: ZnO...*, Solid State Commun. **127**, 535 (2003).

[62] L. E. Orgel, *Spectra of Transition-Metal Complexes*, J. Chem. Phys. **23**, 1004 (1955).

[63] Y. Tanabe and S. Sugano, *On the Absorption Spectra of Complex Ions. I*, J. Phys. Soc. Japan. **9**, 753 (1954).

[64] Y. Tanabe and S. Sugano, *On the Absorption Spectra of Complex Ions, III The Calculation of the Crystalline Field Strength*, J. Phys. Soc. Japan. **9**, 864 (1956).

Chapter 8

Papers

Paper I

The work presented in this chapter was published in :
F. La Mattina, J. G. Bednorz, S. Alvarado, A. Shengelaya, K. A. Müller, and H. Keller, *Controlled oxygen vacancies and space correlation with Cr^{3+} in $SrTiO_3$*, Phys. Rev. B **80**, 075122 (2009)

[DOI: 10.1103/PhysRevB.80.075122]

Controlled oxygen vacancies and space correlation with Cr^{3+} in $SrTiO_3$

Abstract

By means of electron paramagnetic resonance (EPR) measurements on thermally reduced Cr-doped $SrTiO_3$, we find a strong correlation between the Cr^{3+} ions and oxygen vacancies (V_os). A charge compensation associated with the creation of V_os induced by thermal reduction causes the valence of the Cr ions to change from 4+ to 3+. This induces a symmetry change of the crystal field experienced by the Cr atom from cubic to axial. On the other hand, in Cr/Nb-codoped samples, where V_os are absent, the Cr^{3+} EPR signal is isotropic, indicating that these Cr ions occupy an octahedral site of cubic symmetry. From the angular dependence of the EPR spectra we determine an axial crystal field parameter ($D \simeq 8$ MHz), which is consistent with a perturbation induced by a V_o localized at the 3rd coordination sphere of Cr^{3+}. This is in contrast to other transition-metal dopants, where the V_o is located at the 1st coordination sphere. Thus we identify a linear complex of the form Cr^{3+}-O-Ti^{3+}-V_o-Ti^{3+}, which is unique in its structure, and which, furthermore, might account for the stabilization of the insulating state in reduced Cr-doped $SrTiO_3$ crystals.

Controlled oxygen vacancies and space correlation with Cr^{3+} in $SrTiO_3$

F. La Mattina,[1,2,3] J. G. Bednorz,[2] S. F. Alvarado,[2] A. Shengelaya,[4] K. A. Müller,[1] and H. Keller[1]
[1]*Physik-Institut der Universität Zürich, Winterthurerstr. 190, CH-8057 Zürich, Switzerland*
[2]*IBM Research, Zurich Research Laboratory, Säumerstr. 4, CH-8803 Rüschlikon, Switzerland*
[3]*EMPA, Swiss Federal Laboratories for Materials Testing and Research, Electronics/Metrology Laboratory, 8600 Dübendorf, Switzerland*
[4]*Physics Institute of Tbilisi State University, Chavchavadze 3, GE-0128 Tbilisi, Georgia*

(Received 4 June 2009; revised manuscript received 13 July 2009; published 31 August 2009)

By means of electron paramagnetic resonance (EPR) measurements on thermally reduced Cr-doped $SrTiO_3$, we find a strong correlation between the Cr^{3+} ions and oxygen vacancies (V_os). A charge compensation associated with the creation of V_os induced by thermal reduction causes the valence of the Cr ions to change from 4+ to 3+. This induces a symmetry change in the crystal field experienced by the Cr atom from cubic to axial. On the other hand, in Cr/Nb-codoped samples, where V_os are absent, the Cr^{3+} EPR signal is isotropic, indicating that these Cr ions occupy an octahedral site of cubic symmetry. From the angular dependence of the EPR spectra we determine an axial crystal field parameter ($D \simeq 8$ MHz), which is consistent with a perturbation induced by a V_o localized at the third coordination sphere of Cr^{3+}. This is in contrast to other transition-metal dopants, where the V_o is located at the first coordination sphere. Thus we identify a linear complex of the form Cr^{3+}-O-Ti^{3+}-V_o-Ti^{3+}, which is unique in its structure, and which, furthermore, might account for the stabilization of the insulating state in reduced Cr-doped $SrTiO_3$ crystals.

DOI: 10.1103/PhysRevB.80.075122 PACS number(s): 71.27.+a, 71.55.−i, 72.15.Rn, 71.30.+h

I. INTRODUCTION

The electrical transport properties of perovskite oxides can be controlled by inducing a deliberate deviation from the ideal stoichiometry.[1] The introduction of mobile charge carriers through the control of ionizable impurities is central to the production of semiconductor devices. In $SrTiO_3$ an insulator-to-metal transition is obtained at a small critical density of electron doping of $\sim 10^{18}$ e/cm^3.[2] Moreover, various cations confer substantial modifications of the electronic properties. For instance, pure reduced, and Nb-doped $SrTiO_3$ have been reported to exhibit single-gap[3,4] and two-gap superconductivity,[5] respectively. The capability of controlling point defects, such as oxygen vacancies (V_os) or transition-metal (TM) dopants, is essential for the development of semiconducting electronic devices based on perovskite compounds.[6–9] Current-induced bistable resistance effects on metal-insulator-metal (MIM) structures based on doped perovskite oxides, such as Cr-doped $SrTiO_3$, have attracted substantial interest because of their potential technological applications for nonvolatile memory devices.[10,11] Although various models have been proposed for the resistive switching in $SrTiO_3$,[12–14] a clear understanding of the role and the nature of intrinsic defects or dopants has not yet been achieved. Extended defects, such as dislocations[15] and local changes of the V_o content,[13,16–18] are proposed to be responsible for electron conduction in $SrTiO_3$. The accumulation of V_os in a confined conductive path (filamentary) has experimentally been shown[12,13] to result from a dc electroconditioning procedure.[7,9] Local reduction/oxidation processes have been proposed by some authors as an explanation for the resistance-switching mechanism,[17,19] in contradiction to other experimental evidence of trapping/detrapping processes involving the Cr dopant.[8,9] A promising concept for tailoring electronic properties on the nanometer scale arises from the possibility of creating V_os in confined regions.[17,18,20,21] The formation of V_o is accompanied by the transfer of two electrons to the $3d(z^2)$ orbitals of the two Ti atoms along the Ti-V_o-Ti axis[22] and, at higher content of V_o, an insulator-to-metal transition occurs.[23,24] Moreover, it has been proposed that the spatial distribution of the Ti^{3+}-V_o-Ti^{3+} complex[18,25,26] can induce an enhancement or a decrease in the carrier density.

In this paper, we present a detailed electron paramagnetic resonance (EPR) study of thermally reduced Cr-doped $SrTiO_3$. Based on this EPR analysis, we extract a model that describes the spatial correlation between the V_os and the Cr ions in the bulk and explains how this correlation accounts for the transport properties of $SrTiO_3$.

II. MATERIALS AND METHODS

Nominally pure $SrTiO_3$ and Cr-doped and Cr/Nb-codoped crystals were grown from stoichiometric ceramic by the floating-zone method in synthetic air (N_2/O_2).[27] The starting material was prepared by solid-state reaction of a stoichiometric mixture of $SrCO_3$ and TiO_2 at 1150 °C. The $SrCO_3$ has a purity level of 99.999%, whereas the TiO_2 has Fe and Cr at levels of 40 and 1 ppm, respectively. Cr_2O_3 or $SrCrO_4$ were admixed to $SrTiO_3$ to obtain Cr-doping levels in the range of 0.001 to 0.2 mol % or 0.4 to 2 mol %, respectively. The crystals obtained have a cylindrical shape, with a typical diameter and length of ~4 mm and ~4 cm, respectively. Two series of crystals were annealed for 6 h at 1150 °C either in O_2 or Ar/H_2 (5%). The samples were cut along the ⟨100⟩ crystallographic axis with typical dimensions of $2\times1\times0.2$ mm^3, and polished for the EPR and optical absorption (OA) measurements. EPR spectra were taken with a Bruker EMX™ system at 9.4 GHz (*X* band). A manually operated Bruker ER 218G1 goniometer was used to rotate the sample inside the EPR cavity to study the angular dependence of the EPR signal with respect to the external field.

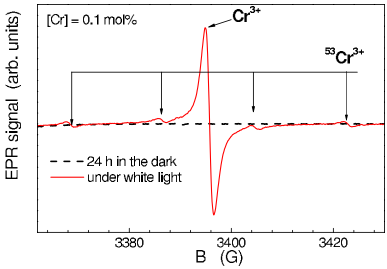

FIG. 1. (Color online) Photoinduced Cr^{3+} EPR signal in oxidized $SrTiO_3$:Cr 0.1 mol %. Solid red line: Cr^{3+} EPR signal detected under illumination with white light. The signal decays when the light is switched off, and disappears completely after 24 h (dashed black line).

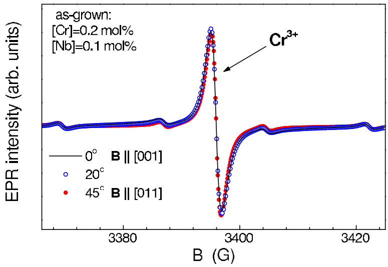

FIG. 2. (Color online) Cr^{3+} EPR signal in Cr/Nb-codoped as-grown $SrTiO_3$. The spectra are obtained by rotating the sample around the [100] crystal axis. The signals at all angles overlap, indicating a cubic site symmetry (isotropic EPR signal).

OA spectra in the near-infrared, visible, and UV range were taken at room temperature with a Beckman DU® 650 spectrometer.

III. EXPERIMENT AND RESULTS

A. Cr^{3+} site symmetry

In $SrTiO_3$, the Cr dopant substitutes Ti^{4+}, and in case of perfect oxygen stoichiometry occupies the octahedral site in the 4+ valence state. The trivalent state can be produced under illumination with a photon energy above 1.5 eV owing to a charge-transfer excitation from the valence band to the Cr 3*d* orbitals.[28] At room-temperature excitation with a photon energy above ca. 3.2 eV creates a conduction-band (CB) electron via an indirect band-gap transition,[29,30] which generates Cr^{3+} via a subsequent trapping process. In both cases, the 3+ state is unstable, and all Cr centers relax back to the 4+ valence state when the light is switched off.[28,31,32]

Cr^{4+} has spin $S=1$, and is EPR silent at the X band owing to a strong crystal-field splitting.[33] A direct detection of Cr^{4+} requires measurements at higher frequencies (Q band).[33,34] Figure 1 shows an EPR spectrum of photon generated (white light) Cr^{3+} in a stoichiometric sample and the spectrum recorded after storing the sample in the dark for 24 h. The spectrum under illumination consists of a central line ($g \approx 1.978$) resulting from the 3+ state of the ^{50}Cr, ^{52}Cr, and ^{54}Cr isotopes and a hyperfine quartet resulting from the nuclear-spin coupling ($I_n=\frac{3}{2}$) of the ^{53}Cr isotope (natural abundance 9.5%).[35]

We measured this EPR signal in a series of Cr-doped oxidized crystals, from nominally pure (0.0001 mol %) to 2 mol %, and could observe the Cr^{3+} signal only under light exposure. This suggests that in our crystals only the 4+ valence state is possible, unless an electron donor is present. However, several examples of stable Cr^{3+} have been reported in the literature.[35–38] For instance, in oxidized Cr-doped $SrTiO_3$ grown by the flame fusion method (Verneuil) a clear example has been observed by Meilerling.[37] By means of EPR he found two kinds of Cr^{3+} centers: a main EPR signal from cubic octahedral Cr^{3+} ions, and only a 4000 times weaker signal from orthorhombic Cr^{3+} centers with charge compensation involving oxygen vacancies. The difference with respect to our oxidized samples may originate from the technique used for the crystal growth. Thus, one can see that the charge state and symmetry of Cr ions in $SrTiO_3$ strongly depend on the quality of the crystal and its impurity concentrations. In our case, the floating-zone technique used for the crystal growth allows to reduce the dislocations density by up to three orders of magnitude as compared to the Verneuil method ($10^2 \sim 10^3/cm^2$ for floating-zone[39] and $\sim 10^6/cm^2$ for Verneuil).[40]

To characterize the Cr^{3+} symmetry in a stable state, we used a crystal with Cr/Nb co-doping, where Nb acts as electron donor. A Cr amount of twice the Nb content ([Cr] =0.2 mol%, [Nb]=0.1 mol%) was chosen to ensure a total compensation of the electron donors, which preserves the insulating state, a prerequisite for unambiguous EPR measurements. EPR signals recorded at different angles between the crystallographic axes and the magnetic field $\vec{\mathbf{B}}$ are shown in Fig. 2, where [100] is the rotation axis and $\theta=0$ for $\vec{\mathbf{B}} \parallel [001]$. The EPR spectra recorded at different angles overlap. This isotropy indicates that Cr^{3+} occupies a site of cubic symmetry. In the case of Cr-doped samples annealed in Ar/H_2 atmosphere, however, a perturbation of the Cr^{3+} site symmetry is apparent. This is shown in Fig. 3, which compares the EPR signal of the Cr/Nb-codoped sample with the Cr-doped reduced sample. In the latter the Cr content is lower, therefore the broadening of the EPR signal cannot be explained in terms of magnetic dipolar interaction. Thus the EPR lineshape change must originate from a site-symmetry modification (noncubic). This is explicitly demonstrated by the angular dependence of the EPR spectra for all Cr concentrations. In particular, at a doping ≤ 0.01 mol%, the narrow width ($\simeq 1.4$ G peak-to-peak) of the EPR lines allows the identification of an additional broad anisotropic line overlapping with the Cr^{3+} line. Here one can clearly separate the hyperfine line at ~ 3422 G (Fig. 4(c)) from the central line of Cr^{3+} at ~ 3400 G (Fig. 4(b)). Both lines exhibit the same changes under a rotation of the crystal by $\frac{\pi}{2}$ around the [100]

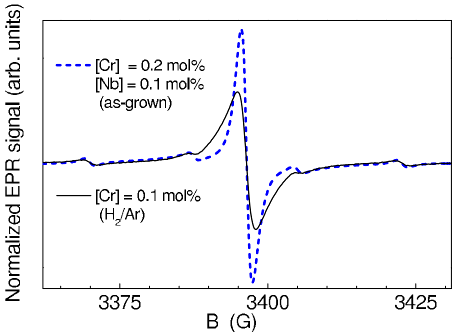

FIG. 3. (Color online) Comparison of Cr^{3+} EPR signals in $SrTiO_3$ with different site symmetries. Dashed blue line: isotropic signal detected in as-grown Cr/Nb-codoped sample; solid black line: signal detected in an oxygen-reduced Cr-doped sample. The spectra are normalized to the total number of spins (double integral of EPR signal).

axis. As the four satellite lines are a fingerprint of $^{53}Cr^{3+}$, the anisotropic component must be assigned to a Cr spin center.

B. Cr^{3+}-oxygen vacancy complex

The Cr^{3+} EPR signal observed in the crystal annealed in Ar/H_2 points to the creation of V_os as electron donors.

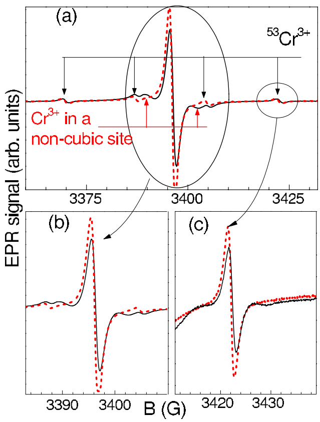

FIG. 4. (Color online) EPR spectra of oxygen-reduced Cr-doped $SrTiO_3$:Cr0.01 mol%). (a) Solid black line: B parallel to the [001] crystal axis; dashed red line: B parallel to the [011] axis. The narrow linewidth at this Cr content allows a precise comparison of the lineshape of the central line (b) of Cr^{3+} with the hyperfine line (c) of ^{53}Cr at ~3422 G ($I_n=\frac{3}{2}$). The identical changes on both lines indicate that the anisotropic component can only originate from a Cr spin center.

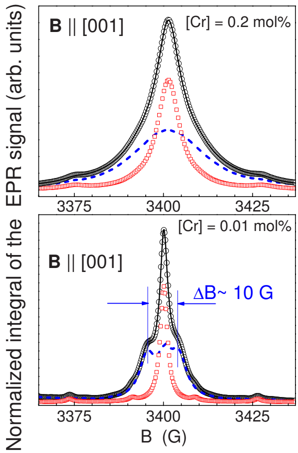

FIG. 5. (Color online) Integral of the EPR signal of reduced Cr-doped $SrTiO_3$ for two different Cr concentrations. Black circles: measured spectrum; solid black line: fitted spectrum; open red squares: the isotropic line; dashed blue line: the anisotropic component obtained as the difference between the measured data and the fitted red component.

Therefore the anisotropic component of the EPR signal should be related to a local lattice distortion due to the proximity of a V_o. A narrow isotropic and a broad anisotropic component can be clearly separated in the EPR spectra, independently of the Cr-doping level. Figure 5 shows the deconvolution performed for two different representative Cr concentrations, 0.01 and 0.2 mol %. The integrated EPR spectra were deconvoluted into a narrow and a broad component, both consisting of a central line and four hyperfine lines. All lines are well described by a Lorentzian lineshape. The shape and the position of the narrow component were found to be identical for each angle and can easily be separated from the broad anisotropic component. The dashed lines in Fig. 5 represent the anisotropic components, obtained as difference between the experimental data and the fitted isotropic components. The relative weights of the isotropic and the anisotropic contributions were found to be ~40% and ~60%, respectively. This ratio is constant for all Cr concentrations analyzed (0.001 to 2 mol %).

This fact indicates that both the charge compensation mechanism and the origin of the noncubic Cr site are identical for all samples and involve the full amount of Cr. However, for the analysis of the angular dependence of the EPR lines, the sample with the lower Cr content is not adequate because of the presence of Fe impurity, which interferes with the fitting procedure. Therefore a sample with a Cr content of 0.2 mol % was chosen. Moreover, the dimensions of the sample were chosen to be $0.5\times0.5\times0.5$ mm^3 to avoid possible contributions caused by shape anisotropies due to different mechanical stress. In Fig. 6, the angular dependence of the anisotropic component of the EPR spectra is shown. The

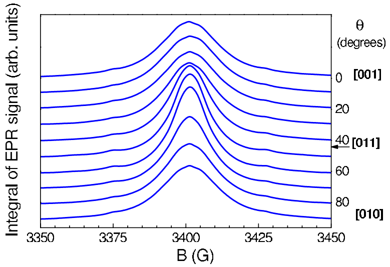

FIG. 6. (Color online) Angular dependence of the anisotropic component of the EPR signal for the Cr-doped (0.2 mol %) reduced sample. Sample rotation is around the [100] crystal axis. The [001] and the [010] axes are indistinguishable for a cubic crystal.

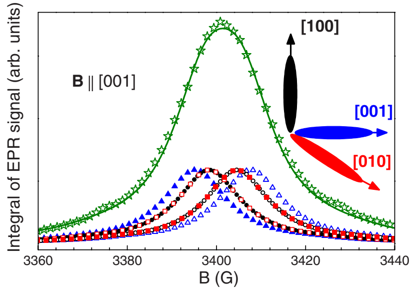

FIG. 7. (Color online) Anisotropic component of the Cr^{3+} integrated EPR signal in the reduced Cr-doped sample ([Cr] =0.2 mol%). The spectra were fitted by six Lorentzians (two for each crystal axis) using only two free parameters: the crystal-field parameter D and the linewidth w. The positions of the lines were obtained from Eqs. (3) and (4) adapted for each direction. Blue triangles, filled and open: lines relative to the [001] crystal axis; red squares, filled and open: lines relative to [010] axis; black circles, filled and open: lines of the [100] axis; green stars: the anisotropic component extracted from the experimental data; green line: sum of all fitted lines.

broad component of the spectrum reported in Fig. 5 (dashed line) indicates the presence of at least three lines within a range of 5 G from the center. This small shift suggests an analysis of the EPR spectra in terms of an effective spin Hamiltonian for Cr^{3+} in the limit of a weak crystal field. We tentatively use an axial symmetric crystal-field term in the spin Hamiltonian:[41]

$$\mathcal{H} = \beta\vec{\mathbf{B}} \cdot \vec{\mathbf{g}} \cdot \vec{\mathbf{S}} + hD\left(S_z^2 - \frac{1}{3}S \cdot (S+1)\right). \qquad (1)$$

Here β is the Bohr magneton, $\vec{\mathbf{B}}$ is the magnetic field, the $\vec{\mathbf{g}}$ tensor is assumed to be isotropic ($g \approx 1.978$), $\vec{\mathbf{S}}$ is the spin vector (S_x, S_y, S_z), h is Planck's constant, D is the crystal-field operator describing the axial symmetry (here measured in GHz), and $S=\frac{3}{2}$. The weak crystal-field condition is obtained by the limiting condition of $D \ll \sim 9.4$ GHz (the microwave energy used). Under this condition, it is possible to solve the effective Hamiltonian with a perturbation approach and obtain the following resonant magnetic fields (B_{res}) for the three allowed transitions:[42,43]

$$\left(-\frac{1}{2} \leftrightarrow +\frac{1}{2}\right): B_{res} = B_0 \qquad (2)$$

$$\left(-\frac{3}{2} \leftrightarrow -\frac{1}{2}\right): B_{res} = B_0 + \Delta B_0(3\cos\theta^2 - 1) \qquad (3)$$

$$\left(+\frac{1}{2} \leftrightarrow +\frac{3}{2}\right): B_{res} = B_0 - \Delta B_0(3\cos\theta^2 - 1). \qquad (4)$$

Here $\Delta B_0 = \frac{hD}{g\beta}$ Eq. (2) describes an isotropic line corresponding to the transition $-\frac{1}{2} \leftrightarrow +\frac{1}{2}$, and Eqs. (3) and (4) describe two anisotropic lines that are symmetrically spaced around the central line. The relative amplitudes of the three spectral contributions are 3:4:3,[41] yielding a fraction of $\frac{4}{4+6}$ (40%) for the isotropic and $\frac{6}{4+6}$ (60%) for the anisotropic contribution, in excellent agreement with our experiments. As this intensity ratio was found to be independent of the Cr doping level (as mentioned earlier), we can conclude that each Cr occupies a site of axial symmetry. Therefore, a space correlation between the Cr^{3+} and the V_o is present, and is responsible for the site symmetry. To estimate the axial crystal-field parameter D defined in Eq. (1), a fitting model for the anisotropic spectral component was implemented by using Eqs. (3) and (4). In Fig. 7, a multiple line fit is shown for $\theta=0$, where six Lorentzian lines (two each for the [001], [010], and [100] crystal axes) were used. Equations (3) and (4) describe the contribution of the [001] crystal axis, whereas the [010] contribution can be obtained by replacing θ with $\frac{\pi}{2}-\theta$. The [100] rotation axis gives rise to two constant components for $\theta=\frac{\pi}{2}$. Assuming that all lines have the same linewidth w, the spectra in Fig. 6 were analyzed using only two free param-

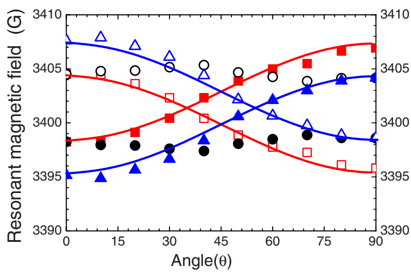

FIG. 8. (Color online) Angular dependencies of the EPR transitions of Cr^{3+} in $SrTiO_3$ in an axial crystal field. The symbols describe the peak position of the transitions shown in Fig. 7. The solid lines correspond to calculated curves based on Eqs. (3) and (4) with $D=8.3$ MHz. The transitions of Cr^{3+} are represented as: triangles, axial symmetry along [001]; squares, along [010], and circles, [100].

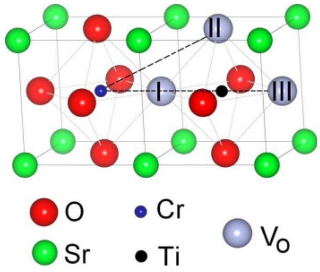

FIG. 9. (Color online) Crystal structure of Cr-doped $SrTiO_3$, showing the possible V_o position in the first three coordination spheres I, II, and III.

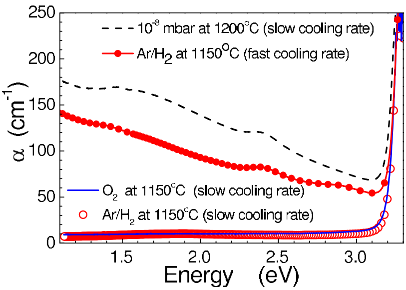

FIG. 10. (Color online) Optical absorption spectra of nominally pure $SrTiO_3$ annealed in different atmospheres.

eters, D and w. The analysis was performed for each spectrum in Fig. 6, yielding an average value $\bar{D}=8.3(8)$ MHz, corresponding to $\Delta\bar{B}_0=3.0(3)$ G. Figure 8 shows the peak position of the six lines as function of θ, and the continuous line is obtained by using $\bar{D}$.

At much lower Cr content, the value of D can be estimated directly from the spectra. In Fig. 5, three peaks are clearly distinguishable in the anisotropic component (dashed line). The maximum peak-to-peak distance corresponds to $4\Delta B_0$ in our fitting model, from which we estimate $D \simeq 7$ MHz ($\Delta B_0 \simeq 2.5$ G). This value is much smaller than the one found in Cr-doped WO_3,[44] where a V_o located next to the Cr site produces a much stronger axial field, $D \simeq 85$ GHz. Owing to the strong valence-bond character of the oxygen octahedron, a similar crystal-field splitting should be observed in $SrTiO_3$ for of a V_o directly attached to the Cr site (position I in Fig. 9). This discrepancy suggests that the V_o is located at the third coordination sphere along the $\langle 100 \rangle$ directions (position III in Fig. 9). A V_o in the second coordination sphere (position II in Fig. 9) is excluded because this geometry leads to a symmetry that is inconsistent with our result of an axial symmetry along $\langle 100 \rangle$.

C. Electron localization: Suppression of the conducting state

OA spectra taken at room temperature enable a comparison between conducting and insulating $SrTiO_3$ (Refs. 1 and 10) (Fig. 10). The undoped oxidized sample is insulating and transparent in the near-infrared and visible range with an absorption edge at 3.2 eV, corresponding to the an indirect band-gap transition of $SrTiO_3$.[30,45,46] The highly reduced sample, annealed in vacuum, exhibits absorption below the band gap, which can be assigned to the presence of V_os and conducting electrons.[1,47] However, the nominal pure $SrTiO_3$ crystals annealed in Ar/H_2 or O_2 (ambient pressure, at 1150 °C for 6 h), show identical OA spectra. These two particular thermal treatments were performed with a relatively slow cooling rate ($\simeq -200$ °C/h) from 1150 °C to room temperature. The comparison of the spectra in Fig. 10 suggest that the Ar/H_2 annealing is not able to significantly change the conducting properties of pure $SrTiO_3$. However, if the sample is quenched (in ≤ 60 sec) from 1150 °C to room temperature, the crystal became conducting and exhibits a similar OA spectrum as the pure $SrTiO_3$ annealed in high vacuum, as shown in Fig. 10. This means that at 1150 °C a significant amount of V_o is introduced because of the reducing atmosphere of Ar/H_2, but the cooling process can produce different effects: the slow cooling rate ($\simeq -200$ °C/h) assists the reoxidation of the crystal due to presence of a residual partial pressure of O_2; the fast cooling (quenching) freezes V_o in the crystal. A different behavior was observed in the case of Cr-doped crystals. The Ar/H_2 annealing causes the valence change in Cr from the 4+ to the 3+ state. Since Cr^{4+} ions are deep traps for CB electrons, at high temperature they capture electrons introduced by the V_o, and when the temperature is reduced slowly, the crystal is forced to keep an amount of V_o to compensate the charge trapped at the Cr^{3+} ions. In the doping range investigated, i.e., up to 2 mol %, all Cr atoms convert to the 3+ valence state, as demonstrated by the linear dependence of the EPR intensities of Cr^{3+} versus the Cr concentration shown in Fig. 11. At a content ≤ 0.01 mol%, the average distance between the Cr centers is ≥ 10 unit cells. Therefore, at this distance, an interaction between the Cr sites is expected to be negligible. As at all concentrations the Cr^{3+} centers exhibit the

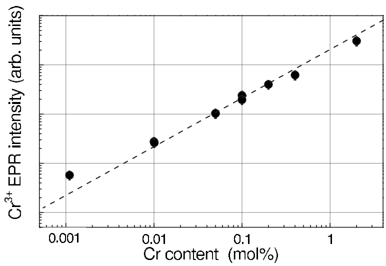

FIG. 11. Intensity of the EPR Cr^{3+} signal versus Cr content in reduced $SrTiO_3$. The linear dependence and the absence saturation at high doping show that all Cr ions are converted to the 3+ valence state.

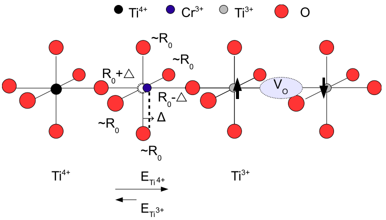

FIG. 12. (Color online) Model of the Cr^{3+}-O-Ti^{3+}-V_o-Ti^{3+} complex in reduced Cr-doped $SrTiO_3$ with the Cr^{3+} ion displaced by the distance Δ from the original 4+ position. The electric field generated by the two adjacent Ti^{3+} and Ti^{4+}, maybe responsible of the displacement Δ.

same axial symmetry, there must be a V_o perturbing each of the Cr sites. The absence of a saturation in the linear behavior suggests that the compensation arises from the effect of the thermal annealing on the Cr dopants and not from other impurities. Moreover, the linear behavior indicates that the charge compensation mechanism is the same at every doping level.

In the following, we discuss the possible mechanisms that change the valence of the Cr ions to the 3+ state and the origin of the Cr^{3+} axial symmetry. The electron captured by the Cr ion could come from the same V_o located at the third coordination sphere of the ion. In this case an unpaired electron should remain at the V_o center or a Ti^{4+} should be converted to Ti^{3+}. In both cases the magnetic dipolar interaction of these centers with the Cr^{3+} ion could give rise to an axial symmetry. According to Fig. 9, this electron should have an average distance from the Cr^{3+} ion on the order of $R_D=3\times R_0$, where R_0 is the distance between the Cr ion and the oxygen atom at the first coordination sphere. The magnitude of the field produced by this unpaired electron at the Cr^{3+} site is given by the expression[41]

$$B \simeq \frac{g\beta}{R_D^3} \simeq 93 \text{ G}. \tag{5}$$

This value is one order of magnitude larger than our experimental value observed as the splitting $\Delta B_0 \sim 3$ G. This discrepancy is consistent with the fact that we did not observe any other paramagnetic center except that of the Cr^{3+}. We have to conclude that, if an unpaired electron is present at the V_o site (or in form of Ti^{3+}) there must be a strong phonon coupling which masks this paramagnetic center via a strong spin-phonon relaxation. Another possible explanation is that there are two kinds of V_o centers introduced by the Ar/H_2 annealing: double charged vacancies (V_o^{++}) which could be randomly distributed and compensate the charges of the electrons trapped by the Cr ions and neutral V_os which are located at the third coordination sphere of the Cr^{3+} ions. In the case of the neutral V_o center, the two electrons from the missing bond of the nearest Ti ions are localized at the two adjacent Ti^{3+} with antiparallel spins[22] as shown in Fig. 12. This particular spin configuration is EPR silent.[48] Both kinds of oxygen vacancies are consistent with the model of strongly localized two-electron and two-hole excitation proposed by Anderson.[49]

The proximity of the Ti^{3+}-V_o-Ti^{3+} complex may be responsible of the breaking of the symmetry of the crystal field experienced by the Cr ion. As shown in Fig. 12, the Ti^{4+} repels the Cr^{3+} more than the nearest Ti^{3+}. The result of this Coulomb interaction produces a net attractive force on the Cr^{3+} toward the Ti^{3+}-V_o-Ti^{3+} complex. As a consequence, the Cr ion may result displaced from the center of the octahedron. Because of the strong covalent bond of the oxygen octahedron, we assume the displacement of the Cr ions as predominant reason of the axial symmetry. We now estimate the displacement of the Cr ion using the experimental value of the axial parameter D. For spin centers $S<2$, Newman and Urban[50] have shown that D can be expressed as a simple sum over the contribution of the separate coordinated ligands (denoted n):

$$D = \bar{b}_2(R_0)\left(\frac{3}{2}\right)\sum_1^6 \left(\frac{R_0}{R_n}\right)^{t_2}\left(\cos^2 \Theta_n - \frac{1}{3}\right). \tag{6}$$

Here R_0 is distance between the Cr ion and the oxygen in an unperturbed octahedral site (Fig. 12), R_n is the distance between the Cr ion and the nth oxygen ligand in the distorted site, Θ_n is the angle between the line joining the paramagnetic ion with the nth ligand and main EPR axis, and $\bar{b}_2(R_0)$ and t_2 are coefficients that depend on R_0 and the nature of the ligand. These two coefficients have been evaluated by Müllër and Berlinger[36] for Cr^{3+} on a metal 4+ site in $SrTiO_3$. In particular they replace the term $\bar{b}_2(R_0)\times(\frac{R_0}{R})^{t_2}$ in Eq. (6) with the function $\bar{b}_2(R)$, which can be approximated to a Lennard-Jones-type function described as:[36]

$$\bar{b}_2(R) = -A\left(\frac{R_0}{R}\right)^n + B\left(\frac{R_0}{R}\right)^m, \tag{7}$$

where $R_0=1.95$ Å, $A=-9.7(1.3)$ cm^{-1}, $B=-7.4(1.2)$ cm^{-1}, and the two exponents $m=10$ and $n=13$. From Eqs. (6) and (7) and the experimental D value, we calculated the displacement Δ (Fig. 12) of the Cr^{3+} as

$$D = \bar{b}_2(R_0+\Delta) + \bar{b}_2(R_0-\Delta) - 2\bar{b}_2(R_0). \tag{8}$$

We obtain $\Delta=0.06(2)$ Å, which corresponds to a displacement of only 3%. This result is in excellent agreement with a previous study of the EPR signal of Cr^{3+} in $SrTiO_3$ under a static uniaxial stress reported by Müller and Berlinger.[36] They found a value of $\Delta B_0 \simeq 2.8$ G, extrapolated at zero stress, which compares with our results of $\simeq 3$ G. They suggest that this axial symmetry may be explained in terms of a displacement of the Cr ion out of the center of the octahedral site along one of the $\langle 100 \rangle$ directions. Here we demonstrate that the axial symmetry is not an intrinsic property of the Cr^{3+}, but is a consequence of the nature of the charge compensation which generates the Cr^{3+} sites caused by the V_os. In the Cr/Nb-codoped crystal, with only Nb as a donor the Cr^{3+} remains in the center of a cubic site, whereas in the case of V_o compensation it shifts from the center. Other complexes of TM ions and V_os where the oxygen vacancy is located in the first coordination sphere have been found in $SrTiO_3$, for example Fe^{3+}-V_o,[51] Mn^{2+}-V_o,[52] and Ni^{3+}-V_o.[48] However, the Cr^{3+}-V_o complex has never been observed with the V_o at the first coordination sphere. This fact may be explained in terms of the interaction between the Cr ion and the V_o. Once the Cr^{4+} traps an electron and becomes Cr^{3+}, the Coulomb interaction with the Ti^{3+} minimizes the energy to form the structure presented in Fig. 12. This particular complex could be the reason why all the reduced Cr-doped $SrTiO_3$ crystals we studied were insulating.

IV. CONCLUSIONS

Our EPR study of Cr-doped $SrTiO_3$ single crystals reveals changes in the symmetry of the Cr site that we control by means of thermal annealing and/or doping with electron donors. When electron donors are present, a Cr atom can change its valence from 4+ to 3+. If the Cr content is equal to or higher than that of the electron donors, the insulating state will be preserved. In a Cr/Nb-codoped crystal, we found that Cr^{3+} occupies an undistorted octahedral site, whereas in the Cr-doped reduced crystals there is a symmetry change from cubic to axial of the crystal field felt by the Cr atom. Here the full amount of Cr is converted to the 3+ state via a charge compensation involving V_os. For the Cr^{3+} in this complex, we found an axial crystal-field parameter $\bar{D}=8.3(8)$ MHz. Here we demonstrate that the axial symmetry observed at the Cr^{3+} site originates from the special location of a V_o which breaks the octahedral symmetry. The corresponding value of D is much lower than that of $\sim$42 GHz for Fe-V_o in $SrTiO_3$,[52] and $\sim$85 GHz for Cr-V_o in WO_3.[44] In these cases the axial symmetry has been assigned to V_os located in the first coordination sphere of the Fe or Cr sites. Our results on reduced crystals indicate, however, that the V_os in Cr-doped $SrTiO_3$ are located at the third coordination sphere. The charge neutrality of the sample and the axial symmetry of the Cr^{3+} can be explained with the presence of two kinds of oxygen vacancies: the neutral V_os and the double charged V_o^{++}s. The amount of both kinds of vacancies is directly controlled by the Cr concentration, and this correlation accounts for the preservation of the insulating state of the reduced Cr-doped crystals.

ACKNOWLEDGMENTS

We thank F. Waldner for providing his expertise for the EPR data analysis and for a careful reading of the manuscript. We thank Y. Watanabe and A. Maisuradze for fruitful discussions and valuable suggestions. F.L.M. gratefully acknowledges support by the Swiss National Science Foundation and the IBM Zurich Research Laboratory. We also thank D. Widmer, H. P. Ott, and K. Wasser for competent technical assistance.

[1] W. S. Baer, Phys. Rev. **144**, 734 (1966).
[2] O. N. Tufte and P. W. Chapman, Phys. Rev. **155**, 796 (1967).
[3] J. F. Schooley, W. R. Hosler, and M. L. Cohen, Phys. Rev. Lett. **12**, 474 (1964).
[4] C. S. Koonce, M. L. Cohen, J. F. Schooley, W. R. Hosler, and E. R. Pfeiffer, Phys. Rev. **163**, 380 (1967).
[5] G. Binnig, A. Baratoff, H. E. Hoenig, and J. G. Bednorz, Phys. Rev. Lett. **45**, 1352 (1980).
[6] C. H. Ahn, J. M. Triscone, and J. Mannhart, Nature (London) **424**, 1015 (2003).
[7] Y. Watanabe, Ferroelectrics **349**, 190 (2007).
[8] S. F. Alvarado, F. La Mattina, and J. G. Bednorz, Appl. Phys. A: Mater. Sci. Process. **89**, 85 (2007).
[9] F. La Mattina, J. G. Bednorz, S. F. Alvarado, A. Shengelaya, and H. Keller, Appl. Phys. Lett. **93**, 022102 (2008).
[10] A. Beck, J. G. Bednorz, C. Gerber, C. Rossel, and D. Widmer, Appl. Phys. Lett. **77**, 139 (2000).
[11] Y. Watanabe, J. G. Bednorz, A. Bietsch, C. Gerber, D. Widmer, A. Beck, and S. J. Wind, Appl. Phys. Lett. **78**, 3738 (2001).
[12] C. Rossel, G. I. Meijer, D. Bremaud, and D. Widmer, J. Appl. Phys. **90**, 2892 (2001).
[13] M. Janousch, G. I. Meijer, U. Staub, B. Delley, S. F. Karg, and B. P. Andreasson, Adv. Mater. **19**, 2232 (2007).
[14] M. J. Rozenberg, I. H. Inoue, and M. J. Sánchez, Phys. Rev. Lett. **92**, 178302 (2004).
[15] K. Szot, W. Speier, R. Carius, U. Zastrow, and W. Beyer, Phys. Rev. Lett. **88**, 075508 (2002).
[16] S. Karg, G. I. Meijer, D. Widmer, and J. G. Bednorz, Appl. Phys. Lett. **89**, 072106 (2006).
[17] K. Szot, W. Speier, G. Bihlmeyer, and R. Waser, Nat. Mater. **5**, 312 (2006).
[18] D. A. Müller, N. Nakagawa, A. Ohtomo, J. L. Grazul, and H. Y. Hwang, Nature (London) **430**, 657 (2004).
[19] D. Choi, D. Lee, H. Sim, M. Chang, and H. Hwang, Appl. Phys. Lett. **88**, 082904 (2006).
[20] Y. Watanabe, D. Sawamura, and M. Okano, Appl. Phys. Lett. **72**, 2415 (1998).
[21] L. Pellegrino, I. Pallecchi, D. Marre, E. Bellingeri, and A. S. Siri, Appl. Phys. Lett. **81**, 3849 (2002).
[22] D. Ricci, G. Bano, G. Pacchioni, and F. Illas, Phys. Rev. B **68**, 224105 (2003).
[23] N. Shanthi and D. D. Sarma, Phys. Rev. B **57**, 2153 (1998).
[24] J. Carrasco, F. Illas, N. Lopez, E. A. Kotomin, Y. F. Zhukovskii, R. A. Evarestov, Y. A. Mastrikov, S. Piskunov, and J. Maier, Phys. Rev. B **73**, 064106 (2006).
[25] D. D. Cuong, B. Lee, K. M. Choi, H.-S. Ahn, S. Han, and J. Lee, Phys. Rev. Lett. **98**, 115503 (2007).
[26] F. Cordero, Phys. Rev. B **76**, 172106 (2007).
[27] G. I. Meijer, U. Staub, M. Janousch, S. L. Johnson, B. Delley, and T. Neisius, Phys. Rev. B **72**, 155102 (2005).
[28] S. A. Basun, U. Bianchi, V. E. Bursian, A. A. Kaplyanskii, W. Kleemann, L. S. Sochava, and V. S. Vikhnin, Ferroelectrics **183**, 255 (1996).
[29] M. Capizzi and A. Frova, Phys. Rev. Lett. **25**, 1298 (1970).
[30] K. van Benthem, C. Elsässer, and R. H. French, J. Appl. Phys. **90**, 6156 (2001).

[31] S. A. Basun, U. Bianchi, V. E. Bursian, A. A. Kaplyanskii, W. Kleemann, L. S. Sochava, and V. S. Vikhnin, J. Lumin. **66-67**, 526 (1995).
[32] T. Feng, Phys. Rev. B **25**, 627 (1982).
[33] R. H. Hoskins and B. H. Soffer, Phys. Rev. **133**, A490 (1964).
[34] D. E. Budil, D. G. Park, J. M. Burlitch, R. F. Geray, R. Dieckmann, and J. Freed, J. Chem. Phys. **101**, 3538 (1994).
[35] K. A. Müller, Arch. Sci. **11**, 150 (1958).
[36] K. A. Müller and W. Berlinger, J. Phys. C **16**, 6861 (1983).
[37] H. D. Meierling, Phys. Status Solidi B **43**, 191 (1971).
[38] S. E. Stokowski and A. L. Schawlow, Phys. Rev. **178**, 457 (1969).
[39] J. J. Kawanabe, H. Minami, K. Oka, R. Oishim, and H. Uwe, Ferroelectrics **348**, 89 (2007).
[40] J. G. Bednorz and H. J. Scheel, J. Cryst. Growth **41**, 5 (1977).
[41] J. E. Wertz, *Electron Spin Resonance, Elementary Theory and Practical Applications* (Chapman and Hall, London, 1986).
[42] B. Bleaney, Physica **17**, 175 (1951).
[43] B. Bleaney and D. J. E. Ingram, Proc. R. Soc. London, Ser. A **205**, 336 (1951).
[44] T. Hirose and M. Kawaminami, J. Phys. Soc. Jpn. **50**, 843 (1981).
[45] S. I. Shablaev, A. M. Danishevskii, V. K. Subashiev, and A. A. Babashkin, Sov. Phys. Solid State **21**, 662 (1979).
[46] S. I. Shablaev, A. M. Danishevskii, and V. K. Subashiev, Sov. Phys. JETP **59**, 1256 (1984).
[47] C. Lee, J. Destry, and J. L. Brebner, Phys. Rev. B **11**, 2299 (1975).
[48] K. A. Müller, W. Berlinger, and R. S. Rubins, Phys. Rev. **186**, 361 (1969).
[49] P. W. Anderson, Phys. Rev. Lett. **34**, 953 (1975).
[50] D. J. Newman and W. Urban, Adv. Phys. **24**, 793 (1975).
[51] K. A. Blazey, J. A. Cabrera, and K. A. Müller, Solid State Commun. **45**, 903 (1983).
[52] E. S. Kirkpatrick, K. A. Müller, and R. S. Rubins, Phys. Rev. **135**, A86 (1964).

Paper II

The work presented in this chapter was published in :
F. La Mattina, J. G. Bednorz, S. Alvarado, A. Shengelaya, H. Keller, *Detection of charge transfer processes in Cr-doped $SrTiO_3$ single crystal*, Appl. Phys. Lett. **93**, 022102 (2008)
 [DOI: 10.1063/1.2959059]

Detection of charge transfer processes in Cr-doped $SrTiO_3$ single crystal

Abstract

An insulator-to-metal transition is observed in Cr-doped $SrTiO_3$ single crystals upon extended exposure to a high electric field, namely, electro conditioning (EC). Electron paramagnetic resonance (EPR) and transport measurements under laser irradiation show anticorrelation between the Cr^{3+} EPR signal and the electrical current. This proves that the Cr3+ ions are responsible for the photocurrent that initiates the EC process. We observe the presence of Cr^{3+}/Cr^{4+} mixed valencies in the bulk in the conducting state. The EPR characterization of the spectra in the conducting state excludes the possibility of a Cr^{3+}-oxygen vacancy complex in the bulk as a result of the EC.

APPLIED PHYSICS LETTERS **93**, 022102 (2008)

Detection of charge transfer processes in Cr-doped $SrTiO_3$ single crystals

F. La Mattina,[1,2,a)] J. G. Bednorz,[2] S. F. Alvarado,[2] A. Shengelaya,[3] and H. Keller[1]
[1]*Physik-Institut der Universität Zürich, Winterthurerstr. 190, CH-8057 Zürich, Switzerland*
[2]*IBM Research, Zurich Research Laboratory, Säumerstr. 4, CH-8803 Rüschlikon, Switzerland*
[3]*Physics Institute of Tbilisi State University, Chavchavadze 3, GE-0128, Tbilisi, Georgia*

(Received 20 May 2008; accepted 24 June 2008; published online 15 July 2008)

An insulator-to-metal transition is observed in Cr-doped $SrTiO_3$ single crystals upon extended exposure to a high electric field, namely, electroconditioning (EC). Electron paramagnetic resonance (EPR) and transport measurements under laser irradiation show anticorrelation between the Cr^{3+} EPR signal and the electrical current. This proves that the Cr^{3+} ions are responsible for the photocurrent that initiates the EC process. We observe the presence of Cr^{3+}/Cr^{4+} mixed valencies in the bulk in the conducting state. The EPR characterization of the spectra in the conducting state excludes the possibility of a Cr^{3+}-oxygen vacancy complex in the bulk as a result of the EC. © *2008 American Institute of Physics*. [DOI: 10.1063/1.2959059]

Insulator-to-metal transitions with a resistive memory effect in selected perovskites are under intense investigation because of potential applications for information storage devices (Ref. 1, and references therein). The investigation of insulating Cr-doped $SrTiO_3$ (band gap$=3.2$ eV) as model system shows that during exposure to an electric field[1–3] its resistance is reduced by several orders of magnitude and a conductive state is reached. We define this process as electroconditioning (EC). In the conducting state, current pulses of opposite polarity switch the resistance reversibly between a high and a low level.[2,4,5] So far, it is not clear whether the fundamental switching mechanism is an interface effect, a bulk effect, or a combination of both. Understanding the mechanism of the EC process is crucial for the development of a model describing the behavior of such a system.

In our study we investigate the influence of the Cr dopant during the EC process. We discuss results obtained on crystals with a doping concentration of 0.1 and 0.2 mol %, grown by the floating-zone method, and annealed for 6 h at 1150 °C in $Ar/H_2(5\%)$. Capacitor-like structures of dimensions $2.5\times1\times0.2$ mm^3 were prepared by depositing Pt electrodes of 50–100 nm thickness on the (100) large faces of polished crystals via e-beam evaporation. The electrodes consist of 0.1×2 mm^2 stripes with a gap of 0.15 mm, interconnected by drops of silver paint to form a meandering structure. These structures are an approximation of a continuous metallic layer, but are transparent to microwave radiation. Electron paramagnetic resonance (EPR) spectra at 9.4 GHz were collected with a Bruker EMX™ spectrometer, and a 2,2-diphenyl-1-picrylhydrazyl sample was used both as standard for the intensity and as a reference resonance marker. A 633 nm ($\sim$1.9 eV) laser of 10 mW was used to illuminate the sample in combination with an optical shutter. Luminescence was detected by means of an avalanche photodiode collecting photons in the range of 400–1100 nm.

We started the EC process with crystals that were insulating despite of having been annealed in reducing atmosphere. It is known that in $SrTiO_3$ oxygen vacancies (V_O) introduced by a reduction process create a conducting state.[6] However, in our case, because of the presence of the Cr dopants, the insulating state is preserved via a charge compensation by transforming the initial Cr^{4+} to Cr^{3+} (Ref. 2). The Cr^{3+} ions act as a reservoir of electrons which can be promoted selectively to the conduction band (CB) by photoexcitation above $\sim$1.86 eV.[7] This process can be directly observed in the time dependence of the photocurrent and the EPR signal of Cr^{3+} under laser irradiation. This is shown in Fig. 1 for a virgin crystal with 0.1 mol % of Cr at fixed bias voltage of 50 V. The photocurrent under laser illumination is accompanied by a decrease in the Cr^{3+} signal. After stopping the irradiation, the CB electrons recombine at the Cr centers, as evidenced by the recovery of the EPR signal. Simultaneously, the current drops rapidly to the initial value. This anticorrelation is a direct proof of selective transfer of electrons between the Cr ions and the CB. Further evidence of this recombination process is provided by the delayed luminescence (DL) which accompanies the EPR signal recovery (Fig. 1). This emission arises when a CB electron is trapped by Cr^{4+}, forming Cr^{3+} in an excited state ($^2E_{2g}$), which subsequently relaxes radiatively via the $^2E_{2g}\rightarrow{}^4A_{2g}$ transition (*R* line, see Fig. 2).[2,7,8] A part of the electrons are fast in recombining and the rest need a longer time to diffuse until

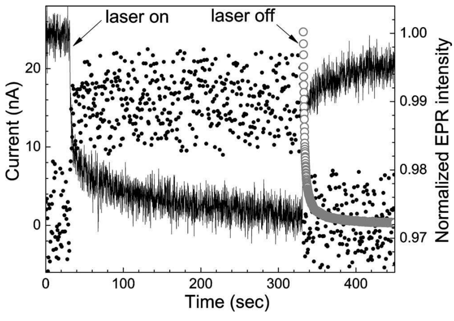

FIG. 1. Photocurrent (dots) and EPR intensity of Cr^{3+} (continuous line) in Cr-doped $SrTiO_3$ ([Cr]=0.1 mol %) as a function of time for a bias voltage of 50 V and laser irradiation ($\lambda=633$ nm). When the laser is turned off, the DL arising from the *R* line of Cr^{3+} is recorded (gray open circles). The EPR data are not corrected for a slow linear drift.

a)Electronic mail: fabiolm@physik.uzh.ch.

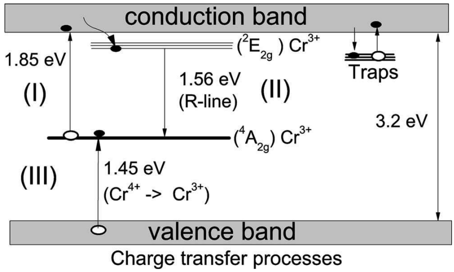

FIG. 2. Diagram of energy transitions and charge transfer processes involving the Cr^{3+} ions in $SrTiO_3$. Adapted from Basun *et al.* (Ref. 7).

they recombine at Cr sites. The recovery of the EPR signal exhibits two components: the fast one correlated with the current drop and the slow one also visible in the DL measurements. The EPR signal indicates that roughly half of the electrons recombine promptly, whereas the remainder recombines with a very long decay time. The slow recombination kinetics was proposed by Basun *et al.*[7] to originate from the capture of electrons at trap centers below the CB, which are not related to the Cr, and by their release, which can be activated thermally and/or by IR irradiation (<1 eV).[7] Figure 2 shows an additional charge transfer process (III) from the valence band (VB) to Cr^{4+}, resulting in the increase of the Cr^{3+} concentration and creation of holes in the VB. As in the virgin sample all Cr ions are in the 3+ state at the beginning of the irradiation, process III is negligible. However, the creation of Cr^{4+} via process I will be balanced via processes II and III as shown by the asymptotic approach to a steady state in the EPR signal (see Fig. 1). The rate of recombination of process II is controlled by the diffusion of electrons from the traps. The time to reach 90% of both EPR signal decay and recovery is comparable and on the order of 80 s. At high initial resistance (~30 GΩ), process I provides the carriers necessary to initiate the EC, which typically requires fields higher than 10^4 V/cm. For prolonged application of such a bias under continuous photoexcitation, the current will increase, and the voltage is adjusted to minimize the power load and prevent damage. Figure 3 shows the effect of illumination when a crystal with 0.2 mol % of Cr content has

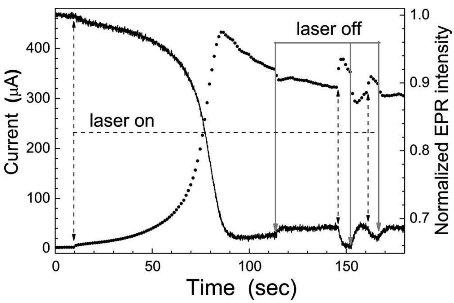

FIG. 3. Photocurrent (dots) and EPR intensity of Cr^{3+} (continuous line) in Cr-doped $SrTiO_3$ ([Cr]=0.1 mol %) as a function of time for a bias voltage of 200 V and laser irradiation (λ=633 nm).

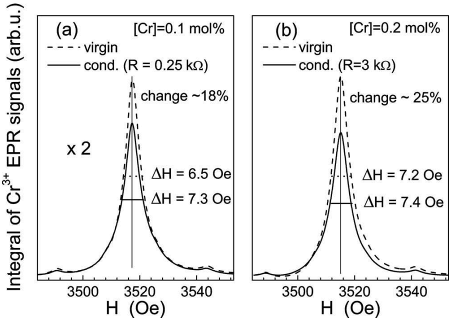

FIG. 4. Integral of the EPR Cr^{3+} signal in Cr-doped $SrTiO_3$ vs. magnetic field *H*. Comparison between the virgin (dashed line) and conducting crystals (continuous line).

reached a higher (intermediate) conducting state (1 M Ω) after ~2 h. At 200 V under laser illumination, the current increases and, simultaneously, the EPR intensity of Cr^{3+} decreases. Here we observe a decrease by ~30% of the initial EPR signal, whereas in the virgin state (see Fig. 1) the observed decrease is typically between 3% and 5%. Hence the transfer of electrons from the Cr ions to the CB can now be more effectively stimulated through impact ionization by the electrical current itself. The overshoot of the electrical current at ~90 s is not correlated with the EPR changes, indicating that at this stage, also other phenomena and/or other sources of carriers are involved. The photoexcited electrons involving the Cr centers are getting less dominant as revealed in subsequent on-off illumination cycles. The drastic resistance decrease by three orders of magnitude (gigaohm → megaohm) can only be due to a substantial transformation of the bulk properties. Once the final conducting state is reached, the intensity of the Cr^{3+} signal has irreversibly dropped to a lower level. Figure 4 shows the integral of the Cr^{3+} EPR spectra of samples in the insulating and the conducting state for doping levels of 0.1 and 0.2 mol %, in which the EC process leads to final resistances of 0.25 and 3 kΩ, respectively. It can be seen that the total amount of Cr^{3+} is lowered by ~20%. This change can be regarded as a measure of the volume fraction of the crystal that is irreversibly modified. The comparison between the virgin and conducting samples shows an increase of the full width at half maximum (FWHM) of $\Delta H \sim 1$ Oe in the sample with 0.1 mol % of Cr. For the sample with higher doping level (Fig. 4(b)), the FWHM remains apparently unchanged, because the linewidth is already broadened owing to the higher Cr content. The lineshape, however, is clearly asymmetric after the EC, indicating a small distortion of the Cr environment. In addition, there is evidence of electronic structural changes, as indicated by the reaction of the crystals to the laser illumination (without bias voltage) in the conducting state. Figure 5 shows that in this case the Cr^{3+} signal increases under laser exposure, whereas in the virgin state it decreased ([Cr]=0.1 mol %, same crystal as in Fig. 1). Process III (Fig. 2) explains this increase as a conversion of Cr^{4+} to Cr^{3+}. Therefore, the ~20% reduction in the Cr^{3+} signal in the conducting state is a proof of the creation of Cr^{4+} centers during the EC process. Apparently, the presence of mixed

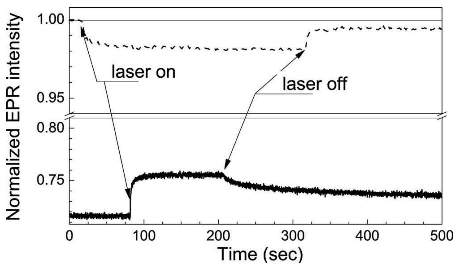

FIG. 5. Time-resolved EPR intensity of Cr^{3+} in Cr-doped $SrTiO_3$ ([Cr] =0.1 mol %) under laser exposure and without bias voltage for a sample in the virgin (dashed line) and the conducting (continuous line) state.

valencies of the Cr ions is necessary to create the conducting state. In oxidized samples, all Cr ions are in the 4+ valence state and no electron donors are present. Moreover, the Cr^{4+} ions act as electron traps, which explains why these samples cannot be brought into the conducting state through EC. An x-ray absorption spectroscopy (XAS) study of the Cr *K* edge (with a probing depth of $\sim 5\ \mu m$) shows[9] that for planar structures the EC process creates a Cr^{3+}/Cr^{4+} mixture.[3] From high-resolution imaging at the energy of the pre-edge of Cr, it is concluded that the conducting path exhibits an enrichment of V_O's located in the nearest-neighbor site of the Cr centers.[9] Such a defect should result in a paramagnetic center in a strong axial crystal field, which has been characterized for Fe^{3+}-V_O in $SrTiO_3$ and Cr^{3+}-V_O in WO_3.[10,11] In these cases, the strong axial field manifests itself in a large shift of the resonance field of the EPR signal by ~ 2000 and ~ 1000 Oe (when rotating the crystal axis from [100] to [010]) for $SrTiO_3$ and WO_3, respectively.[10,11] In our sample, however, this shift is absent, and only a small distortion was observed as deduced from the broadening by 1 Oe and the asymmetric EPR spectrum in Figs. 4(a) and 4(b), respectively. Such a small distortion of the oxygen octahedra surrounding the Cr is not compatible with the presence of V_O's at the nearest-neighbor position of Cr sites. Because EPR is a bulk-sensitive technique we cannot exclude the formation of a Cr^{3+}-V_O complex at the electrode interface as detected by XAS.

Through EPR studies we can directly observe the excitation of electrons from the Cr^{3+} ions to the CB via a decrease of the Cr^{3+} signal and a simultaneous increase of the electrical current at fixed bias. Therefore the Cr^{3+} ions present in the virgin insulating samples are responsible for the photocurrent observed that initiates the EC process. The drastic resistance decrease between the virgin and the final conducting state (gigaohm → kilo-ohm) can only be due to a substantial transformation of the bulk properties. Moreover, the decrease of the EPR signal by $\sim 20\%$ in the conducting state indicates creation of Cr^{4+}, which could act as trap centers for the carriers. Apparently, the presence of mixed valences of the Cr ions is necessary to create the conducting state. This is in agreement with the result of luminescence measurements showing the recombination of electrons from the CB to the Cr^{4+} ions during the switching of conductivity to the high-resistance memory state.[2] The small distortions of the EPR spectra in the conducting state exclude the possibility of a Cr^{3+}-V_O complex in the bulk as a result of the EC that was proposed by others authors.[5,9]

We thank K. A. Müller, Y. Watanabe, and A. Maisuradze for fruitful discussions. F.L.M. gratefully acknowledges support by the Swiss National Science Foundation. We also thank M. Tschudy, D. Widmer, H. P. Ott, K. Wasser, and K. Bösiger for competent technical assistance.

[1] Y. Watanabe, Ferroelectrics **349**, 190 (2007).
[2] S. F. Alvarado, F. L. Mattina, and J. G. Bednorz, Appl. Phys. A: Mater. Sci. Process. **89**, 85 (2007).
[3] G. I. Meijer, U. Staub, M. Janousch, S. L. Johnson, B. Delley, and T. Neisius, Phys. Rev. B **72**, 155102 (2005).
[4] A. Beck, J. G. Bednorz, C. Gerber, C. Rossel, and D. Widmer, Appl. Phys. Lett. **77**, 139 (2000).
[5] K. Szot, W. Speier, G. Bihlmeyer, and R. Waser, Nat. Mater. **5**, 312 (2006).
[6] W. S. Baer, Phys. Rev. **144**, 734 (1966).
[7] S. A. Basun, U. Bianchi, V. E. Bursian, A. A. Kaplyanskii, W. Kleemann, L. S. Sochava, and V. S. Vikhnin, Ferroelectrics **183**, 255 (1996).
[8] T. Feng, Phys. Rev. B **25**, 627 (1982).
[9] M. Janousch, G. I. Meijer, U. Staub, B. Delley, S. F. Karg, and B. P. Andreasson, Adv. Mater. (Weinheim, Ger.) **19**, 2232 (2007).
[10] E. S. Kirkpatrick, K. A. Müller, and R. S. Rubins, Phys. Rev. **135**, A86 (1964).
[11] T. Hirose and M. Kawaminami, J. Phys. Soc. Jpn. **50**, 843 (1981).

Paper III

The work presented in this chapter was published in :
S . F. Alvarado, F. La Mattina, and J. G Bednorz, *Electroluminescence in $SrTiO_3$:Cr single-crystal nonvolatile memory cells*, Appl. Phys. A **89**, 85-89 (2007).

Electroluminescence in $SrTiO_3$:Cr single-crystal nonvolatile memory cells

Abstract

Metal-insulator-metal (MIM) structures involving transition-metal oxides and, more recently, also perovskite oxides with resistive switching effects have attracted substantial interest in research aimed at nonvolatile memories of nanometer dimensions. Although some models are presently under discussion, it is still not clear whether the fundamental switching mechanism is an interface or a bulk property, or a combination of both. Extended defects, such as dislocation lines and changes in the oxygen vacancy concentration, are considered responsible for the conducting state, and local reduction/oxidation processes have been proposed to be responsible for the resistive switching. In addition, the role of dopants has not been discussed in depth. Here we report on an electric-field-controlled electron trapping/detrapping process involved in the resistive switching in Cr-doped $SrTiO_3$. Electroluminescence (EL) measurements reveal that during resistive switching, light emission is observed only in the switching transition from high to low conductivity. The EL spectrum is typical for Cr^{3+} in an octahedral ligand field, indicating that the switching process involves trapping/detrapping of electrons at the Cr site.With increasing conductivity of $SrTiO_3$, we observe a change from the predominant $^2E \rightarrow ^4 A_{2g}$ (R-line) to the vibronically red-shifted $^4T_2 \rightarrow ^4 A_{2g}$ transition, which points to a modification of the Cr-occupied lattice sites.

Appl. Phys. A 89, 85–89 (2007)
DOI: 10.1007/s00339-007-4207-2

Applied Physics A
Materials Science & Processing

S.F. ALVARADO[1,✉]
F. LA MATTINA[1,2]
J.G. BEDNORZ[1]

Electroluminescence in $SrTiO_3$:Cr single-crystal nonvolatile memory cells

[1] IBM Research, Zürich Research Laboratory, Säumerstr. 4, 8803 Rüschlikon, Switzerland
[2] Physics Institute, University of Zürich, Winterthurerstr. 190, 8057 Zürich, Switzerland

Invited rapid communication

Received: 28 June 2007/Accepted: 29 June 2007
Published online: 17 July 2007 •

ABSTRACT Metal–insulator–metal (M–I–M) structures involving transition-metal oxides and, more recently, also perovskite oxides with resistive switching effects have attracted substantial interest in research aimed at nonvolatile memories of nanometer dimensions. Although some models are presently under discussion, it is still not clear whether the fundamental switching mechanism is an interface or a bulk property, or a combination of both. Extended defects, such as dislocation lines and changes in the oxygen vacancy concentration, are considered responsible for the conducting state, and local reduction/oxidation processes have been proposed to be responsible for the resistive switching. In addition, the role of dopants has not been discussed in depth. Here we report on an electric-field-controlled electron trapping/detrapping process involved in the resistive switching in Cr-doped $SrTiO_3$. Electroluminescence (EL) measurements reveal that during resistive switching, light emission is observed only in the switching transition from high to low conductivity. The EL spectrum is typical for Cr^{3+} in an octahedral ligand field, indicating that the switching process involves trapping/detrapping of electrons at the Cr site. With increasing conductivity of $SrTiO_3$, we observe a change from the predominant $^2E \rightarrow {}^4A_{2g}$ (R-line) to the vibronically red-shifted $^4T_2 \rightarrow {}^4A_{2g}$ transition, which points to a modification of the Cr-occupied lattice sites.

PACS 71.30.+h; 78.60.Fi; 73.40.Rw; 78.55.-m; 85.30.Tv

1 Introduction

There has been increased interest in investigating various types of nonvolatile random access memories. Different concepts are being pursued to develop storage devices with higher areal densities and lower power consumption than those of standard flash memory. One approach is to use ferroelectric polarization in a FET-like arrangement to modulate the resistance in an adjacent conducting channel [1, 2]. Simpler memory cells presently under intense investigation are based on the resistance change of a medium by means of current or voltage pulses, an effect observed in a large variety of materials. In the so-called phase-change materials, based on chalcogenide compounds [3], the mechanism for establishing the "low" and "high" resistance states is well understood, whereas for binary or ternary oxides such as Perovskites, a clear picture has not yet emerged. Current-induced bistable resistance effects or voltage-controlled negative resistance phenomena in compounds such as Nb_2O_5, TiO_2, Ta_2O_5 and NiO [4–7] and selected Perovskites exhibit strong similarities in current–voltage (I–V) characteristics from the macroscopic down to the nanometer scale [8–10], suggesting that a common scheme may be applicable.

Among the models proposed to explain the physical origin of the resistance changes in these materials, one finds modified interface properties [11–13], local inhomogeneities in the conduction path [14, 15] and a phenomenological approach involving a nonpercolating domain structure [16]. While most research is done on thin-film oxide layers, a few reports on memories are based on bulk single crystals [15, 17–20]. With the availability of doped $SrTiO_3$ single crystals, which exhibit the same memory behavior as doped $SrTiO_3$ and $SrZrO_3$ films, it became possible to study the influence both lattice defects controlled by dopants and interface effects have on the performance of a model memory system. In manganites, hole doping provides a sufficiently high bulk conductivity so that both thin films [8] and single crystals [19, 20] apparently do not require any electrical formation process prior to memory operation, or this it is not discussed.

In contrast, doped and/or oxygen-deficient $SrTiO_3$ requires a dc electric stress, a so-called forming process, to drive the insulator into a conducting state, which is the prerequisite for the realization of bistable resistive memory. Extended defects such as dislocations [21] and changes in the oxygen–vacancy concentration [18, 22] are considered responsible for the conducting state achieved by forming, while local reduction/oxidation processes have been proposed as an explanation for the resistance switching mechanism [15, 23]. A possible role of controlled defects in the form of dopants has not yet been discussed in depth.

✉ Fax: +41-1-724-8958, E-mail: alv@zurich.ibm.com

2 Experimental

Single crystals grown in air by the floating-zone method [18] were annealed at 1150 °C in Ar/H_2 5% to adjust a defined condition with respect to the Cr valence. ESR spectra taken at 80 K with a BRUKER EMX system at 9.4 GHz enable a quantitative comparison between oxidized and reduced crystals. In the oxidized sample, the absence of the Cr^{3+} signal implies that almost all Cr ions are in the tetravalent state. A direct detection of Cr^{4+} requires measurements at higher frequencies (> 34 GHz) [24, 25]. Upon reduction of Cr-doped $SrTiO_3$, a large fraction (estimated to be between 100% and 50%) of the Cr dopants change their valence to 3+ because of charge compensation due to the presence of oxygen vacancies. A reduced $SrTiO_3$ crystal with a concentration of 0.0001 mol. % of Cr was used as reference to estimate the concentration of spin centers. At this low concentration, one can assume that, upon reduction, all of the Cr atoms are converted to the 3+ valence state. Pt electrodes of 50–100 nm thickness with a typical separation of 500 μm are deposited on (100) faces of polished crystals via e-beam evaporation in either planar or capacitor geometry, producing a fully symmetric M–I–M structure. This enables optical access to the volume between the electrodes during the dc stressing and memory operation with the electric field along the main crystal axis. The luminescence experiments are performed using an optical multichannel analyzer covering a spectral range of 300–1000 nm and with a photon-counting Si avalanche photodiode for the wavelength-integrated signal in the 400–1060 nm range. All measurements are done under ambient conditions using reduced crystals. No I–M transition could be observed in the fully oxidized state or undoped reduced crystals.

In Cr-doped crystals, it was shown that the conducting state achieved by the forming is associated with a change of the Cr valence from 3+ to 4+, which suggests that Cr^{3+} can be a source of carriers for the conduction band (CB) [18]. The Cr^{3+} and Cr^{4+} impurity levels within the band gap of $SrTiO_3$ [26] will act as donor and acceptor, respectively [27–30]. In this report we present experimental evidence of an electric-field-driven electron trapping/detrapping process at the Cr site, which is involved in the resistive switching of Cr-doped $SrTiO_3$.

3 Results

3.1 *Photoexcited luminescence and electroluminescence during sample forming*

EL and photoexcited luminescence spectra, collected on unformed samples, allow us to assign the optical response to the $^2E \rightarrow {}^4A_{2g}$ transition, the typical *R*-line of Cr^{3+} in an octahedral site [31–33]. In the conducting state, however, a significantly broadened spectrum suggests that modified defect states are involved in the charge transfer, and the EL spectra indicate carrier recombination during switching from the low (LR) to the high-resistance (HR) memory state.

In pure $SrTiO_3$ the formation of oxygen vacancies during the reduction process leads to a filling of Ti 3*d* CB states and an insulator-to-metal (I–M) transition takes place when a sufficiently high electron doping is established. However, our ESR data (see Fig. 1) show that, upon reduction of Cr-doped $SrTiO_3$, a fraction of the Cr^{4+} (see methods) changes its valence to 3+, indicating that electron doping oc-

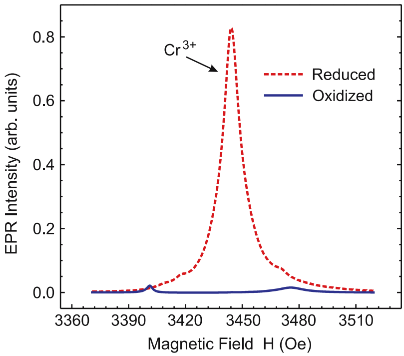

FIGURE 1 EPR Cr^{3+} *X* band signal (integrated intensity) in $SrTiO_3$ doped with 0.2% Cr. The *blue curve* is obtained in a sample oxidized 8 h at 1150 °C in an oxygen atmosphere. The *red-dotted curve* is obtained after reducing the sample by annealing for 8 h in H_2/Ar atmosphere at 1150 °C. This process produces oxygen vacancies in $SrTiO_3$, which, because of charge compensation, changes the valence of a fraction of the Cr dopant atoms from 4+ to 3+ valence

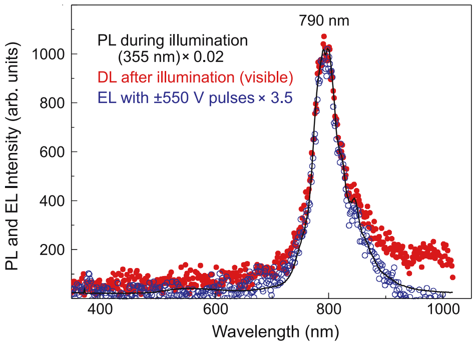

FIGURE 2 Luminescence of a $SrTiO_3$:Cr 0.2 mol % single-crystal: virgin sample at zero bias during laser (355 nm) exposure (PL) (*black line*); virgin sample in the dark during application of voltage pulses of ±550 V (EL) (*open blue circles*); spectra from a virgin samples after exposure to white light, taken with a delay of 2 s (DL) (*filled red circles*). This emission corresponds to the *R*-line, characteristic for charge-transfer processes involving Cr^{3+} in an octahedral crystal field [29, 31]. Hereby a CB electron when trapped by Cr^{4+} forms an excited Cr^{3+} state, which subsequently relaxes to the ground state via the $^2E \rightarrow {}^4A_{2g}$ transition [26, 27]

curs at the Cr-dopant sites instead [33]. The energy levels of the latter are located in the band gap of the $SrTiO_3$ host [26, 29] and, therefore, the crystals remain insulating. Because of the high initial resistance, the forming procedure has to start at a high dc voltage (up to 1 kV) in order to initiate a current flow in the nA range. As continuous carrier injection leads to an increasing current with time, the voltage is decreased in steps to keep the power at a low level to prevent irreversible damage. The final state in which stable resistive switching is established is typically reached in 5 to 10 h. This process can be accelerated by photo-excitation in the visible. It was assumed [9, 17] that the Cr^{3+} center acts as a source of carriers needed to induce the I–M transformation. Proof of an excitation of electrons involving the Cr site is provided by the spectra of the photoluminescence (PL) and EL signals, the latter excited with bias voltage pulses at relatively low currents. Both show the occurrence of a dominant line at approx. 790 nm, with a full width at half maximum of 45 nm, Fig. 2. This emission corresponds to the *R*-line, characteristic of charge-transfer processes involving Cr^{3+} in an octahedral crystal field [31, 33]. It results from the excitation of an electron from Cr^{3+} to the CB, leaving the Cr in the tetravalent state. A CB electron, when trapped by Cr^{4+}, will form an excited Cr^{3+} state, which subsequently relaxes via the ${}^2E \to {}^4A_{2g}$ transition to the ground state [28, 29]. Furthermore, excitation at various wavelengths (355, 633 and 780 nm) confirms that electron transfer to the CB takes place at subbandgap energies above 1.86 eV (670 nm) [28], a condition also met for irradiation in the visible. This is consistent with our ESR measurements (data not shown), which under continuous irradiation with an electric field applied show a decrease of the Cr^{3+} signal. The *R*-line emission observed both in the delayed luminescence (DL) at zero bias at the early stages of stressing and in the EL can be taken as proof of the contribution of the Cr^{3+} impurity gap states in promoting the I–M transition in $SrTiO_3$.

Near the completion of the forming process, the resistance typically decreases to the $k\Omega$ range, where the I–V loops begin to develop the hysteretic characteristics (inset of Fig. 3) required for resistive memory switching. At this stage, the system behaves metastably and has not yet developed a sufficiently large and stable asymmetry, which at low voltages should exhibit an almost ohmic behavior in the LR and a small dI/dV ratio in the HR state.

The broad EL spectrum (Fig. 3) suggests a superposition of multiple emission lines, but the *R*-line still is a dominant feature (Fig. 2), already observed before the forming process. This implies that in the conducting state the charge-transfer processes via the Cr band-gap states play a significant role in the electronic transport.

3.2 *Electroluminescence behavior of a formed memory cell*

In this particular example, we observe that by running voltage sweeps at higher currents (Fig. 4a–c), the hysteresis eventually undergoes a transition to a final stable asymmetric state. Thus, from an intermediate state (Fig. 4a), in which the memory cell remained in LR, a pronounced hysteresis can be established through sweeps at a higher compliance (80 mA), see Fig. 4b. Once a stable asymmetry is imprinted, the hystere-

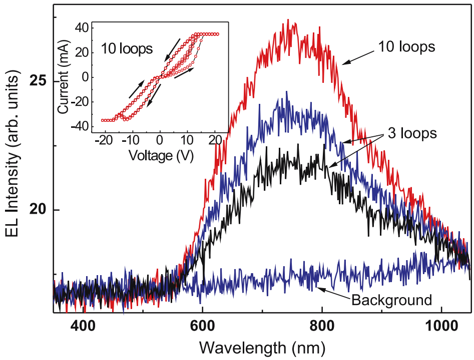

FIGURE 3 EL spectrum recorded during multiple hysteresis loops: 10 loops (*red*); three loops (*blue, black*). The spectra consist of a superposition of emission lines; one of them centered at approx. 790 nm exhibits the signature of the characteristic Cr *R*-line (Fig. 2)

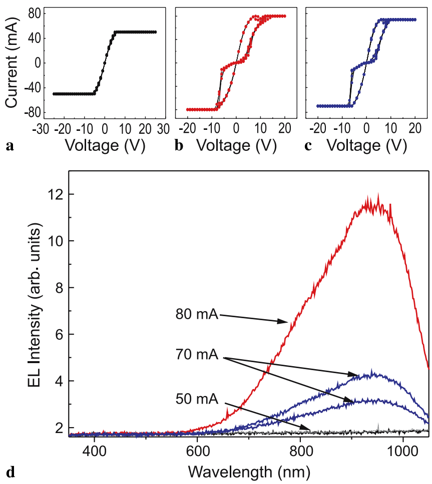

FIGURE 4 EL spectra of memory cell approaching a stable state (3 I–V loops each). (**a**) I–V loops at intermediate switching state, no switching. During these loops, no EL could be detected (background signal). (**b**) By increasing the compliance to 80 mA, a stable asymmetry is imprinted in the hysteresis. (**c**) Stable operation at compliance reduced to 70 mA. (**d**) EL spectrum obtained during stable switching loops

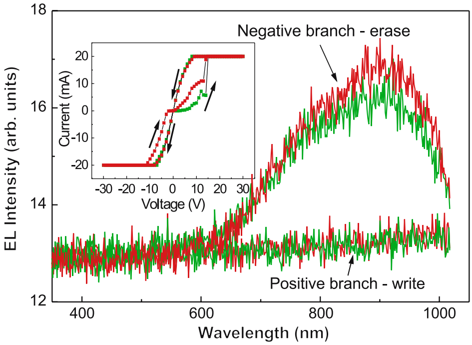

FIGURE 5 Two I–V loops with transition from a low to a high-resistance at negative polarity, and EL spectrum recorded separately for each write (positive branch) and erase (negative branch) half loop. The occurrence of the luminescence only at the erasing branch clearly indicates that this luminescence is correlated with a recombination process that decreases the number of conducting electrons

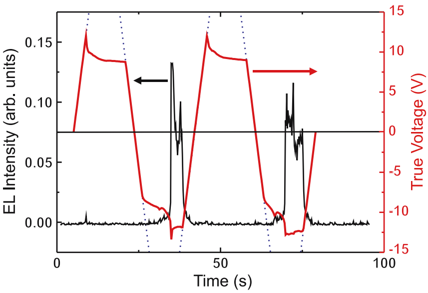

FIGURE 6 Simultaneous time-resolved luminescence (*black*) and I–V loops on a single crystal of $SrTiO_3$:Cr 0.2 mol. %. The abrupt changes of the true applied voltage curve observed in the negative branch of the hysteresis curve indicate that onset of EL coincides with an abrupt decrease in the conductance

sis is maintained by switching at lower currents (Fig. 4c).

The EL spectrum recorded during repeated voltage sweeps shows a drastic increase of intensity in the higher wavelength region, see Fig. 4, compared with Fig. 3. This is typical for a stable resistance switching, whereas no EL occurs in the intermediate state. We note that no simple relation of the EL intensity to the maximum current flowing exists. A clear EL signal with the same spectral distribution (Fig. 5) is also obtained for a memory cell operating at 20 mA. Current flow in confined regions or, in the extreme case, in filaments whose cross section can vary in different samples precludes measuring the true local power or current density. With the voltage swept in positive and negative half-loops, EL occurs in one polarity only, namely, in the negative branch of the hysteresis, where the LR to HR switching takes place. As the transition occurs while the current is in compliance, the actual true voltage applied is the relevant parameter for the detection of the switching and the correlation with the EL event. The wavelength-integrated EL signal and the true voltage measurement during a series of I–V loops are shown in Fig. 6. The abrupt changes in the V vs. t curve in the negative branch of the hysteresis indicate resistance changes that coincide with the onset of a strong EL. Apparently a threshold value either in the power density or in the applied field needs to be reached to initiate the process and maintain the EL until the voltage drops from its plateau value.

4 Discussion

A plausible explanation of the above results is that the EL arises from a dynamic process involving trapping of carriers at the Cr^{4+} centers with subsequent radiative transitions to the ground state. This is clearly the case for the $^2E \rightarrow {}^4A_{2g}$ transition. Regarding emission in the 900 to 1000-nm range, one could invoke local Joule heating due to the high currents. Luminescence spectra obtained on crystals heated up to 980 °C indicate, however, that the spectral features of the EL cannot be accounted for by black-body radiation, which leaves an electronic transition as the origin of this emission band. Such a band in this energy range has actually been observed by optical excitation in numerous compounds with Cr dopants in octahedral lattice sites [35–37] and is assigned to the $^4T_2 \rightarrow {}^4A_{2g}$ transition. This indicates that, upon forming, a change in orbital occupancy takes place from t_{2g}^3 to $t_{2g}^2 e_g^1$ [32, 38, 39]. The latter transition appears at an energy lower than the R-line because of a strong electron lattice coupling [35] with a red shift of approx. 300 nm with respect to the $^4A_{2g} \rightarrow {}^4T_2$ absorption band at 670 nm, which is comparable to that found in other oxides [35–37, 40]. Thus in our forming process, on going from the insulating to the conducting state, the emission changes from the $^2E\left(t_{2g}^3\right) \rightarrow {}^4A_{2g}\left(t_{2g}^3\right)$ (R-line) to a predominant $^4T_2\left(t_{2g}^2 e_g^1\right) \rightarrow {}^4A_{2g}\left(t_{2g}^3\right)$ transition. A plausible explanation for this shift is a nonreversible field-induced distortion of the Cr-occupied octahedral lattice site, leading to a change of the relative transition probabilities. Such a change of balance from the $^2E \rightarrow {}^4A_{2g}$ to the $^4T_2 \rightarrow {}^4A_{2g}$ emission has been observed under pressure-controlled distortion of the Cr-occupied octahedral site [40]. Evidence of an electric-field-driven modification in Cr-doped $SrTiO_3$ has been found in XAS mapping experiments, which reveal an oxygen vacancy migration into confined crystal regions [41]. This is consistent with our observed changes in EL. Therefore with progressive forming, the predominant EL shifts from the R-line, involving t_{2g} orbitals whose lobes point between the O-ligands, to EL from the $^4T_2 \rightarrow {}^4A_{2g}$ transition. The latter involves e_g orbitals represented by the $x^2 - y^2$ and z^2 $3d$ wave functions [32], which have lobes pointing towards the O-ligands. Hence both octahedral distortions [27, 35, 42, 43] and oxygen vacancies will strongly affect the transition probabilities.

5 Summary

Our luminescence measurements performed on $SrTiO_3$:Cr crystals at different stages of conductivity reveal that the light emission is associated with $3d$ intrashell transitions of Cr^{3+} in an octahedral lattice site. Electrically stimulated emission can be taken as proof of dynamic processes involving trapping and subsequent radiative decay of electrons at the Cr dopant sites. With increasing conductivity, achieved during forming, the emission maximum shifts from predominant $^2E\left(t_{2g}^3\right) \rightarrow {}^4A_{2g}\left(t_{2g}^3\right)$ (R-line) to predominant emission from the vibronically shifted $^4T_2\left(t_{2g}^2 e_g^1\right) \rightarrow {}^4A_{2g}\left(t_{2g}^3\right)$ transition. The latter is associated with a change in orbital occupancy, and its energy shift can be related to a geometrical change of the oxygen octahedron, either through distortion and/or a modified oxygen–vacancy distribution. The EL in the final state, which occurs only when the memory cell is switched from the LR to the HR state, can provide an important stimulus for the refinement of theoretical models by taking controlled and defined trapping centers into account.

ACKNOWLEDGEMENTS We thank K.A. Müller, H. Keller, A. Shengelaya, G.I. Meijer, S.F. Karg and R. Macfarlane for fruitful discussions. FLM gratefully acknowledges the support by the Swiss National Science Foundation. We also thank M. Tschudy, D. Widmer, H.P. Ott and K. Wasser for competent technical assistance.

REFERENCES

1 Y. Watanabe, Appl. Phys. Lett. **66**, 1770 (1995)
2 C.H. Ahn, J.-M. Triscone, N. Archibald, M. Decroux, R.H. Hammond, T.H. Geballe, Ø. Fischer, M.R. Beasley, Science **269**, 373 (1995)
3 H.F. Hamann, M. O'Boyle, Y.C. Martin, M. Rooks, H.K. Wickramashinghe, Nature Mater. **5**, 383 (2006)
4 W.R. Hiatt, T.W. Hickmott, Appl. Phys. Lett. **6**, 106 (1965)
5 G. Argall, Solid State Electron. **11**, 535 (1968)
6 K.L. Chopra, J. Appl. Phys. **36**, 184 (1965)
7 J.C. Bruyere, B.K. Chakraverty, Appl. Phys. Lett. **16**, 40 (1970)
8 S.Q. Liu, N.J. Wu, A. Ignatiev, Appl. Phys. Lett. **76**, 2749 (2000)
9 A. Beck, J.G. Bednorz, C. Gerber, C. Rossel, D. Widmer, Appl. Phys. Lett. **77**, 139 (2000)
10 V. Szot, R. Dittmann, W. Speier, R. Waser, Phys. Stat. Solidi **1**, R86 (2007)
11 A. Baikalov, Y.Q. Wang, B. Shen, B. Lorenz, S. Tsui, Y.Y. Sun, Y.Y. Xue, C.W. Chu, Appl. Phys. Lett. **83**, 957 (2003)
12 T. Fujii, M. Kawazaki, A. Sawa, H. Akoh, Y. Kawazoe, Y. Tokura, Appl. Phys. Lett. **86**, 012 107 (2005)
13 A. Sawa, T. Fujii, M. Kawasaki, Y. Tokura, Appl. Phys. Lett. **85**, 4073 (2004)
14 C. Rossel, G.I. Meijer, D. Bremaud, J. Appl. Phys. **90**, 2892 (2001)
15 K. Szot, W. Speier, G. Bihlmeyer, R. Waser, Nature Mater. **5**, 312 (2006)
16 M.J. Rozenberg, I.H. Inoue, M.J. Sanchez, Phys. Rev. Lett. **92**, 178 302 (2004)
17 Y. Watanabe, J.G. Bednorz, A. Bietsch, C. Gerber, D. Widmer, A. Beck, S.J. Wind, Appl. Phys. Lett. **78**, 3738 (2001)
18 G.I. Meijer, U. Staub, M. Janousch, S.L. Johnson, B. Delley, T. Neisius, Phys. Rev. B **72**, 155 102 (2005)
19 A. Asamitsu, Y. Tomioka, H. Kuwahara, Y. Tokura, Nature **388**, 50 (1997)
20 Y. Tokunaga, Y. Kaneko, J.P. He, T. Arima, A. Sawa, T. Fujii, M. Kawasaki, Y. Tokura, Appl. Phys. Lett. **88**, 223 507 (2006)
21 K. Szot, W. Speier, R. Carius, U. Zastrow, W. Beyer, Phys. Rev. Lett. **88**, 75 508 (2002)
22 S. Karg, G.I. Meijer, D. Widmer, J.G. Bednorz, Appl. Phys. Lett. **89**, 072 106 (2006)
23 D. Choi, D. Lee, H. Sim, M. Chang, H. Hwang, Appl. Phys. Lett. **88**, 082 904 (2006)
24 R.H. Hoskins, B.H. Soffer, Phys. Rev. **133**, A490 (1964)
25 D.E. Budil, D.G. Park, J.M. Burlitch, R.F. Geray, R. Dieckmann, J.H. Freed, J. Chem. Phys. **101**, 3538 (1994)
26 M.O. Selme, P. Pecheur, J. Phys. C **21**, 1779 (1988)
27 K.A. Müller, Proc. 1st Int. Conf. Paramagnetic Resonance, Vol. 1 (Academic Press, New York, 1963), pp. 17–43
28 S.A. Basun U. Bianchi, V.E. Bursian, A.A. Kaplyanskii, W. Kleemann, P.A. Markovin, L.S. Sochava, V.S. Vikhnin, Ferroelectrics **183**, 255 (1996)
29 S.A. Basun, U. Bianchi, V.E. Bursian, A.A. Kaplyanskii, W. Kleemann, L.S. Sochava, V.S. Vikhnin, J. Luminesc. **66–67**, 526 (1996)
30 A.J. Silversmith, W. Lenth, K.W. Blazey, R.M. Macfarlane, J. Luminesc. **59**, 269 (1994)
31 T. Feng, Phys. Rev. B **25**, 627 (1982)
32 L.E. Orgel, J. Chem. Phys. **23**, 1004 (1955)
33 A.M. Glass, J. Chem. Phys. **50**, 1501 (1969)
34 H.D. Meierling, Phys. Stat. Solidi B **43**, 191 (1971)
35 M. Grinberg, P.I. Macfarlane, B. Hendersson, K. Holliday, Phys. Rev. B **52**, 3917 (1995)
36 G.A. Torchia, O. Martinez Matos, P. Vaveliuk, J.O. Tocho, J. Phys.: Condens. Matter **13**, 6577 (2001)
37 G.A. Torchia, O. Martinez Matos, P. Vaveliuk, J.O. Tocho, Solid State Commun. **127**, 535 (2003)
38 Y. Tanabe, S. Sugano, J. Phys. Soc. Japan. **9**, 753 (1954)
39 Y. Tanabe, S. Sugano, J. Phys. Soc. Japan. **11**, 864 (1956)
40 M. Grinberg, J. Barzowska, Y.R. Shen, K.L. Bray, B.V. Padlyak, P.P. Buchynskii, Phys. Rev. B **65**, 064 203 (2002)
41 M. Janousch, G.I. Meijer, U. Staub, B. Delley, S.F. Karg, B.P. Andreasson, Adv. Mater. (2007), in press
42 M. Grinberg, W. Jaskolski, P.I. Macfarlane, B. Hendersson, K. Holliday, J. Luminesc. **72–74**, 193 (1997)
43 K.A. Müller, K.W. Blazey, T.W. Kool, Solid State Commun. **85**, 381 (1993)

Acknowledgments

I would like to thank all the people who have made this work possible, and helped me during the last four years. First, I want to thank Prof. Hugo Keller who "catched" me from the warm Sicily. He gave me the opportunity to work very freely and he supported me throughout the whole project. Each discussion with him, inspired me with new ingredients to build up my scientific personality.

Many experiments were made possible by the close collaboration with Dr. Georg Bednorz. He "fished" me from the University of Zürich and brought me to IBM Zürich Research Laboratory. His continuous and never-endig patience in discussing scientific problems has impressed me very much. I am very grateful to him for giving me the opportunity to work in his group and for their kind hospitality during my stay at IBM.

I really have to thank to Prof. Karl Alexander Müller. I discussed with him many times theoretical and experimental aspects of my investigation. He was able to open my mind giving me always a broad point of view.

I greatly enjoyed working with Prof. Alexander Shengelaya. He was a friend, and a perfect teacher. I addressed me always in the right direction. I will never forget his teaching methods. He followed me constantly, but as soon he realized that I was able to be independent he left to me the necessary freedom.

The continuous interest of Dr. Joseph Roos was also very helpful to my work. The discussions with him, always end up in the solution of a problem.

Dr. Alexander Maisuradze was a perfect colleague and a good friend. I had a lot of fruitful discussion in front of the EPR apparatus and sometimes in front of a bottle of Georgian Vodka.

Simon Strässle, Stephen Weyeneth, Dr. Stefan Kohout, and Dr. Björn Graneli gave me a comfortable environment and interesting insights into other fields, techniques and cultures. Martin Klöckner gave me assistance with technical details and good humor. Kurt Bösiger and the machine-shop team were always able to solve any of my strange requests.

Dr. Rustem Khasanov and Dr. Dimitry Eshchenko introduced me into the world of the μSR at PSI.

I want to thank all the people that I met during my work at IBM. Dr. Santos Alvarado helped me to arrange a set-up for the time-resolved spectroscopy presented in this work. Daniel Widmer, Dr. Rolf Allenspach, Dr. Antoine Vanhaverberke, Dr. Carlo Zinoni, Dr. Leo Gross, Reto Schlittler, and Dr. Gerhard Meyer for the sympathetic atmosphere and working environment at IBM.

Finally I want to thank all the other people which have supported me not only during my studies. Raffele Dell'Amore (o professò), Dr. Daniele Di Castro , Dr. Martina Corso, and Dr. Anna Tamai were my little italian community at the Physik-Institut. Dr. Claudio Cirelli, Francesca Albertini, e Dr. Andrea Carminati per essere stati la mia famiglia di Zurigo. Dr. Erika Di Giuseppe la mia sorellina, aquisita in Zelgstrasse 2. Dr. Marcello Bertoli mi ha allietato con le sue "storie".

La piccola Gaia, Vittoria ed il piccolo Nicolò mi hanno regalato l'emozione di sentirmi zio. Nathalie la mia maestrina. Dr. Riccardo Pellarin, Dr. Luca Reggiani, e Dr. Fabio Krog i miei compagni di giochi. Che dire di Dr. Marco Miranda? *E anche se ve lo dicessi, che ve lo dico affà?!*. I thank my parents that pushed me to take a risk sometimes. Più di tutti devo inoltre ringraziare Carlotta, che mi è stata accanto in questi ultimi due anni. Ogni minuto trascorso con lei è stato come un goccia di miele che scorre sulle labbra.

Curriculum Vitae

Name	Fabio La Mattina
Birth	26.07.1976 in Gela (CL), Italy
Nationality	Italian

Education

1990-1995	I.T.I.S. "Alessandro Volta", Palermo (Italy)
July 1995	Maturità tecnica industriale
1996-2003	Undergraduate Studies in Physics, University of Palermo
July 2001-July 2003	Diploma work at the Physics Institut of the Univerisy of Palermo in the "Laboratory of Amorphous Materials Physics" Group of Prof. R. Boscaino. Thesis Title: "Optical and ESR properties of Ge(1), Ge(2) and E'(Ge) centers in sol-gel Ge-doped silica"; supervisor: Prof. R. Boscaino (Univesity of Palermo). The thesis has been mentioned for the "E. Gugino" award.
Jul 2003	Graduation with full marks (110/110 cum laude).
since March 2004	Employed as PhD student in the Superconductivity and Magnetism Group of Prof. Dr. H. Keller.
May 2008	PhD thesis: "Insulator-to-metal Transition and Resistive Memory Switching in Cr-doped $SrTiO_3$: Charge-transfer Processes Involving the Cr Ions"; supervisor: Prof. Dr. H. Keller, Prof. Dr. A. Shengelaya, Dr. Dr. h.c. mult. J. G. Bednorz, and Prof. Dr. Dr. h.c. mult. K. A. Müller.

Teaching and Working Experiences

since January 2005	50% Employed at IBM Zürich Research Lab in the research staff of Storage & Memory Technology in the project of "Resistance change memory".
since March 2004	Teaching Assistent, Univerity of Zürich; lab-courses for physics students.

Publications

1. **F. La Mattina**, J. G. Bednorz, S. Alvarado, A. Shengelaya, K. A. Müller, and H. Keller
   Controlled oxygen vacancies and space correlation with Cr^{3+} *in* $SrTiO_3$,
   Physical Review B **80**, 075122 (2009)

2. **F. La Mattina**, J. G. Bednorz, S. Alvarado, A. Shengelaya, and H. Keller
   Detection of charge transfer processes in Cr-doped $SrTiO_3$ *single crystal*,
   Appl. Phys. Lett. **93**, 022102 (2008)

3. S . F. Alvarado, **F. La Mattina**, and J. G Bednorz,
   Electroluminescence in SrTiO3:Cr single-crystal nonvolatile memory cells,
   Applied Physics A **89**, 85-89 (2007).

Further publications

1. R. Khasanov, A. Shengelaya, A. Maisuradze, **F. La Mattina**, A. Bussmann-Holder, H. Keller, and K. A. Müller,
   Experimental evidence for two gaps in the high-temperature $La_{1.83}Sr_{0.17}CuO_4$ *superconductor*,
   Physical Review Letters **98**, 057007-1-4 (2007).

2. A. Bussmann-Holder, R. Khasanov, A. Shengelaya, A. Maisuradze, **F. La Mattina**, H. Keller, and K. A. Müller,
   Mixed order parameter symmetries in cuprate superconductors,
   Europhysical Letters **77**, 27002-p1-p4 (2007).

3. R. Khasanov, I. L. Landau, C. Baines, **F. La Mattina**, A. Maisuradze, K. Togano, and H. Keller,
   Muon-spin-rotation measurements of the penetration depth in Li_2Pd_3B ,
   Physical Review B **73**, 214528-1-6 (2006).

4. S. Agnello, R. Boscaino, **F. La Mattina**, S. Grandi, A. Magistris,
   Hydrogen-related paramagnetic centers in Ge-doped Sol-Gel silica induced by γ*-ray irradiation*,
   Journal of Sol-Gel Science and Tecnology **37** 63-68 (2006).

5. R. Khasanov, D. G. Eshchenko, D. Di Castro, A. Shengelaya, **F. La Mattina**, A. Maisuradze, C. Baines, H. Luetkens, J. Karpinski, S. M. Kazakov, and H. Keller,
   Magnetic penetration depth in $RbOs_2O_6$ *studied by muon spin rotation*,
   Physical Review B **72**, 104504-1-7 (2005).

6. S. Agnello, R. Boscaino, **F. La Mattina**, S. Grandi, A. Magistris,
Optical Properties and Photosensitivity of Vacuum Synthesized Ge-doped Sol-Gel Amorphous SiO_2 ,
pag. 422-426 in Proceedings of 4th IEEE/LEOS Workshop on Fibres and Optical Passive Components, IEEE Catalog Number 05EX1021, ISBN 0-7803-8949-2, S. Riva-Sanseverino, M. Artiglia Ed. (2005).

7. R. Khasanov, D. G. Eshchenko, J. Karpinski, S. M. Kazakov, N. D. Zhigadlo, R. Brtsch, D. Gavillet, D. Di Castro, A. Shengelaya, **F. La Mattina**, A. Maisuradze, C. Baines, and H. Keller,
Pressure effects on the transition temperature and the magnetic field penetration depth in the pyrochlore superconductor $RbOs_2O_6$,
Physical Review Letters **93**, 157004-1-4 (2004).

8. S. Agnello, R. Boscaino, M. Cannas, F. M. Gelardi, **F. La Mattina**, S. Grandi, A. Magistris,
Ge related centers induced by gamma irradiation in sol-gel Ge-doped silica,
Journal of Non-Crystalline Solids **322**, 134 (2003).